Novel Ce3+ and Ce4+ Metal-Organic Frameworks: a multi-technique characterization

Università degli Studi di Torino
Doctoral School of Sciences and Innovative Technologies
PhD Programme in Chemical and Materials Sciences XXXI Cycle

Novel Ce^{3+} and Ce^{4+} Metal-Organic Frameworks: a multi-technique characterization

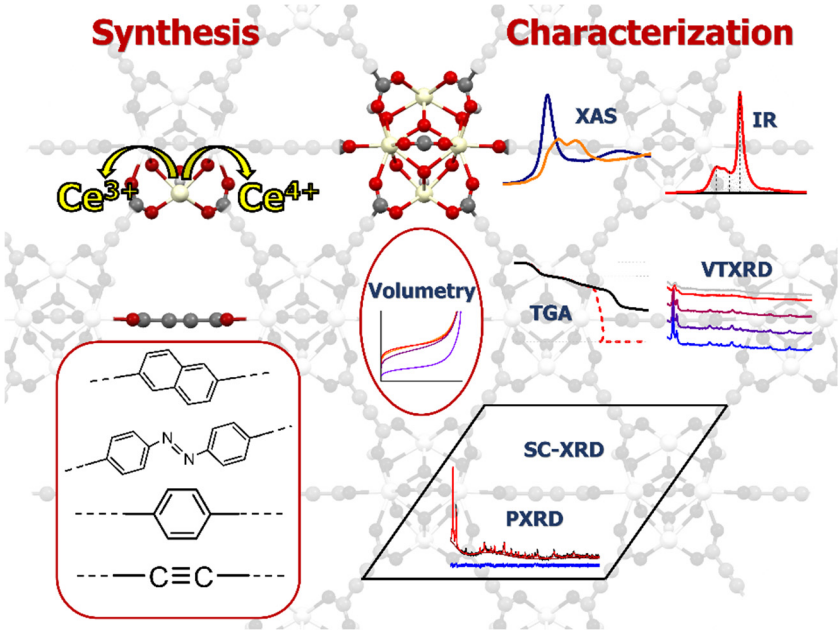

Cesare Atzori

Supervisor:
Dr. **Francesca Carla Bonino**

Università degli Studi di Torino

Doctoral School of Sciences and Innovative Technologies

PhD Programme in Chemical and Materials Sciences XXXI cycle

Novel Ce^{3+} and Ce^{4+} Metal-Organic Frameworks: a multi-technique characterization

Candidate: **Cesare Atzori**

Supervisor: Dr. **Francesca Carla Bonino**

Jury Members: Prof. **Bartolomeo Civalleri**
Università di Torino
Dipartimento di Chimica

Prof. **Claudio Gerbaldi**
Politecnico di Torino
Dipartimento Scienza Applicata e Tecnologia (DISAT)

Dr. **Kirill A. Lomachenko**
European Synchrotron Radiation Facility

Head of the Doctoral School: Prof. **Massimo Emilio Maffei**

PhD Programme Coordinator: Prof. **Mario Chiesa**

Torino, 2018

Index

Preface

The present thesis concerns the core activities of my three years of PhD studies: the synthesis of novel Metal-Organic Frameworks (MOFs) and their characterization using a multi-technique approach.

The activities of my laboratory (NIS center at the Università di Torino) are focused on the characterization of materials and their surfaces using a wide range of techniques, mainly spectroscopies. In order to develop the synthetic skills required for the present research I spent a period of 3 months abroad in the laboratory of Prof. Stock in Kiel (Germany), whose research interests are mainly devoted to synthesis of new MOFs. The skills acquired in that period were applied to the development of the synthetic procedure of each material reported in the present document.

The "trait d'union" of this thesis is the use of cerium cations in Metal-Organic Frameworks. This metal, albeit uncommon in the current MOF literature, is characterized by a high availability and a peculiar chemistry which permitted to obtain equally peculiar MOF compounds.

The following work is articulated into: 1) Introduction section, where MOFs will be described in general together with the main synthetic methods and characterization techniques used in the field and a fast survey on the main applications where MOFs play a role; 2) Synthetic procedures and Experimental methods; 3) Results presented in four different sections, each one devoted to a different material; 4) Conclusions.

1.Introduction

1.1 Metal-organic Frameworks

Metal-organic frameworks (MOFs) represent a class of hybrid porous solids formed by both organic and inorganic metal clusters connected together by coordination bonds.[1–6] They represent a versatile class of materials very often characterized by permanent porosity. They are made of discrete inorganic metal cations or small clusters that act as nodes in the framework and organic linker molecules that form together a specific crystalline structure when they establish a metal-ligand coordination bond. For this reason a lattice is generated by the ideal infinite repetition of this motif in the three dimensions. The very high structural diversity and chemical versatility of these materials can be attributed to the possibility to tune their properties by an opportune choice of both organic and inorganic building units. Thanks to this peculiarity, MOFs have opened access to a wide spectrum of functionalities not present in traditional porous materials. The exploration of structure-function relationships has attracted a tremendous amount of interest by the scientific community in the last two decades, mainly. These materials can be characterized by high specific surface areas, tunable pore size and specific chemical functionalities opening a wide landscape of potential applications in various fields like catalysis, gas storage and separation and energy-related usages, for example light-harvesting.

1.1.1 Definition and nomenclature

According to IUPAC,[7] the term "Metal-Organic Framework" stands for a coordination compound which structure satisfies the following criteria:

- Extends in two or three dimensions through repeating coordination bonded entities
- Contains organic linkers
- Contains potential voids

These compounds must follow the classical rules for naming chemical compounds (e.g. sodium benzoate) but in the literature from the very beginning the name assigned to the MOF refers to the laboratory where the material was discovered, followed by a number. For example MIL- for the Materials Institute Lavoisier, UiO- for the University of Oslo, while the short name MOF- is used by the material synthesized in the laboratory of Prof. Yaghi in Berkeley who is, in fact,[8] the inventor of the "Metal-Organic Framework" name.

1.1.2 History

Compounds falling in the definition of MOF proposed by IUPAC started to appear in the literature way back in 1959, where an early example of coordination network with potential voids based on copper and organic linkers is reported by Kinoshita et al.[9] Some other compounds with those criteria appeared in the literature at the end of the '80's,[10,11], and some other in the first years of the '90s principally due to Zaworotko,[12] Kitagawa,[13] and Yaghi.[14] After a couple of years MOF-2[15] (1998), MOF-5[16] (1999) and HKUST-1[17] (1999) will be published by Yaghi and co-workers and the last by Williams et al.. These are the first published MOFs based on carboxylate building units. MOF-5, which is chemically a zinc terephthalate, is characterized by an extremely high porosity, which can be measured in the order of 3000 m^2/g by nitrogen adsorption uptake experiments. This evidence was judged to be ground-breaking for the time of the discovery, being these specific surface areas totally unprecedented. This resulted in an enormous increase of effort by the scientific community in researching MOFs, which is still growing nowadays, as testified by the number of MOF structures[18] published in the CSD (Cambridge Structural Database) crystallographic database (Figure 1).

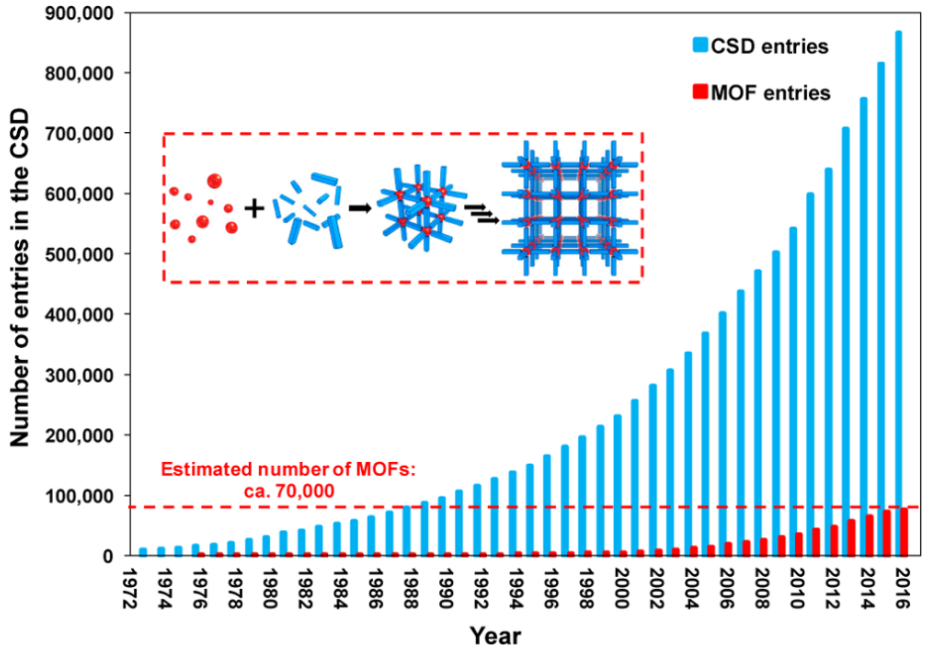

Figure 1 – Growth of the MOF entries published in the Cambridge Structural Database (CSD). Taken from ref. [18].

1.1.3 Reticular chemistry

Some authors, principally O'Keeffe, Yaghi and Eddaoudi[19] rationalized MOFs structure on the basis of a network analysis: they considered the combination of the inorganic and the organic building units of the structure as Secondary Building Units (SBUs) which can be used to build the MOF structures.

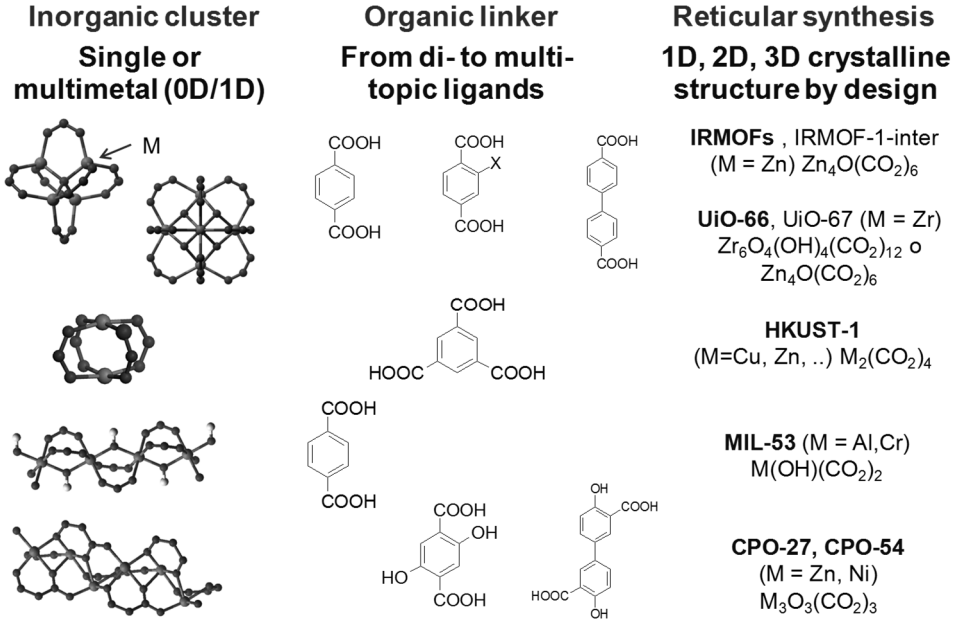

Figure 2 – Examples of inorganic and organic components of the most common MOFs. SBUs are highlighted in the left column. Taken from ref. [20]

The identification and the classification of the networks, done mainly with an *ab-initio* approach (i.e. without a knowledge on the chemistry of the materials, only relying on the connectivity of the SBUs), allowed the building of targeted networks by design. The Reticular Chemistry Structure Resource[21] (RCSR) is a collection of thousands of different theoretical nets which all different combinations among different geometries of the metals and the linkers is explored: it reports also the crystallographic space group of the resulting materials.

An example of the so-called reticular chemistry is the series of UiO-66, 67 and 68 materials[22] (Figure 3) where only varying the length of the organic linkers one obtain a series of materials with the same inorganic cluster and the same cubic topology.

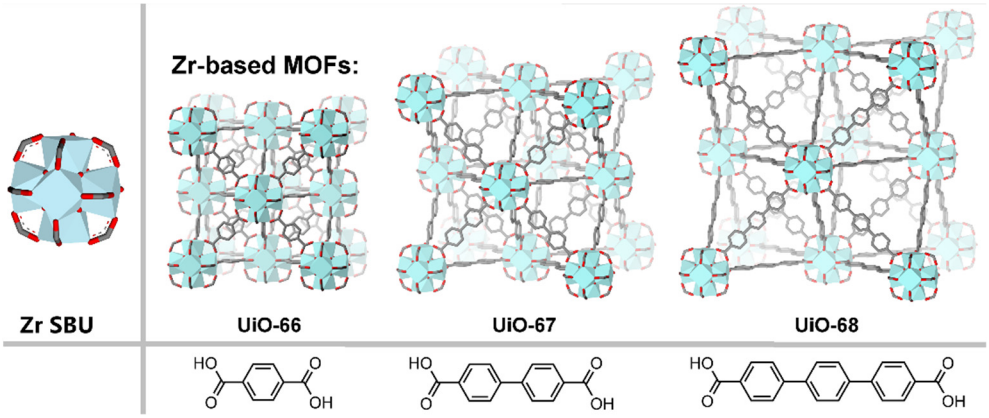

Figure 3 – Crystal structures of UiO-66, 67 and 68 materials as published by Cavka et al.[22] Coordination spheres of Zr atoms are represented by polyhedrons, carbon and oxygen atoms are printed in black and red, respectively. Hydrogen atoms are omitted for the sake fo clarity. Taken from ref. [23].

This approach permitted to modulate the final properties of the MOFs by a very high degree of control. For example the specific surface area for these materials is reported to be 1187 m^2/g for UiO-66 and 3000 and 4170 m^2/g for UiO-67 and UiO-68, respectively.

1.1.4 Ce-based MOFs

Cerium is the most abundant lanthanide element present in the earth crust[24,25] (see Figure 4) and it is inherently cheap for this reason. The ores that are mined for the extraction of the more rare and precious rare earth elements (like Nd, Eu, Tm and Lu) are also rich in Ce and this causes a large introduction of this element in the market, which is the cause for its low price (6 US$/kg for Ce metal and 2.6 US$/kg for CeO_2 in 2018[26]).

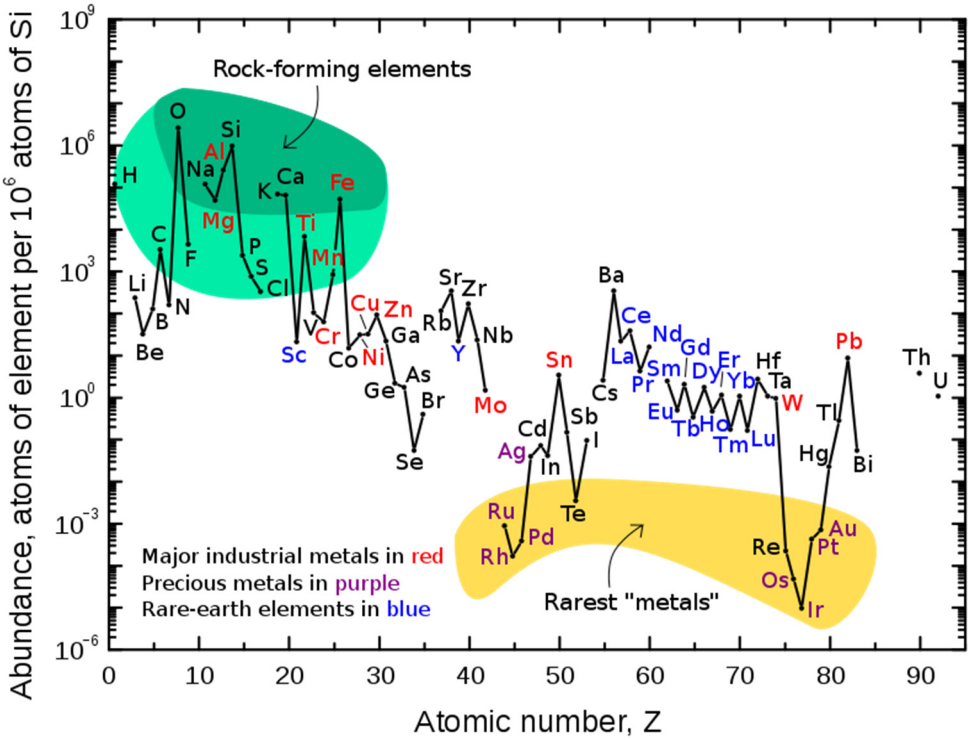

Figure 4 – Abundance (atomic fraction) of the chemical elements in the Earth's upper continental crust as a function of the atomic number. Adapted from ref. [24]

Its oxide CeO_2, commonly named ceria, is particularly relevant for redox chemistry being a catalyst for oxidation and reduction reactions[27]. The fact that Ce is stable in both oxidation states Ce^{3+} and Ce^{4+}, a unique peculiarity for a lanthanide element, is exploited in applications like combustion catalysis,[28] reforming processes and photocatalysis.[27]

Ce based MOFs have been more recently studied by the scientific community: general traits that can be drawn looking at the current literature published on Ce containing MOFs is the following:

- Both Ce^{3+} and Ce^{4+} oxidation states can be used in the synthesis of MOFs
- Synthetic conditions for Ce^{3+} containing MOFs tends to be harsher than Ce^{4+}
- Usually Ce^{4+} starting reagents may be reducing to Ce^{3+} during the synthesis, the opposite was never observed, at the best of the knowledge of the author.
- Ce^{3+} materials have more frequently peculiar structures, while Ce^{4+} tends to give rise to MOFs having the same structure of other 4+ cations (e.g. Zr^{4+} or Hf^{4+}). Their thermal stability is generally lower than their Zr^{4+} counterparts.

A list of reported Ce^{3+} containing MOFs is reported in Table 1 while the Ce^{4+} containing ones are reported in Table 2, respectively. Part of the reviewing of the literature has been already done by Lammert.[29]

Table 1 – MOFs containing Ce^{3+} cations published in literature.

Formula	Linker molecule	Reference
$[Ce_2(L)_2(DMF)_4]$	4,4',4''-{[(2,4,6-trimethylbenzene-1,3,5-triyl)tris-(methylene)] tris(oxy)}tribenzoic acid	30
$[Ce(HTCPB)]\cdot(EtOH)_{0.28}\cdot(H_2O)_{2.75}$	1,2,4,5-Tetrakis(4-carboxyphenyl)benzene	31
$[Ce(BTC)(DMF)_2]$	Trimesic acid	32
$[Ce_5(BDC)_{7.5}(DMF)_4]$	Terephthalic acid	33
$[Ce_2(ADC)_3(DMF)_4]\cdot DMF$	9,10-Anthracenedicarboxylic acid	34
$[Ce(ADC)_{1.5}(DMA)_3]$	9,10-Anthracenedicarboxylic acid	34
$[Ce(BTC)(H_2O)]\cdot DMF$	Trimesic acid	35,36
$[Ce_2(H_2O)(BPyDC)_3(DMF)_2]\cdot 2(DMF)$	2,2-Bipyridine-5,5'-dicarboxylic acid	37

$[Ce_4(H_2O)_5(BPyDC)_6(DMF)]\cdot x(DMF)$	2,2-Bipyridine-5,5'-dicarboxylic acid	37
$[Ce(TTTPC)(NO_2)_2Cl]\cdot H_2O_{10}$	1,1',1''-tris(2,4,6-trimethylbenzene-1,3,5- triyl)-tris(methylene)-tris(pyridine-4-carboxylic acid)}	38
$[Ce_2(EBTC)_{1.5}(CH_3OH)_4]\cdot 6H_2O$	1,1'-ethynebenzene-3,3′,5,5′-tetracarboxylic acid	39
$[Ce(HL)(DMA)_2]\cdot DMA\cdot 2H_2O$	5,5'-(2,3,5,6-tetramethyl-1,4-phenylene) bis(methylene) bis(azanediyl) diisophthalic acid	40
$[Ce_2(BPDA)_3(H_2O)_4]\cdot H_2O$	Benzophenone-2,4'-dicarboxylic acid	41
$[Ce_2(NDC)_3(DMF)_4]\cdot xH_2O$	1,4-Naphthalenedicarboxylic acid	42
$[Ce(NDC)_{1.5}(DMF)(H_2O)_{0.5}]\cdot 0.5DMF$	2,6-Naphthalenedicarboxylic acid	43
$[Ce(PDC)_{1.5}(DMF)]\cdot DMF$	3,5-Pyridinedicarboxylic acid	44,45
$[Ce_2(PDC)_3(H2O)_2]$	3,5-Pyridinedicarboxylic acid	46
[CeCl(BPDC)(DMF)]	4,4'-Biphenyldicarboxylic acid	47
$[Ce(BTPCA)(H_2O)]\cdot 2DMF\cdot 3H_2O$	1,1',1''-(benzene-1,3,5-triyl)tripiperidine-4-carboxylic acid	48
$[Ce_2(DHBDC)_3(DMF)_4]\cdot DMF$	Benzene-2,5-dihydroxy-1,4-dicarboxylic acid	49
$[Ce_6(BDC)_9(DMF)_6(H_2O)_3]\cdot 33DMF$	Terephthalic acid	50
$[Ce_2(ADB)_3(DMSO)_4]\cdot 6DMSO\cdot 8H_2O$	4,4'-Azodibenzoic acid	50

$[Ce_3(ADB)_3(HADB)_3]\cdot 33DMSO\cdot 29H_2O$	4,4'-Azodibenzoic acid	50
$[Ce_2(ADB)_3(H2O)_3]$	4,4'-Azodibenzoic acid	50
$[Ce_2(SDBA)_3(DMF)_4]$	4,4'-Sulfonyldibenzoic acid	51
$[(CH_3)_2NH_2]_3[Ce_3(SDBA)_6]\cdot 6DMF$	4,4'-Sulfonyldibenzoic acid	51
$[Ce(BTB)(H_2O)]$	1,3,5-Tris(4-carboxyphenyl)benzene	52
$[Ce_2(PDA)_3(H_2O)]\cdot 2H_2O$	1,4 Phenylendiacetic acid	53

Table 2 – MOFs containing Ce^{4+} cations published in literature.

Formula	Linker molecule	Reference
$[Ce_6O_4(OH)_4(Fum)_6]$	Fumaric acid	54
$[Ce_6O_4(OH)_4(BDC)_6]$	1,4-benzenedicarboxylic acid	54
$[Ce_6O_4(OH)_4(NDC)_6]$	2,6-naphthalenedicarboxylic acid	54
$[Ce_6O_4(OH)_4(BPDC)_6]$	4,4'-biphenyldicarboxylic acid	54
$[Ce_6(\mu_3\text{-}O)_4(\mu_3\text{-}OH)_4(OH)_4(H_2O)_4(TCPB)_2]$	1,2,4,5-tetrakis(4-carboxyphenyl)benzene	55
$[Ce_6O_4(OH)_4(FDC)_4(OH)_4(H2O)_4]$	2,5-furandicarboxylic acid	56
$[Ce_6(\mu3\text{-}O)_4(\mu3\text{-}OH)_4(BPyDC)_6]$	2,2′-bipyridine-5,5′-dicarboxylic acid	57
$Ce_6(\mu3\text{-}O)_4(\mu3\text{-}OH)_4(PZDC)_4(OH)_4(H2O)_4$	3,5-pyrazoledicarboxylic acid	57
$Ce_6(\mu3\text{-}O)_4(\mu3\text{-}OH)_4(TDC)_4(OH)_4(H2O)_4$	2,5-thiophenedicarboxylic acid	57
$Ce_6(\mu3\text{-}O)_4(\mu3\text{-}OH)_4(BTC)_2(OH)_6(H2O)_6$	benzene-1,3,5-tricarboxylic acid	57
$[Ce_6(OH)_4(O)_4(PDC)_{6-x}(Cl)_{2x}(H_2O)_{2x}]$	2,5-pyridinedicarboxylic acid	58

$[Ce_6O_4(OH)_4(CCA)_6]\cdot 6DMF\cdot 16H_2O$	4-carboxycinnamic acid	59
$[CeZr_5(\mu 3\text{-}O)_4(\mu 3\text{-}OH)_4(PZDC)_4(OH)_2(H_2O)_2]$	1-H-Pyrazole-3,5-dicarboxylic acid	60
$[Ce_6O_4(OH)_4(Muc)_6]$	Muconic acid	61
$[Ce_6O_4(OH)_4(CDC)_6]$	Trans-1,4-cyclohexanedicarboxylic acid	61
$[Ce_6(OH)_4O_4(BA)_4(TBAPy)_2]$	1,3,6,8-tetrakis(p-benzoate)pyrenehexacarboxylic acid	61

As an example of successful employing of Ce MOFs as redox catalysts Smolders et al.[62] reported in 2018 the catalytic activity of Ce-UiO-67 in the aerobic oxidation of benzylic alcohol to benzaldehyde mediated by TEMPO (2,2,6,6-tetramethyl-1-piperidinyloxy), as shown in Figure 5. The usage of X-Ray absorption spectroscopy permitted to unravel the role of the Ce cations in this catalytic cycle.

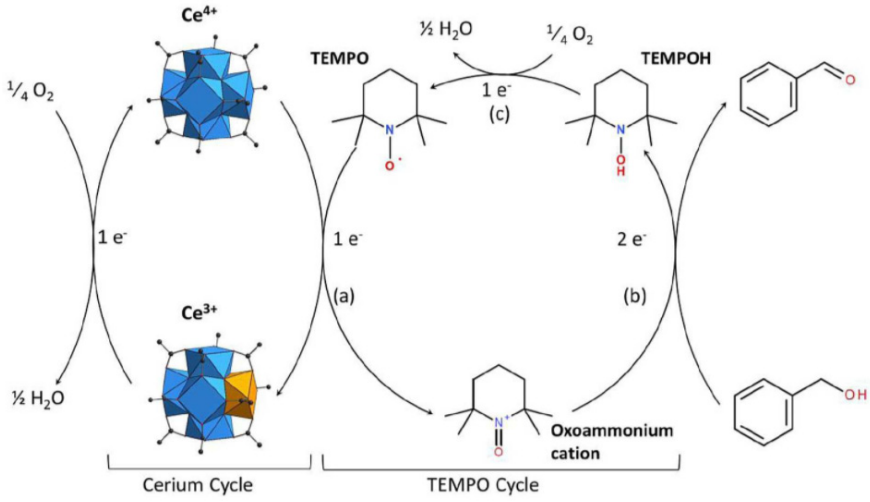

Figure 5 – Proposed reaction mechanism for the aerobic TEMPO-mediated oxidation of benzyl alcohol by Ce-UiO-67. Taken from ref.[62]

1.1.5 Mixed-metal MOFs

MOFs that present more than one metal (which can be named bimetallic or multi-metallic) were more recently introduced in the literature[63] as a way to impart those

materials the wanted properties (e.g. electronic, catalytic or sorption performances). They can be prepared by two main routes:

- One-step synthesis: this method involves the simultaneous reaction of the two metal precursors during the synthesis. This method often leads to fragile networks and unpredictable topologies. This method is then restricted to those metal whose reactivity is very similar. This is the method exploited by Lammert and co-workers[64] to synthesize Ce/Zr-UiO-66 bimetallic MOFs.
- Post-synthetic modifications: as an alternative way one can also firstly synthesize a mono-metallic MOF then exchange this metal with a different one with a process that is, in fact, a post-synthetic modification (see section 1.2.3). This method was used by Brozek et al.[65] to exchange Zn^{2+} cations in MOF-5 with Ti, V, Cr, Mn and Fe cations, also in different oxidation states. This approach permitted to obtain materials with peculiars catalytic properties[66]

Some of the relevant MOFs that have been synthesized also with multiple metals are enlisted in Table 3.

Table 3 – Review of the mixed-metal MOFs published in literature.

MOF	Involved metals	Reference
UiO-66	Ce, Zr, Ti	60,64,67,68
MOF-5	Ti, V, Cr, Mn, Fe	65
HKUST-1	Cu, Zn, Ru	69,70
MOF-74	Ni, Co	71
DUT-67	Ce, Zr	60
CAU-38	Ce, Zr	60
$(M_3O)_2(TCPP)_3$	Mn, Co,Ni, Fe	72
CPM-200	Fe, Mg, In, Ga, Co, Mn, Sc, Ni	73
PCN-224	Zr, Ti	74
MIL-88B	Fe, Ni	75

1.2 Synthesis

A great amount of effort was spent on the bottom-up synthesis of Metal-Organic Frameworks[76,77]: tuning the performance of these materials for selected applications has in fact to pass through the sieve of a successful and reliable synthesis.

Generally speaking, the optimization a MOF synthesis is the act of finding the conditions that lead to a defined inorganic unit without decomposing the organic linker. Moreover, the material has to nucleate and grow with an appropriate kinetics in order to have a crystalline product. This self-assembly phenomenon is depicted in Figure 6.

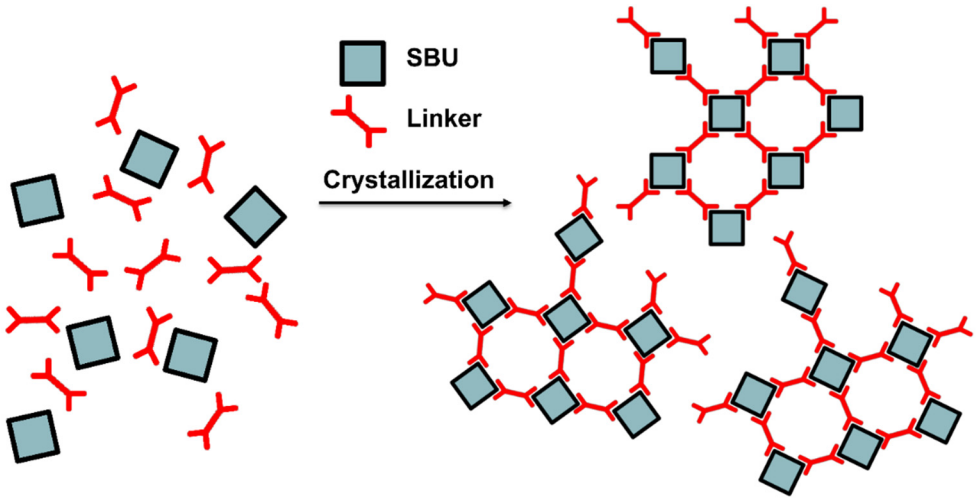

Figure 6 – Representation of the assembly phenomena of SBUs and linkers in MOF synthesis. Taken from ref. [78]

The most widely used method to synthesize MOFs is solvothermal synthesis, and in fact this is the way the materials discussed in the present thesis are made. This procedure is simply made by mixing a metal salt with the organic linker in a solvent (typically a high-boiling polar aprotic one, like DMF, DMA or DMSO) in a closed and robust vessel (like a Teflon-lined autoclave or a screw-top vial) and heat this using an oven for a fixed amount of time (that can be varying from minutes to days). The product then has to be retrieved (by filtering or centrifuging) and carefully washed from the solvent excess and the unreacted reagents.

To approach this problem several methods were employed and developed in the literature, some of these depicted in Figure 7 below. Not all of them are belonging to a solvothermal classification: for example solvent-free, mechanochemical or sonochemical methods were also exploited.

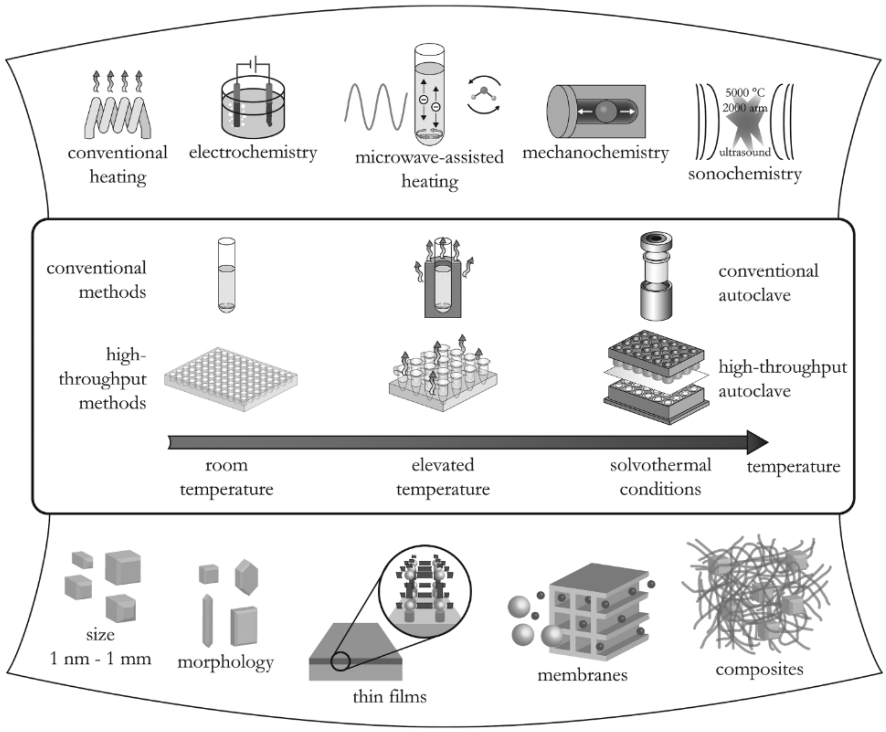

Figure 7 – Pictorial representation of some common synthetic methods for MOFs. Taken from ref. [76].

Apart from the correctness of the synthesized crystal phase and the yield of the reaction also the particle size and the morphology of the product must be optimized to suit the material for a specific application. Just to cite an example, a crystal of suitable dimensions (>200 μm, at laboratory instruments) is needed for the structural determination using the single-crystal X-Ray diffraction technique. Our synthetic procedure must be optimized in order to have such a crystal dimension if we want to do this experiment.

Controlled additions of reagents like modulators, Structure Directing Agents (SDAs) or mineralizers are widely used in MOF synthesis. Modulators are monodentate ligands having the same chemical functionality of the linker (which, for definition, must be multidentate) and is able to compete with the linker during the synthesis,

modifying thus the nucleation and growth kinetics and causing effects into the crystal size and the morphology of the product.[79] These have been used to modulate the dimensions of the crystals for example in UiO-66[80] and in the same material they demonstrated to have a great influence also on the defectivity.[81–84] SDAs, on the other hand, are used to "fill" the pore space and thus to promote the formation of the network. An example of usage of a SDA can be the usage of DABCO (1,4-diazabicyclo[2.2.2]octane) in the synthesis of DUT-8,[85,86] a Ni naphthalenate MOF. Mineralizing agents, finally, are added to help the dissolution of the reagents into the reaction mixture: commonly inorganic acids, bases or fluoride salts.

1.2.1 High-Throughput methods

Such a wide set of synthetic parameters (solvent, concentrations, temperature, residence time, addition of modulators, SDAs, mineralizers) must be optimized through exploratory synthesis and reasoned guess, as this field of synthetic chemistry is lacking the deep and mechanistic knowledge that is owned by the synthetic organic chemistry, for example. To overcome this time-consuming work a so called High-Throughput (HT) synthesis approach has been developed by Stock et al.[76,87] in order to accelerate the discovery of new compounds and the optimization of the parameters. The key point of such an approach is the parallelization of the syntheses achieved using multi-welled reactors and the systematic variation of the parameters like the solvent, metal source, reagents concentration, the additions of modulators. The obtained products, after recovery by filtration or centrifugation, are characterized by a fast PXRD measurement and the diffractograms are compared with databases containing the known compounds and the diffractogram of the reagents used in the synthesis. Analyzing those datasets, relevant trends and crystallization fields can be found. The whole HT process is flowcharted in Figure 8 below.

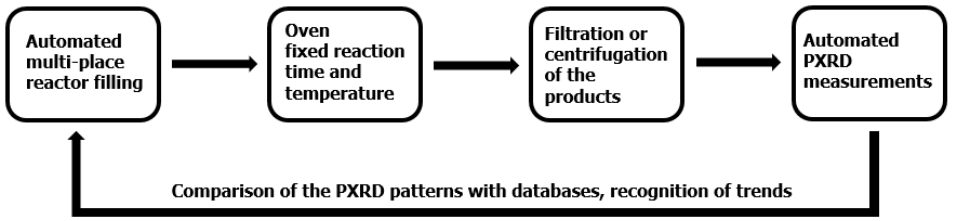

Figure 8 – A High-Throughput approach to MOF synthesis. Taken from ref. [20]

A nice example of HT investigation (Figure 9) of MOF compounds can be found in a work by Albat et al.[88] regarding the synthesis of compounds of Bi^{3+} and 4,8-disulfonyl-2,6-naphthalenedicarboxylic acid (H_4DSNDC). It is truly astonishing to

observe that with the systematic variation of the molar ratio, the pH, residence time and temperature (which was studied in more than 500 different reactions) six different compounds were isolated and the "recipe" for obtaining those pure compounds was obtained.

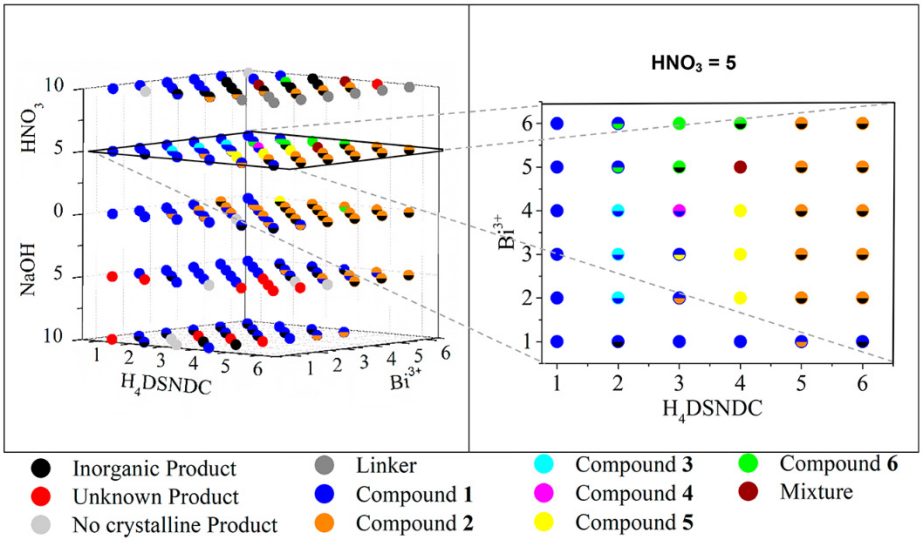

Figure 9 – Investigated parameter space for the synthesis of Bi^{3+}/H_4DSNDC MOF compounds at 180°C and 48 h of reaction time. Taken from ref.[88]

1.2.2 Linker functionalization

Linkers with the same topicity and geometry but different chemical functionalities can be exploited in MOFs in order to synthesize isostructural material with tunable and desired properties. Nice examples are the usage of 2-aminoterephthalic acid instead or in conjunction with terephthalic acid in Fe-MIL-101[89] and UiO-66[90,91] in order to insert -NH_2 dangling in the pores and thus control properties like the adsorption of carbon dioxide.

1.2.3 Post-synthetic functionalization

MOFs can be modified chemically after the synthesis in order to tune their properties[92,93]. This has been achieved by exchanging the monodentate moieties dangling from the defects of the material by Shearer et al.[82,94] in order to tune the adsorption properties of the materials for carbon dioxide. Another approach, followed by Øien et al.[95] and Braglia et al.[96], was to coordinate metallic species (respectively Pt and Cu) into bipyridine functionalized UiO-67s in order to synthesize potential heterogeneous catalysts.

1.3 Characterization

When the synthesis has been optimized at the point to produce the desired phase with sufficient purity and an acceptable yield, the characterization, as recently suggested by Howarth et al.[97], traditionally follows the following steps:

- Structure determination by X-ray diffraction techniques (i.e. Single-crystal or powder X-Ray diffraction, or SCXRD and PXRD)
- Assessment of the stability upon guest removal or thermal treatment by Thermogravimetry (TGA) or Variable-temperature powder X-Ray diffraction (VTXRD)
- Adsorption measurements by N_2 or Ar at low temperatures in order to measure the specific surface area and assess the porosity of the material.

1.3.1 Structure determination

Crystal structure determination is preferentially obtained through single-crystal X-Ray diffraction experiments, this technique being a very mature and reliable way to obtain crystallographic information.[98] In order to do so a crystal of sufficient dimensions (hundreds of μm, for laboratory diffractometers) has to be grown which is sometimes not compatible with the synthesis peculiarities (i.e. kinetics). The synthetic procedure can be adjusted in order to promote the formation of bigger crystals, also exploiting specific techniques like diffusion limited growth[76]. It has to be kept in mind that a synthetic procedure optimized for the formation of big crystals may not be representative of the material synthesized in the "classical" way. Synchrotron sources may be exploited to overcome this problem as single-crystal diffraction beamlines typically require crystal of smaller dimensions[99] than laboratory diffractometers but the access to these facilities may be not easy or immediate. For those materials all the efforts have failed in this sense, the less straightforward task of solving the structure from a powder diffractogram may be tempted. In this case, having complementary information like a similar structure that can be adapted to fit the unknown one may be extremely helpful. Also chemical measurements like elemental analysis (by ICP-MS), oxidation state determination (by XPS, XAS or UV spectroscopy experiments) may be used. Nevertheless *ab-initio* modeling can be also exploited to drive the structural determination toward a correct structure.

1.3.2 Solvent removal and thermal stability

A crucial step in the characterization of MOFs is the possibility to remove the solvent from the pores of the system keeping a permanent porosity, a procedure very often called activation. After any solvothermal synthesis the pore of the material remain filled with the solvent used in the reaction. These molecules can be removed in most of the cases by a thermal treatment during dynamic outgassing or inert flow at temperatures mild enough to keep intact the crystal structure of the materials. In order to optimize the activation conditions TGA and VTXRD data are combined to observe the temperature at which the solvent is removed and simultaneously looking at the diffractogram of the material at that temperature. In the cases when the temperature required is so high to cause a structural collapse, an exchange of the solvent with a more volatile one (for example exchange DMF with methanol) may be helpful to use a lower activation temperature. The same TGA and VTXRD techniques are used to measure the thermal stability of the material and to assess if there are phase transformations associated with the solvent removal or the thermal treatment itself. New crystal phases deriving from the thermal treatment may be solved using the same techniques described in the previous section.

1.3.3 Gas adsorption volumetry

Porous materials, as MOFs are, may have their porosity evaluated measuring adsorption isotherms of probe molecules like N_2, Ar or CO_2 that adsorbs into the internal surface of these frameworks. A nice review of what can be done with those kind of experiments has been published by Thommes et al.[100]. As this technique evidences directly the porosity, which may be overlooked by structural diffraction or thermal analysis techniques, the presence of specific surface area observed after activation is the most recognized proof for the successful removal of the solvent from the pores of the system.

1.3.4 X-Ray absorption spectroscopies in MOFs

X-Ray absorption spectroscopy (XAS)[101,102] techniques may be used in the characterization of MOF materials: information about the oxidation state and the local geometry of the metal cations can be extracted from the XANES spectra. EXAFS spectroscopy can be exploited in challenging case where single-crystal data is not available or there are motifs that are not following the symmetry of the whole structure (and thus, are “invisible” from diffraction) like defects or cluster geometries. The element-selectivity and the local structure information available from the EXAFS data analysis can be very helpful.

EXAFS can be relevant in confirming the structure obtained from diffraction experiments, as in the case of $Ce_2(NDC)_3$ (section 3.1) or in highlighting that the inorganic cornerstone has a lower symmetry with respect to that of the organic framework, as in the case of Ce/Zr UiO-66 (section 3.3). Such a synergic approach with X-Ray diffraction already shown its potentialities in disclosing the structures of solvated and desolvated UiO-66,[22,103] UiO-67,[104] Hf-UiO-66,[105] (see Figure 10) desolvated HKUST-1,[106] MOF-76-Ce,[36] and Ni-cubane MOFs.[107]

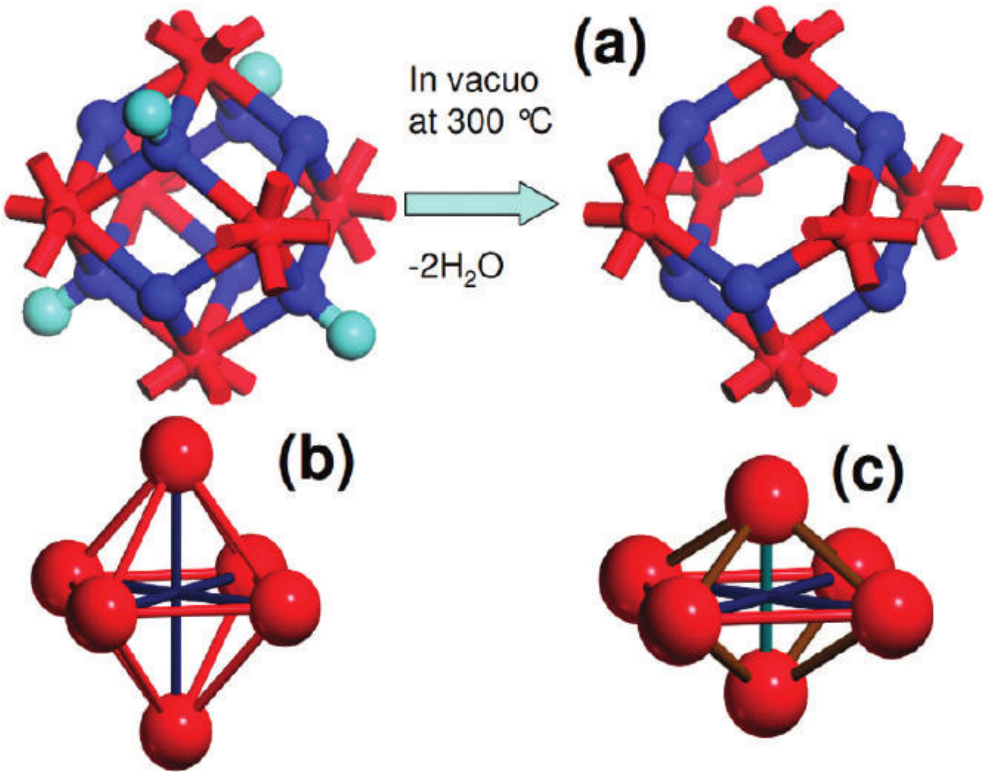

Figure 10 – Representation of the dehydroxylation undergone by the $Zr_6O_4(OH)_4$ cluster upon thermal treatment at 300°C in vacuo resulting in a disordered Zr_6O_6 cluster. Such transformation is "invisible" by diffraction and only EXAFS was able to see it. Red, blue and cyan color refer to Zr, O and H atoms respectively. Taken from ref. [103]

1.4 Applications

Among the variety of the applications in which the usage of MOFs was proposed in literature, the following three paragraphs are concerning three of them, being according the author the most prominent ones.

1.4.1 Gas storage and separation

The high porosity and specific surface areas of MOFs, sometimes combined with the presence of active species on the surfaces (i.e. open-metal sites), confers these materials the ability to store considerable amount of gases inside their pores. For this reason perhaps the most researched application of MOFs is their usage in gas storage[108–110] and separation[109,111]. Being really important for our economy the most studied gases in this respect are H_2 and CH_4 as energy vectors and CO_2 to CCUS (carbon capture, utilization and storage) applications. Patel and co-workers[112] recently published a series of guidelines (Table 4) which are to be followed if a technology based on a solid sorbent (like a MOF) has to compete with a classical carbon dioxide capture technology (i.e. aqueous solution of monoethanolamine).

Table 4 – Benchmark checkpoints for an effective CO_2 sorbent. Adapted from ref. [112]

Checkpoint	Desired
Capacity	>2 mmol CO_2 per g of sorbent
Recyclability	>1000 cycles
Selectivity	>100 (CO_2/other gases)
Stability	$>150\,^{\circ}C$, boiling water, H_2S, SO_x, NO_x, HCl, NaOH, mechanical strength with low attrition index (AI)
Cost	$<\$50\,kg^{-1}$ ($<\$10\,kg^{-1}$)
Kinetics	>1 mmol $(g \times min)^{-1}$

1.4.2 Catalysis

The usage of MOFs as heterogeneous catalysts has received extensively attention by the scientific community[113–115]. They are promising because the pore dimensions and the catalytic site can be designed at an unmatched degree if compared to previous catalysts. Their first results were essentially proof of concepts, as, in comparison to the most known inorganic catalysts (e.g. zeolites), MOFs are indeed fragile materials. Gascon and co-workers shown in a pictorial way (Figure 11) the possibilities to host a catalytic site inside MOFs, they can be inserted by both in-synthesis and post-synthesis modes and they rely on modifications of both inorganic and organic component of MOFs.

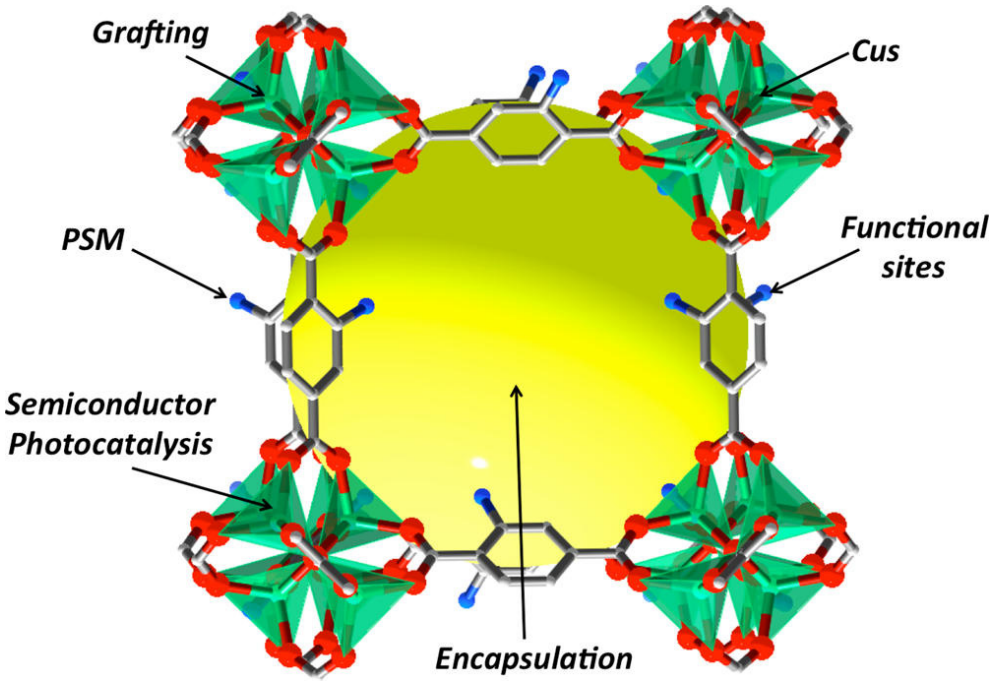

Figure 11 – Pictorial representation of the catalytic opportunities offered by MOFs. Taken from ref. [114].

Farrusseng et al.[116] classified the catalytic activities of MOFs in different mechanisms: (i) Lewis acidity, shown for example by open-metal sites. (ii) Brønsted acidity (iii) Basic functionality (iv) Enantioselectivity (enhanced by the chirality of the pore system) (v) C-C bond formation and polymerization (vi) Nanosized metal nanoparticles trapped inside the pores (vii) Organometallic complexes supported on MOFs.

1.4.3 Energy applications

Being MOFs extremely versatile, due to the unique possibility to tune their properties by a careful choice of the linker and the metal, a significant amount of research has been devoted in MOFs for energy related applications.[117,118] Recent examples of usage of MOFs in light harvesting,[119–121] energy storage,[122] conductive properties[123] have been recently published in the literature.

Exploiting the enormous structural tunability of MOFs, researchers explored a large numbers of structures in order to obtain photoactive materials, either using luminescent/chromophoric linkers or metal nodes [124,125] or inserting photoactive guest molecules in the MOF pores, using the ordered nanostructure to optimize the exciton migration.[126] Porphyrin-containing[124] MOFs, as well as Ruthenium based framework [125] have been explored for a possible use in hybrid photovoltaics such as Dye-Sensitized Solar Cells,[127] and their role as interfacial active agents at semiconductor interface or in the electrolyte[128,129] has been investigated.[126]

Until now, power conversion efficiencies in working devices are still very low, especially respect to the state of the art of these systems, but the first results are encouraging.

2.Experimental

2.1 Synthetic procedures for the MOFs

2.1.1 Synthesis of $Ce_2(NDC)_3(DMF)_2$

Chemicals were obtained from Alfa Aesar ($Ce(NO_3)_3 \cdot 6H_2O$, 99,5% purity), TCI (H_2NDC, 98 % purity) and Grüssing (DMF, 99 % purity) were used without further purification. Synthesis conditions were optimized by means of high-throughput methods (see section 1.2.1) To this purpose, reactors containing 24 Teflon liners with a maximum volume of 2 mL were filled with the reaction mixtures and then heated at the set temperature for a fixed time. After recovery of the solid product by filtration automated PXRD measurements permitted to identify the conditions where yield and crystallinity of the product were optimal. Once these optimal conditions were established, for the scaled-up synthesis of $Ce_2(NDC)_3(DMF)_2$ 778.3 mg (3.6 mmol) of 2,6-naphthalenedicarboxylic acid (H_2NDC), 13.2 mL (170 mmol) of DMF and 6 mL of a 130 g/L $Ce(NO_3)_3 \cdot 6H_2O$ solution in DMF (0.3 M and thus 1.8 mmol of Ce) were combined in a 25 mL Teflon lined autoclave. This vessel was closed and heated to 160°C in 3 h, kept at this temperature for 72 h and cooled down to RT in 12 h. The product was filtered off, washed with fresh DMF in the funnel for three times and dried on the filter paper under air flow. The yield of the reaction using the formula $Ce_2(NDC)_3(DMF)_2$ is 89% (based on the metal source). The product appears in the form of pale yellow needle-like crystals in the half-millimeter range of dimensions along the "long" axis of the crystal (see optical image in Figure 1).

2.1.2 Synthesis of $Ce_2(ADB)_3(DMA)_{3.4}$

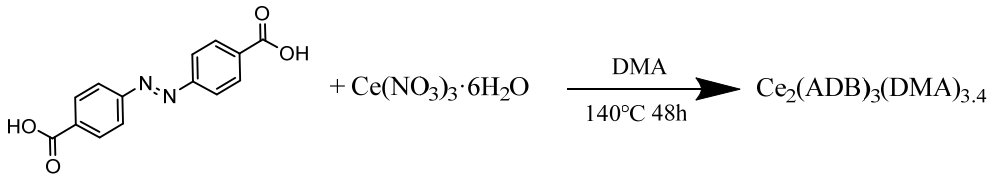

The synthesis of $Ce_2(ADB)_3(DMA)_{3.4}$ MOF was optimized by means of high-throughput methods (see section 1.2.1 and) under solvothermal conditions, details about the explored synthetic parameters are reported elsewhere.[130] Thus, 1.5 mmol (0.41 g) of azobenzene-4,4'-dicarboxylic acid (H_2ADB 95.0%,TCI) and 0.75 mmol (2.5 mL of a 0.3 M concentrated DMA solution) of $Ce(NO_3)_3 \cdot 6H_2O$ (99.0%, Sigma-Aldrich) were dissolved in 7.5 mL DMA (N,N-dimethylacetamide, 99.5%, Sigma-Aldrich). Then, the mixture was sealed in a 100 mL Teflon-lined stainless steel

autoclave and heated at 140 °C for 48 h. After cooling to RT (cool down rate: 0.4 °C/min), the product was centrifuged to remove the supernatant. Then it was washed with fresh DMA (2 mL) to remove unreacted linker and impurities. Finally, the product was dried at RT with a dry N_2 flow. The final yield was 0.59 g (57%, based on the metal source and the $Ce_2(ADB)_3(DMA)_{3.4}$ formula).

2.1.3 Synthesis of Ce/Zr-UiO-66

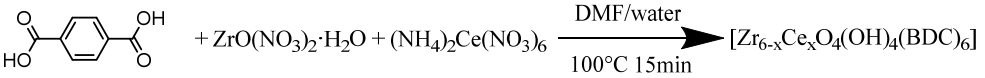

Cerium (IV) ammonium nitrate (98 %, $(NH_4)_2Ce(NO_3)_6$, Alfa Aesar), 1,4-benzenedicarboxyic acid (98 %, H_2BDC, Sigma Aldrich), zirconyl nitrate monohydrate ($ZrO(NO_3)_2{\cdot}H_2O$, ABCR), zirconium(IV) chloride (99 %, $ZrCl_4$, Sigma Aldrich), N,N-dimethylformamide (99 %, DMF, Grüssing) and formic acid (100 %, HCOOH, BASF) were used as obtained. The synthesis of the mixed-metal Ce/Zr-UiO-66 compounds was previously reported by Lammert et al.[54,64] and this procedure was also used in the current study. The Ce/Zr-UiO-66 compounds were synthesized using Pyrex glass reaction tubes (maximum volume 14 mL). The linker 1,4-benzenedicarboxylic acid (H_2BDC, 127.6 mg) was dissolved in N,N-dimethylformamide (DMF, 3.6 mL) and transferred into the glass reactor. Subsequently the formic acid (HCOOH, 100 %, 1.03 mL) and finally the aqueous solutions of $(NH_4)_2Ce(NO_3)_6$ (0.533 M) and $ZrO(NO_3)_2{\cdot}H_2O$ (0.533 M) were added in the desired stoichiometry (Table *5*). The total volume of the two metal salt solutions was always 1.2 mL.

Table 5 – Parameters for the synthesis of pure Ce-UiO-66 and mixed-metal Ce/Zr-UiO-66 samples. Ce, Zr, H_2BDC and HCOOH values are intended as mutual molar ratios.

Sample	Ce	Zr	H_2BDC	HCOOH	Ce [µL]	Zr [µL]
Ce5	0.3	5.7	7.2	256	60	1140
Ce10	0.6	5.4	7.2	256	120	1080
Ce15	0.9	5.1	7.2	256	180	1020
Ce22	2.0	4.0	7.2	256	400	800
Ce45	4.0	2.0	7.2	256	800	400
Ce84	5.5	0.5	7.2	256	1100	100
Ce-UiO-66	6.0	0.0	7.2	256	1200	0

The glass reactors were heated under stirring for 15 min at 100 °C using an aluminum heating block. After the synthesis the glass reactor was cooled down to room temperature and the precipitate was isolated by centrifugation. The mother liquor was decanted off and the MOF were re-dispersed and centrifuged two times in DMF (2

mL) and three times in acetone (2 mL). Finally, the MOF was dried in air at 70 °C. The addition of formic acid to the synthesis mixture worked as a modulator, slowing down the kinetics of the reaction and thus improving the crystallinity of the product. The nomenclature of the samples, Ce**xx**, stands for the percentage of Ce metal in respect of the total metal content of the MOF.

Zr-UiO-66 was synthesized following the procedure reported by Cavka et al.[22] Zirconium(IV) chloride (530 mg) and 1,4-benzenedicarboxylic acid (H_2BDC, 340 mg) were dissolved in N,N-dimethylformamide (DMF, 20 mL). This mixture was sealed in a steel autoclave and placed in an oven at 120 °C for 24 h. After the synthesis the solvothermal reactor was cooled down to room temperature and the precipitate was centrifuged. The mother liquor was decanted off and the product was re-dispersed and centrifuged two times in DMF (5 mL) and three times in acetone (5 mL). Finally, the MOF was dried in air at 70 °C.

2.1.4 Synthesis of Ce-UiO-66-ADC

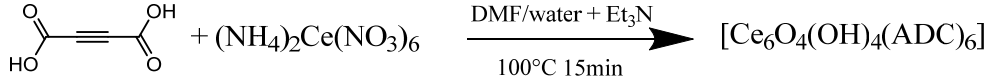

Cerium (IV) ammonium nitrate (98 %, $(NH_4)_2Ce(NO_3)_6$, Sigma-Aldrich), acetylenedicarboxylic acid (95 %, H_2ADC, TCI Chemicals), N,N-dimethylformamide (99 %, DMF, Sigma-Aldrich) and triethylamine (99 %, Et_3N, Sigma-Aldrich) were used as obtained. The synthesis procedure was optimized using high-throughput methods (section 1.2.1) starting from the one reported by Lammert et al.[54] in 2015 using different ditopic linkers, details about the optimization of the synthesis can be found elsewhere.[131,132] 644 mg of H_2ADC, 32 mL of DMF, 790 µL of triethylamine and 10.66 mL of 0.0533 M of Cerium(IV) Ammonium Nitrate (CAN) aqueous solution were added to a thick-walled glass tube with a screw cap which was closed and inserted into a pre-heated oven and kept at 100°C for 15 minutes. Product was then centrifuged and briefly washed with fresh acetone to let it dry at room temperature. The final yield was 32% based on the metal source and using the formula $[Ce_6O_4(OH)_4(ADC)_6]$. The addition of triethylamine to the synthesis mixture worked as a deprotonating agent to the linker, speeding up the reaction by a high degree. This is needed to improve the yield of the reaction and to avoid the linker decarboxylation (see section 3.4.5).

2.2 Experimental methods

2.2.1 X-Ray diffraction techniques

Single-crystal X-ray diffraction (SCXRD) data for the $Ce_2(NDC)_3(DMF)_2$ MOF were recorded on a Stoe IPDS diffractometer equipped with an image-plate detector using MoK_α radiation; a crystal was glued to the tip of a glass capillary and cooled down to about 153 K with a cold nitrogen blower. Direct methods implemented in the SHELXS-2013 code were used in order to solve the structure, while crystal structure refinement, using full-matrix least-squares algorithms, was done using SHELXL-2013.[133] All non-hydrogen atoms were refined with anisotropic displacement parameters while C-H atoms were positioned via a riding model and refined isotropically. Numerical absorption correction was carried out by using X-Shape and X-Red from the X-Area package.[134] Diffraction data of the $Ce_2(NDC)_3$, after desolvation, were acquired at 100 K using a Bruker D8 Venture diffractometer equipped with a Photon100 CMOS detector and using MoK_α radiation. Several crystals were screened for diffraction due to poor diffraction. The crystals showed signs of degradation, with visible cracks and opacity. The diffraction frames show very broad reflections and diffuse scattering. The Material Studio software package from Accelrys was used during the crystal structure pictures making.

The crystal structure of the $Ce_2(ADB)_3(DMA)_{3.4}$ was solved with single-crystal diffraction data collected using an Oxford Xcalibur CCD area detector diffractometer. Structure solution was performed by SIR2011[135] and refinement with full-matrix least-squares by SHELXL-2013.[133] Mercury was used for crystal structure drawing.[136]

Powder X-ray diffraction (PXRD) patterns of $Ce_2(NDC)_3(DMF)_2$, $Ce_2(ADB)_3(DMA)_{3.4}$ and Ce-UiO-66-ADC were taken with a Panalytical X'Pert PRO MPD diffractometer equipped with a CuK_α source operating in Debye-Scherrer geometry. Borosilicate glass capillaries with inner diameter of 0.5 mm were used as sample holders. Scattered photons were collected by a X'Celerator detector equipped with a Ni filter in order to attenuate K_β radiation. High-resolution diffractograms of pure Ce, pure Zr and $Zr_{3.54}Ce_{2.46}$-UiO-66 samples after desolvation at 180°C were conducted at the high-resolution powder diffraction beamline of the European Synchrotron Radiation Facility (ID22, ESRF, Grenoble, France).

Pawley and Rietveld refinements were carried out using the TOPAS-Academic[137] V5 software. Peaks were fitted using a Pseudo Voigt profile and all the diffractometers were modeled using a simple axial model.

2.2.2 Thermal analysis techniques

Variable temperature PXRD (VTXRD) measurements on $Ce_2(NDC)_3(DMF)_2$ were collected on a STOE Stadi P combi with CuK_α radiation in transmission geometry and equipped with a furnace; open quartz capillaries with an inner diameter of 0.5 mm were used as sample holders. The temperature program was set to measure a diffractogram every 25°C from RT to 600°C, waiting at each step 15 min at the setpoint before collecting data. The sample was heated at a rate of 3°C/min. Diffraction patterns of $Ce_2(ADB)_3(DMA)_{3.4}$ and Ce-UiO-66-ADC, instead, have been collected with a PW3050/60 X'Pert PRO MPD diffractometer from PANalytical working in Bragg-Brentano geometry, using as source a ceramic tube with a Cu anode. Scattered photons were collected by a X'Celerator detector equipped with Ni filter to attenuate K_β. Non-ambient chamber Anton Paar XRK900 with Be windows was used to collect the PXRD data in dynamic vacuum with a ramp rate of 3°C/min and the sample was held in an isothermal temperature for 25 min prior to every 2θ scan.

Thermogravimetric analysis (TGA) data were recorded with a TA instruments Q600 thermobalance in a dry air or N_2 flow (100 mL/min) with a ramp of 3°C/min from RT to 700°C working with about 10 mg of sample in an open alumina crucible for all the samples reported in the present document.

2.2.3 X-ray absorption spectroscopy

All XAS measurements except for those for Ce10 sample were performed at BM31 beamline[138] of European Synchrotron Radiation Facility (ESRF, Grenoble, France). The ring was operating in 7/8 multibunch mode with the current between 160 and 200 mA. All the measurements at BM31 were conducted in transmission mode using Si (111) double-crystal monochromator. Three ionization chambers were used for photon detection (30 cm long, 1 bar filing, 1 kV voltage), the third one being used for energy calibration with CeO_2 reference. Gas mixtures used for filling the ionization chambers and resulting absorption values are given in Table 6.

Table 6 – Filling of the ionization chambers for the XAS experiments.

Edge	Edge energy, eV	I_0 mixture	I_1 and I_2 mixture
Ce L_3 edge	5723	30% N_2 in He	10% Ar in He
Zr K edge	17998	30% Ar in He	10 % Kr in Ar
Ce K edge	40443	15% Kr in Ar	100% Kr

XAS spectra for Ce10 sample were collected at BM23 beamline of the ESRF. The experimental setup was similar to the one at BM31, except for the use of Si (311) monochromator for the measurements at Ce K-edge.

All MOFs were measured in the form of self-supporting pellets of 5 mm diameter, packed using the power achievable pressure. The mass of MOF powder for sample preparation was optimized by XAFSmass software.[139]

XAS data analysis was performed using Athena program for averaging and normalizing data and Artemis code for EXAFS fitting, both codes coming from Demeter package.[140] Scattering amplitudes and phase shifts were calculated by FEFF6[141] code bundled with Artemis.

2.2.4 Vibrational spectroscopy

Vibrational infrared spectra (FTIR) were collected in transmission mode using a Thermo Scientific Nicolet 6700 spectrometer equipped with a liquid N_2 cooled MCT detector on thin self-supporting pellets. Samples of $Ce_2(NDC)_3(DMF)_2$ and Ce-UiO-66-ADC were outgassed in dynamic high vacuum ($5 \cdot 10^{-4}$ mbar) at the reported temperature for in a homemade quartz cell equipped with KBr windows that allows also controlled dosages of gaseous probes (i.e. CD_3CN) in an *in-situ* manner.

Raman spectra were collected on a sample of Ce-UiO-66-ADC that was prepared and pretreated in the same manner as for the transmission FTIR measurements, albeit using another type of locally constructed airtight cell featuring a suprasil quartz cuvette in place of KBr windows. Raman spectra were recorded over a wavenumber range of 3200-100 cm^{-1} on a Renishaw inVia Raman microscope spectrometer in backscattering mode. A 785 nm diode laser was used for the excitation, and the scattered photons by were dispersed by a 1200 lines/mm grating monochromator and collected on a CCD camera whose collection optic was set at 20X objective summing up 20 scans with an exposition time of 20 s per step working at the 10% of the total laser power and using a rotating sample holder of local construction[142] to overcome the degradation of the sample under the beam.

2.2.5 Volumetric adsorption

A Micromeritics ASAP 2020 apparatus was used to measure both N_2 and CO_2 adsorption isotherms for all the materials studied in the present thesis. While for the measure at -196°C a classical liquid nitrogen dewar was used as isothermal bath, the data at -78°C was measured using a dry ice / acetone cold bath whose temperature was accurately measured with a Pt100 thermometer and then used to obtain the saturation pressure looking at the published phase diagram for carbon dioxide. For the CO_2 measurement in the 0°C-60°C range the temperature was kept stable by means of an isothermal water bath (Julabo F25). A local construction setup was employed which permitted us to thermally activate $Ce_2(NDC)_3(DMF)_2$ and $Ce_2(ADB)_3(DMA)_{3.4}$ materials (ramping at 5°C/min to the target temperature and keeping this temperature for 2 h) in dynamic vacuum and then measure the isotherms without exposing the sample to air.

3.Results and discussion

3.1 $Ce_2(NDC)_3(DMF)_2$

The synthesis procedure of $Ce_2(NDC)_3(DMF)_2$ described in section 2.1.1 was optimized by the means of high-throughput methods, also described earlier in the introduction in section 1.2.1 An optical micrograph of the as-synthesized compound is shown in Figure 12 below.

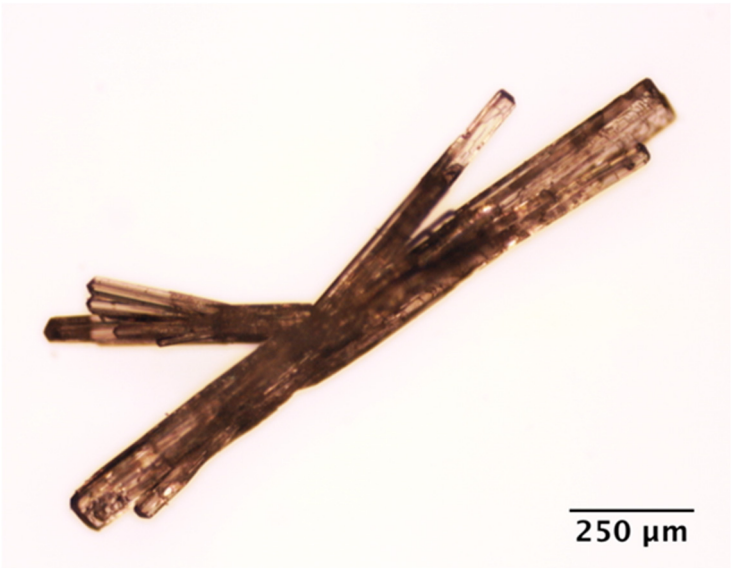

Figure 12 – Optical micrograph of $Ce_2(NDC)_3(DMF)_2$ crystals.

3.1.1 Thermal activation

$Ce_2(NDC)_3(DMF)_2$ was studied upon thermal treatment by means of TGA, VTXRD and in-situ FTIR spectroscopy. The data resulting from these experiments are enlisted below.

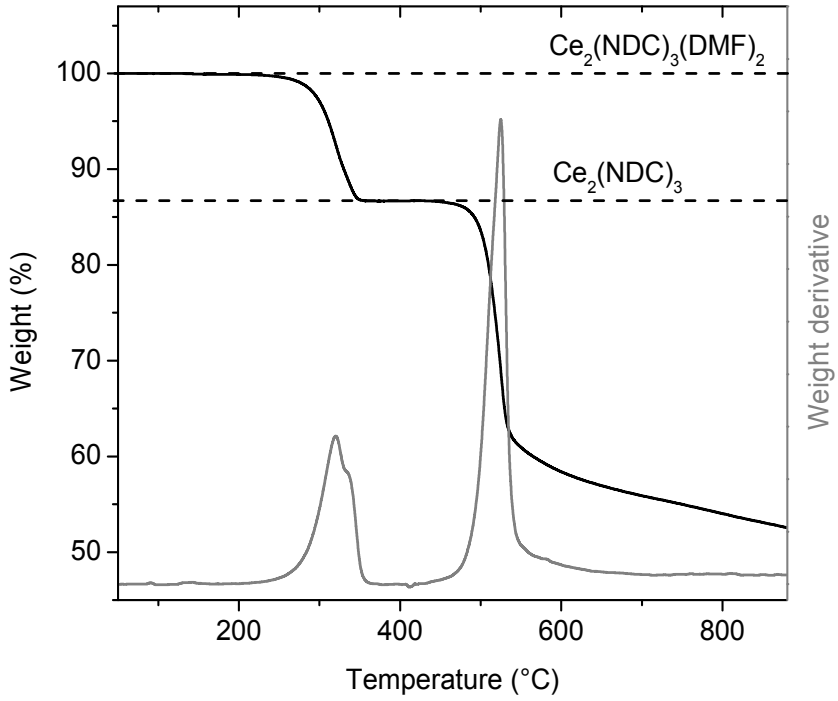

Figure 13 – TGA curve of $Ce_2(NDC)_3(DMF)_2$ in a dry nitrogen atmosphere (black), its derivative (DTA) is reported in grey color.

The TGA curve collected on $Ce_2(NDC)_3(DMF)_2$ is characterized by the presence of a steep weight loss at an onset temperature of 293°C that can be well assigned to the desorption of all the structural DMF molecules present to give $Ce_2(NDC)_3$. Such assignation is strongly suggested by a calculation made on the stoichiometry of the pristine compound: calculating the amount of weight that must change during the desorption of those DMF molecules one obtains a good agreement with the experiment (dashed lines in Figure 13). For this reason, a static temperature of 300°C was adopted to desolvate the pristine material and obtain $Ce_2(NDC)_3$ when needed for the other experiments (FTIR, SCXRD, XAS, adsorption measurements). At

higher temperatures the weight does not change till about 440°C. At an onset temperature of 502°C the material is decomposing (pyrolysis) yielding CeO_2 and coke-like species, as expected for the thermal decomposition of a Ce-MOF in an inert atmosphere.[36]

The FTIR spectrum collected on a thin self-supporting pellet of $Ce_2(NDC)_3(DMF)_2$ is reported in Figure 14. The same pellet was thermally activated at 300°C for 2 h under dynamic vacuum with a setup of local construction: this treatment leads to the desolvation into $Ce_2(NDC)_3$ as hypothesized from TGA data. The resulting spectrum is also shown in Figure 14.

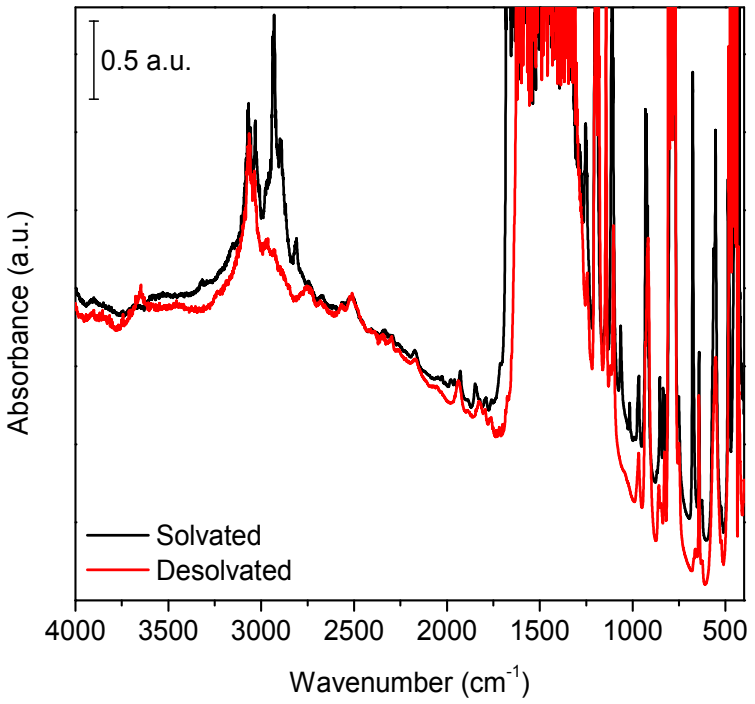

Figure 14 – FTIR spectra of $Ce_2(NDC)_3(DMF)_2$ (black line) and $Ce_2(NDC)_3$ (red line).

Very intense bands coming from the symmetric and asymmetric stretching of carboxylates are clearly visible in the 1630-1300 cm^{-1} range, as expected for a MOF. In the region below these signals, also called fingerprint region, a great number of bands is present due to complex vibrational modes involving mainly the naphthalenic

aromatic rings. Around 3000 cm^{-1} an absorption due to C-H stretching is clearly visible: while the band at 3070 can be undoubtedly assigned to the naphthalenic hydrogens, the one at 2930 cm^{-1} is due to aliphatic CHs coming from DMF.[143] This band is vanishing with thermal activation confirming the hypothesis drawn from the TGA data together with the diminishing of the shoulder at 1670 cm^{-1} due to the carbonyl stretching in DMF molecules. The fact that only signals coming from DMF are changing upon thermal activation is again suggesting the hypothesis for which the MOF can be successfully desolvated by such a treatment.

VTXRD data (Figure 15), complementarily to TGA and *in-situ* FTIR, are showing a similar behavior. Three different phases can be recognized from the patterns, which are enlisted below.

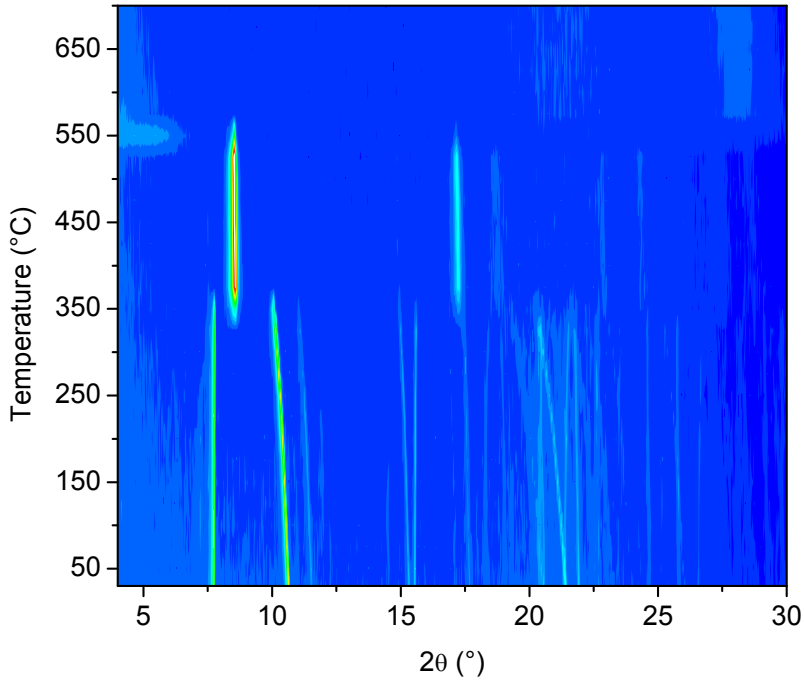

Figure 15 – VTXRD data collected on $Ce_2(NDC)_3(DMF)_2$ visualized as a contour plot. (λ = 1.5406 Å)

- From RT to 360°C: $Ce_2(NDC)_3(DMF)_2$
- From 360°C to 550°C: $Ce_2(NDC)_3$, as supported by TGA and FTIR data.

- Above 550°C: $Ce_2(NDC)_3$ pyrolysis to nano-sized CeO_2[36] and coke-like species.

PXRD Reflections clearly undergo a shift upon heating (before phase transformation associated to the loss of DMF molecules) that is caused by thermal expansion effects (the higher the temperature, the larger the cell parameter, the lower the angle of the diffraction signal). The $Ce_2(NDC)_3$ phase is probably crystallizing in a less symmetric space group, as the number of peaks that are visible is lower; for this phase no thermal effect on the cell parameters is visible till the MOF collapses. The difference in temperature between the phase transformation observed in TGA and FTIR experiments (at about 300°C) and the one happening here (360°C) is probably due to the different atmospheres used in these experiments i.e. a stream of inert gas for TGA and dynamic vacuum for TGA and FTIR, respectively, and static conditions for the VTXRD experiment. The crystalline structure of these compounds will be discussed in the following section.

3.1.2 Crystal structure

The crystal structures of the as-synthetized $Ce_2(NDC)_3(DMF)_2$ and fully desolvated $Ce_2(NDC)_3$ compounds, were determined from SC-XRD data and taking also into account the input coming from the EXAFS data about the atoms surrounding Ce cations. Table 7 reports the crystallographic data of both compounds.

Table 7 – Crystal data for $Ce_2(NDC)_3(DMF)_2$ and $Ce_2(NDC)_3$.

	$Ce_2(NDC)_3(DMF)_2$	**$Ce_2(NDC)_3$**
Formula	$C_{84}H_{64}Ce_4N_4O_{28}$	$C_{36}H_{18}Ce_2O_{12}$
Formula weight (g·mol^{-1})	2137.88	922.76
Crystal system	$Orthorombic$	$Trigonal$
Space group	$Pca2_1$	$P\bar{3}c1$
a (Å)	19.836(4)	11.845(5)
b (Å)	8.7339(17)	11.845(5)
c (Å)	45.451(9)	7.698(3)
α = β (°)	90	90
γ (°)	90	120
Cell volume (Å^3)	7874(3)	935.3(8)
Temperature (K)	153(2)	100(2)
Abs. coefficient (mm^{-1})	2.357	2.460
Calc. density (g·cm^{-3})	1.803	1.606
Z	4	2
Measured reflections	11957	108
R_{int}	0.0519	0.0727
No. of parameters	1082	29
R_1	0.0519	0.0729
wR (all data)	0.1317	0.1205
Largest. diff. peak (e·Å^{-3})	$-1.920 / 2.677$	$-0.555 / 0.450$

The solvated compound, $Ce_2(NDC)_3(DMF)_2$, crystallizes in an orthorhombic space group with a structure that consists of distorted pentagonal bipyramidal Ce(III) cations coordinated by carboxylates coming from different linkers and one oxygen atom coming from an adsorbed DMF molecule (see Figure 16 for a structure representation).

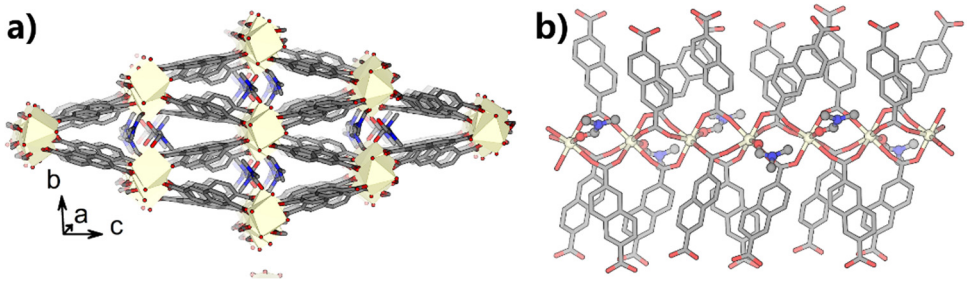

Figure 16 – Pictorial representation of the crystal structure $Ce_2(NDC)_3(DMF)_2$, Color code: Ce (dark yellow), O (red), C (gray), N (blue), H (omitted)

Every Ce(III) cation is sharing three different carboxylate groups, coming from the naphthalenic moieties, to form extended chains parallel to the a-axis. The same linker molecules are forming inter-chain bridges to give a network structure with diamond-shaped channels parallel to the Ce(III) chains (Figure 16b).

Upon desolvation by thermal treatment in dynamic vacuum (300°C for 2 h), see VTXRD and TGA data reported below, the crystal structure of $Ce_2(NDC)_3(DMF)_2$ undergoes a phase transition characterized by the loss of the DMF molecules and thus becomes $Ce_2(NDC)_3$. The quality of the diffraction data collected on a single-crystal of $Ce_2(NDC)_3$ is significantly worsened from the one collected on $Ce_2(NDC)_3(DMF)_2$ and consists of very diffuse diffraction peaks (see also Figure 19). These signals are also broadening with the scattering angle, giving readable diffraction data only to 1.3 Å. Nevertheless data reduction with the hexagonal space group P-3c1 (see Table 7 for details) proceeded without issues giving a structure depicted in Figure 17 below.

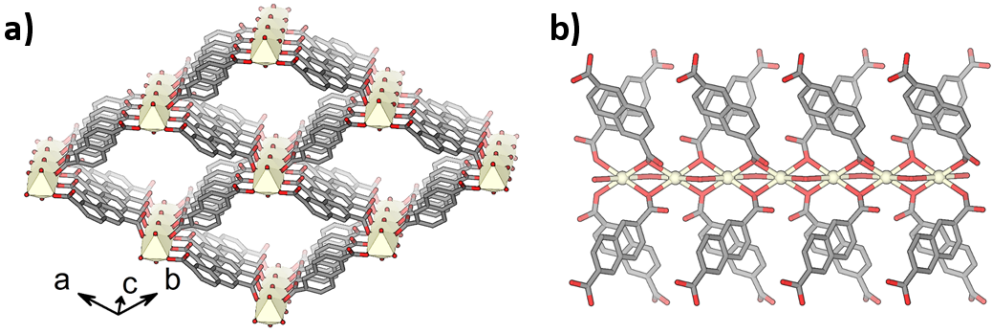

Figure 17 – Pictorial representation of the crystal structure $Ce_2(NDC)_3$, Color code: Ce (dark yellow), O (red), C (gray), N (blue), H (omitted).

The solved structure for $Ce_2(NDC)_3$ shows a hexagonal crystal structure consisting of linear chains of Ce cations, as for the solvated structure, aligned to the crystal c-axis. As there is disorder in the linker structure, that cannot be resolved directly, the

occupancies of the linker has been set to one half in order to accommodate also a linker that bridges two Ce chains in a way that "closes the pores" shown in Figure 17a. These occupancies factors are in accordance to the proposed stoichiometry of the compound, $Ce_2(NDC)_3$, that is also confirmed by TGA measurements (see Figure 13) Figure 18 represents the structure of the desolvated compound plotting all linker atoms, even with non-integer occupancies.

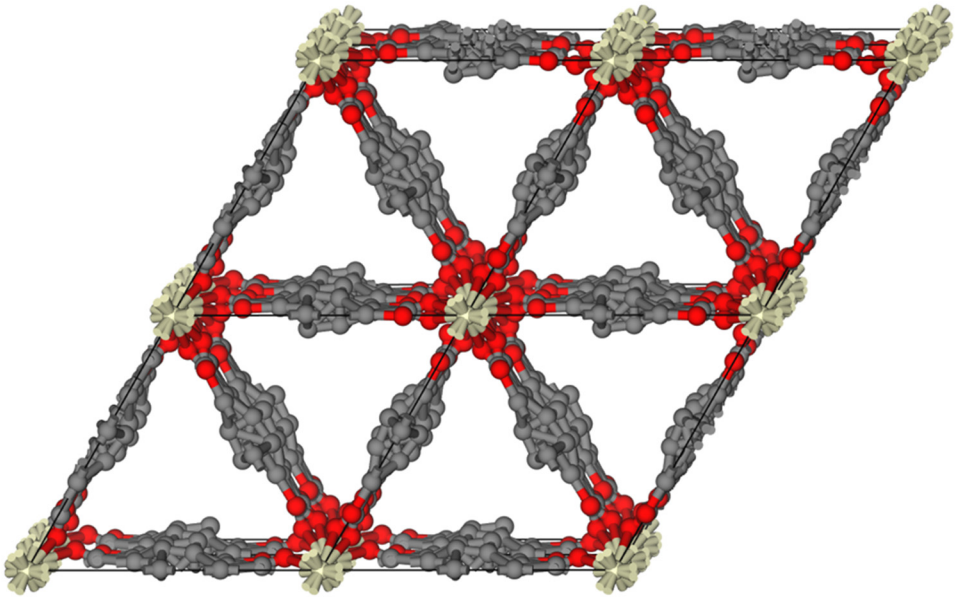

Figure 18 – Pictorial representation of the crystal structure of $Ce_2(NDC)_3$ viewed along the c-axis, showing all possible positions of the atoms.

Considering the disorder associated to the linker positions, the presence of diamond-shaped channels, as present in the solvated structure, must be declined and instead triangular channels (as shown in Figure 18) must be considered. It has to be noticed what other MOFs characterized by a flexible structure, such as MIL-53[144,145], upon adsorption of gas molecules are not showing such rearrangement of its constituents upon thermal activation.

With the aim to demonstrate that the proposed structures found by SCXRD are the only crystalline phases present in the bulk samples Pawley PXRD refinements were done on the diffractograms using the unit cells coming from Table 7. The results are enlisted in Figure 19 and Table 8 below.

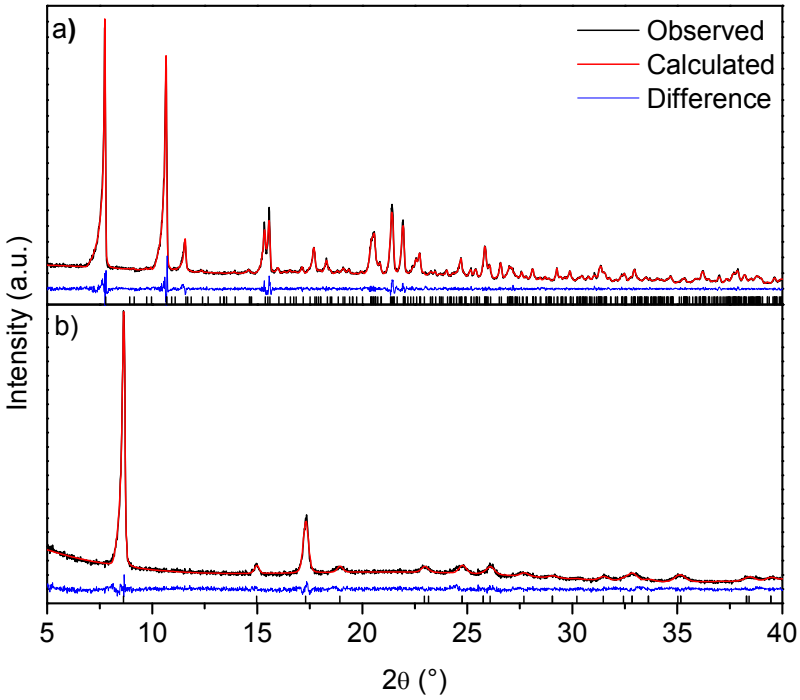

Figure 19 – Pawley fits on PXRD patterns of $Ce_2(NDC)_3(DMF)_2$ (a) and $Ce_2(NDC)_3$ (b). Observed, calculated and residuals are drawn respectively in black, red and blue lines, allowed reflections are reported by black ticks. (λ = 1.5406 Å).

Table 8 – Comparison between cell parameters obtained by SC-XRD and Pawley refinements on $Ce_2(NDC)_3(DMF)_2$ and $Ce_2(NDC)_3$ PXRD patterns

$Ce_2(NDC)_3(DMF)_2$	**Pawley**	**SC-XRD**
a (Å)	19.791(3)	19.836(4)
b (Å)	8.865(11)	8.7339(17)
c (Å)	45.392(6)	45.451(9)
Volume ($Å^3$)	7964(2)	7874(3)
$Ce_2(NDC)_3$	**Pawley**	**SC-XRD**
a (Å)	11.823(2)	11.845(5)
b (Å)	11.823(2)	11.845(5)
c (Å)	7.675(4)	7.698(3)
Volume ($Å^3$)	929.1(5)	935.3(8)

As it is evident from the fit results, the cell parameters coming from the powder diffraction data are in accordance with those of single-crystal data refinements. It is relevant to notice also that while single-crystal data is collected at low temperatures (100-150 K), the powder one is measured at room temperature: for this reason such differences in cell lengths have to be accounted to a thermal expansion effect. No new crystalline phase can be recognized looking at the fits in Figure 19 confirming the purity of the synthesized compounds.

3.1.3 X-ray absorption spectroscopy

X-ray absorption spectroscopy (XAS) was exploited in studying this material as i) a method to determine the oxidation state of Ce before by means of XANES spectroscopy before and after thermal activation and, more importantly, ii) confirm the structural results coming from SC-XRD through EXAFS fitting analysis. Figure 20 shows XANES spectra of both $Ce_2(NDC)_3(DMF)_2$ and $Ce_2(NDC)_3$ and their comparison with Ce(III) and Ce(IV) standards.

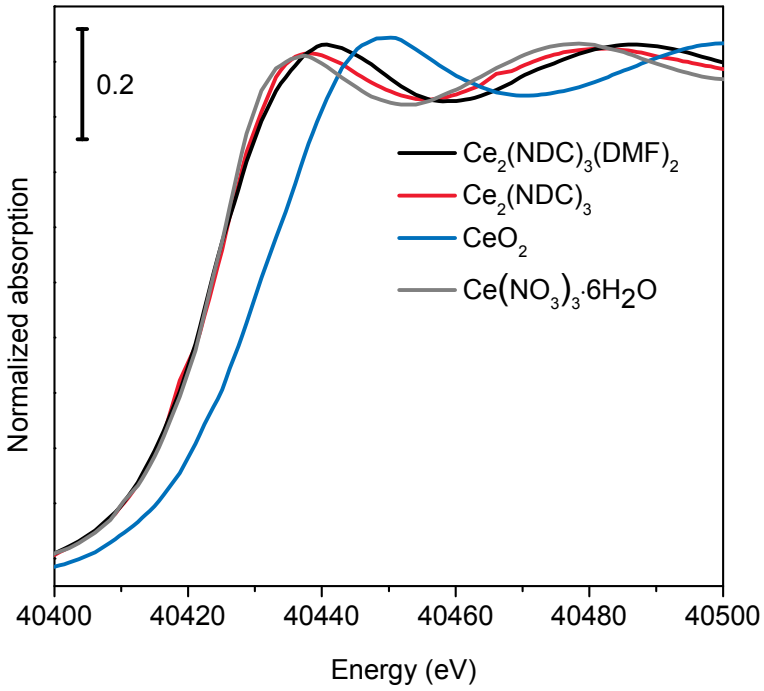

Figure 20 – Ce K-edge XANES spectra of $Ce_2(NDC)_3(DMF)_2$ (black line) and $Ce_2(NDC)_3$ (red line) compared to those of Ce(IV) oxide and Ce(III) nitrate hexahydrate (respectively blue and grey curves).

The absorption edges of both $Ce_2(NDC)_3(DMF)_2$ and $Ce_2(NDC)_3$ correspond to the one of Ce(III) comparing it with the Ce(III) nitrate hexahydrate standard. This indicates the conservation of the 3+ oxidation state during the desolvation of the material, despite the phase transition.

As a complement to the long-range structural analysis done with SC-XRD (and its limitations due to inherent disorder) Ce K-edge EXAFS spectra were collected for the solvated and desolvated materials. As starting point for the structural EXAFS fitting of the atoms surrounding Ce, the crystal structure coming from X-ray diffraction was used. To increase the reliability of the fit the scattering paths from Ce atoms to light atoms were grouped in three O and three C shells reducing the number of parameters used in the fitting process. Being Ce-Ce a significant scattering path (due to the high Z of Ce), this path has been included in the model for $Ce_2(NDC)_3$. EXAFS fitting results are shown in Figure 21 and in Table 9 below.

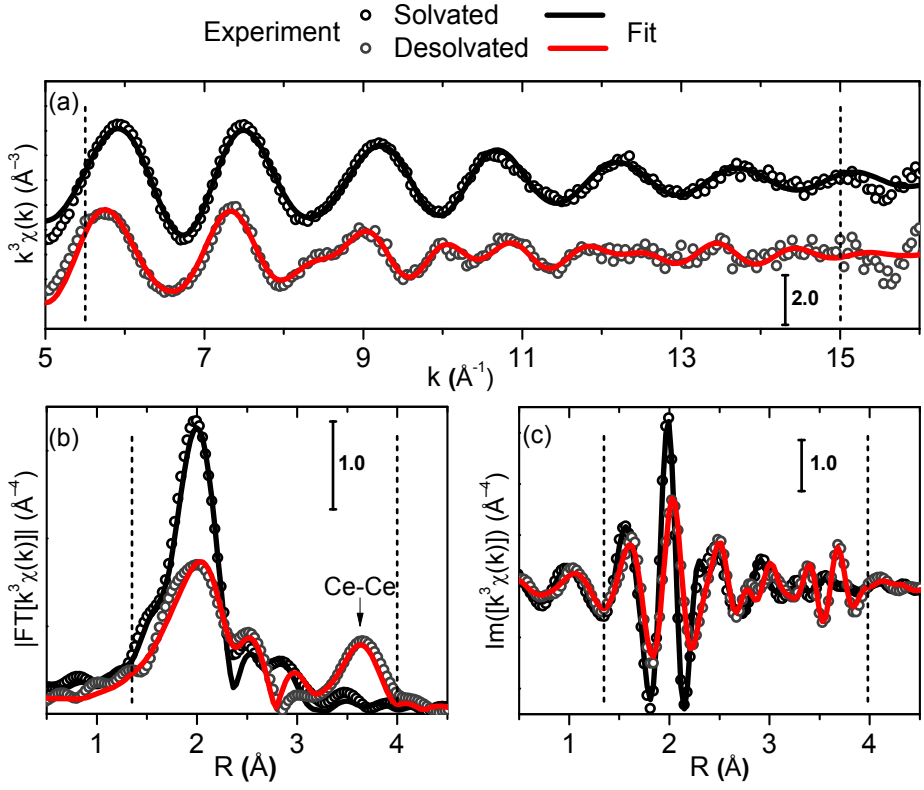

Figure 21 – Ce K-edge EXAFS spectra of $Ce_2(NDC)_3(DMF)_2$ and $Ce_2(NDC)_3$ (dots). The fit results, spectra (a), magnitude (b) and imaginary part (c) are shown by black and red lines for the solvated and the desolvated compounds, respectively.

Table 9 – Fitting results of the Ce K-edge EXAFS spectra for $Ce_2(NDC)_3(DMF)_2$ and $Ce_2(NDC)_3$.

Parameter	$Ce_2(NDC)_3(DMF)_2$	$Ce_2(NDC)_3$
R-factor	0.02	0.03
Fitting range in k, $Å^{-1}$	5.5 – 15	
Fitting range in R, Å	1.35 – 4	
N_{ind}	15.7	
N_{par}	5	9
S_0^2	1.0	1.0
ΔE	-0.3(1.7)	2.3(2.8)
N_{O1}	2.33	3
R_{O1}, Å	2.40(1)	2.44(1)
$\sigma^2_{O1,}$ $Å^2$	0.006(1)	0.009(1)
N_{O2}	2.33	3
R_{O2}, Å	2.43(1)	2.49(1)
$\sigma^2_{O2,}$ $Å^2$	0.006(1)	0.010(1)
N_{O3}	2.33	3
R_{O3}, Å	2.46(1)	2.53(1)
$\sigma^2_{O3,}$ $Å^2$	0.006(1)	0.010(1)
N_{C1}	2.33	3
R_{C1}, Å	3.28(2)	2.98(2)
$\sigma^2_{C1,}$ $Å^2$	0.004(2)	0.005(1)
N_{C2}	2.33	3
R_{C2}, Å	3.36(2)	3.46(3)
$\sigma^2_{c2,}$ $Å^2$	0.004(2)	0.006(1)
N_{C3}	2.33	3
R_{C3}, Å	3.43(2)	4.15(9)
$\sigma^2_{C3,}$ $Å^2$	0.004(2)	0.006(1)
N_{Ce}	-	2
R_{Ce}, $Å^2$	-	3.87(2)
$\sigma^2_{Ce,}$ $Å^2$	-	0.009(1)

The EXAFS fitting confirmed the structural features observed by SC-XRD with good R-factors and reasonable parameters for both $Ce_2(NDC)_3(DMF)_2$ and $Ce_2(NDC)_3$. The Ce-Ce (Figure 21) distance can be observed only for $Ce_2(NDC)_3$ as with thermal activation they become closer (3.87(2) Å by EXAFS vs. 3.849(2) Å from SC-XRD). As concerns Ce-O and Ce-C distances a general disordering (i.e. broadening of the range span of those bonds) is observed upon desolvation. This can be correlated with the strain associated to the removal of the solvent from the pores and the subsequent rearrangement of the crystal structure.

3.1.4 Adsorption properties

In order to measure the surface area and the porosity of $Ce_2(NDC)_3$, N_2 was dosed at -196°C with an automatic volumetric apparatus in order to measure an adsorption isotherm. The results (reported in Figure 22) show a nearly negligible adsorption in the whole pressure range (0-1 p/p_0 range) indicating nil surface area or porosity whatever the model used to reduce this data (e.g. Langmuir or BET models).

CO_2 was dosed at a temperature of -78°C as an alternative probe to N_2 in order to address the end of measuring a specific surface area on $Ce_2(NDC)_3$ giving isotherms reported in Figure 22.

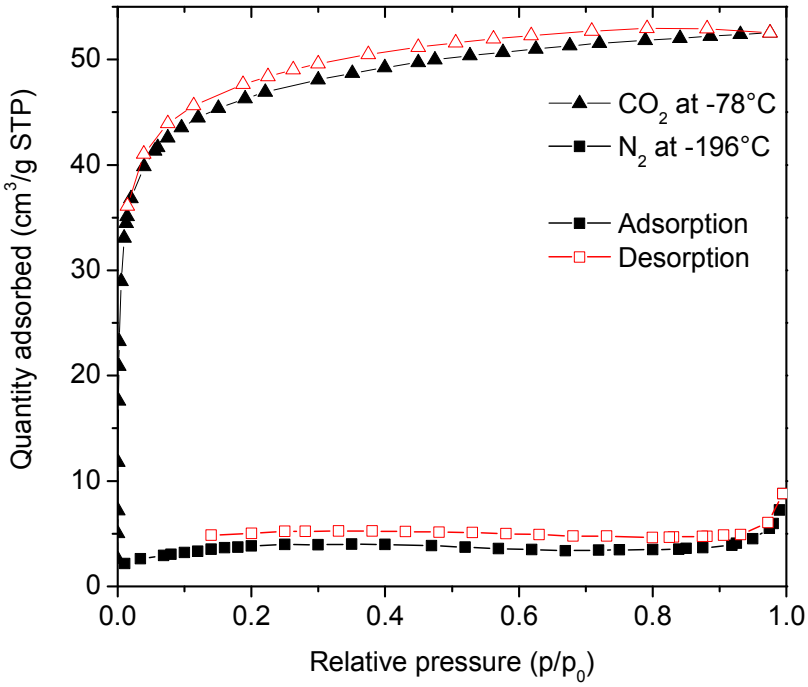

Figure 22 – $Ce_2(NDC)_3$ adsorption isotherms of N_2 at -196°C and CO_2 at -78°C. The two molecules are represented by squares and triangles, respectively. Adsorption branches is reported by solid black symbols while the desorption one is represented by open red symbols.

The adsorption isotherm of CO_2 can be assigned to a Type I^{100}, typical of microporous materials.

Such results indicate that $Ce_2(NDC)_3$ is characterized by a kind of porosity that cannot be traditionally determined by N_2 adsorption at -196°C. The application of BET and Langmuir models in order to extract a specific surface area gave results enlisted in Table 10 .

Table 10 – Specific surface area values measured on $Ce_2(NDC)_3$.

Probe	**BET (m^2/g)**	**Langmuir (m^2/g)**
N_2 at -196°C	–	–
CO_2 at -78°C	170(3)	222(1)

It must be considered that the application of CO_2 in the determination of specific surface area and porosity of polar materials, like MOFs and siliceous porous materials (e.g. mesoporous silica like SBA-15 or MCM-41 or zeolites) is not recommended[100,146,147] as the type of interaction that is established between the probe and the surface of the material is too specific, principally due to the high quadrupolar moment of CO_2.

A series of hypotheses for which the surface area was zero for N_2 and not for CO_2 can be drawn:

- The kinetic diameter of CO_2 is smaller than the one of N_2: in case of ultra-microporous material carbon dioxide can enter in pores where nitrogen cannot.
- The experiment with CO_2 is done at a temperature which is substantially higher than the one of liquid nitrogen, being 118 K higher. For this reason the diffusion kinetics of carbon dioxide can improve significantly. In this case the nitrogen isotherm must be considered not at equilibrium.
- This particular material, $Ce_2(NDC)_3$, is characterized by a phase transformation that occurs at the temperature of -196°C which converts it into a non-porous one. In order to catch this an X-ray diffraction experiment must be carried out at the temperature of liquid nitrogen. Such an experiment cannot be performed with the equipment currently available.

Apart from the specific surface area and porosity measurements the uptake performances were measured by volumetric CO_2 adsorption measurements, reported below in Figure 23.

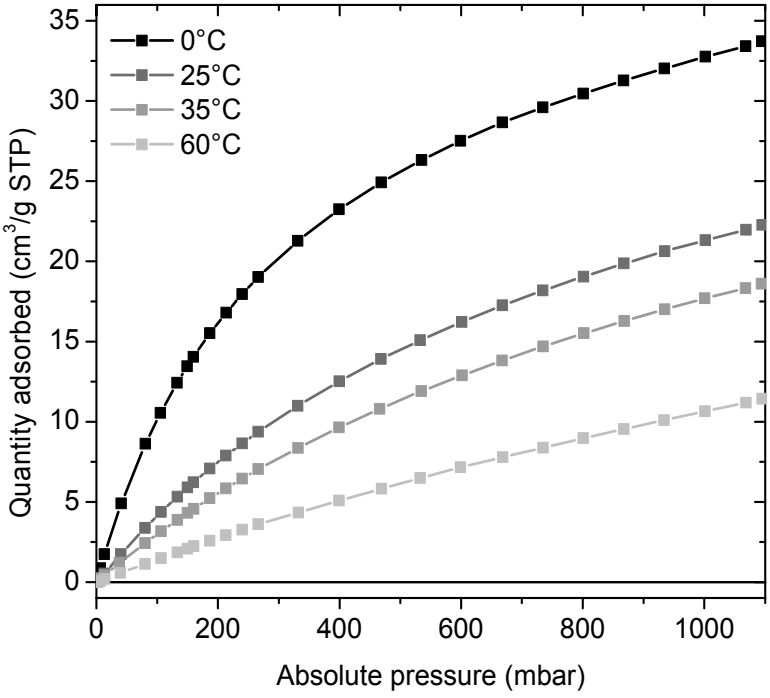

Figure 23 – CO_2 adsorption isotherms of $Ce_2(NDC)_3$ collected at different temperatures. Desorption branches (superimposable to adsorption ones) are omitted for the sake of clarity.

$Ce_2(NDC)_3$ adsorbs a not negligible amount of CO_2 at around room temperature. As these uptakes are not in the same order of magnitude of those ones measured on the best candidate for CO_2 storage and capture porous materials (i.e. UTSA-16[148] or Mg-MOF-74[109]), this material cannot be unfortunately proposed for such applications.

3.2 $Ce_2(ADB)_3(DMA)_{3.4}$

The synthesis procedure of $Ce_2(ADB)_3(DMA)_{3.4}$ described in section 2.1.2 was optimized by the means of high-throughput methods, also described earlier in the introduction in section 1.2.1. An optical image of the product is shown in Figure 24.

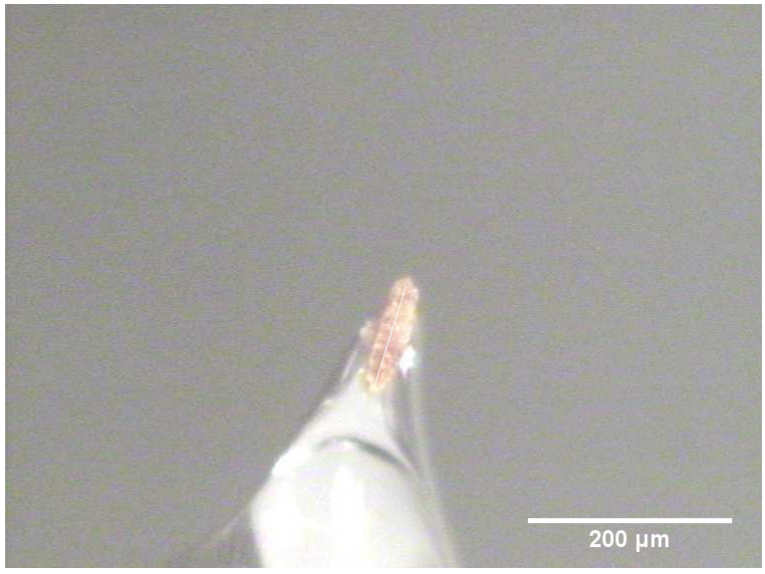

Figure 24 – Optical image of the crystal of $Ce_2(ADB)_3(DMA)_{3.4}$ selected for the SCXRD experiment.

3.2.1 Crystal structure

By looking at the solved crystal structure (Table 11 and Figure 25) the materials shows a typical coordination polymer structure with bonds between carboxylates and Ce cations. Such atoms build Ce-O-Ce chains aligned to the c-axis of the crystal structure. Linker molecules, instead, work as a bridge from those chains forming a 3D structure with one-dimensional long channels aligned in the same direction of the Ce chains (Figure 25)

Table 11 – Crystal data for $Ce_2(ADB)_3(DMA)_{3.4}$

	$Ce_2(ADB)_3(DMA)_{3.4}$
Formula	$C_{21}H_{12}CeN_3O_6$
Formula weight (g·mol^{-1})	542.46
Crystal system	*Monoclinic*
Space group	$P2_1/n$
a (Å)	16.238(3)
b (Å)	8.858(3)
c (Å)	21.124(5)
α = γ (°)	90
β (°)	96.47(2)
Cell volume (Å^3)	3019.0(13)
Temperature (K)	293(2)
Abs. coefficient (mm^{-1})	1.537
Calc. density (g·cm^{-3})	1.193
Z	4
Measured reflections	9577
R_{int}	0.2170
No. of parameters	304
R_1	0.2170
wR (all data)	0.1378
Largest. diff. peak (e·Å^{-3})	−1.937 / 3.530

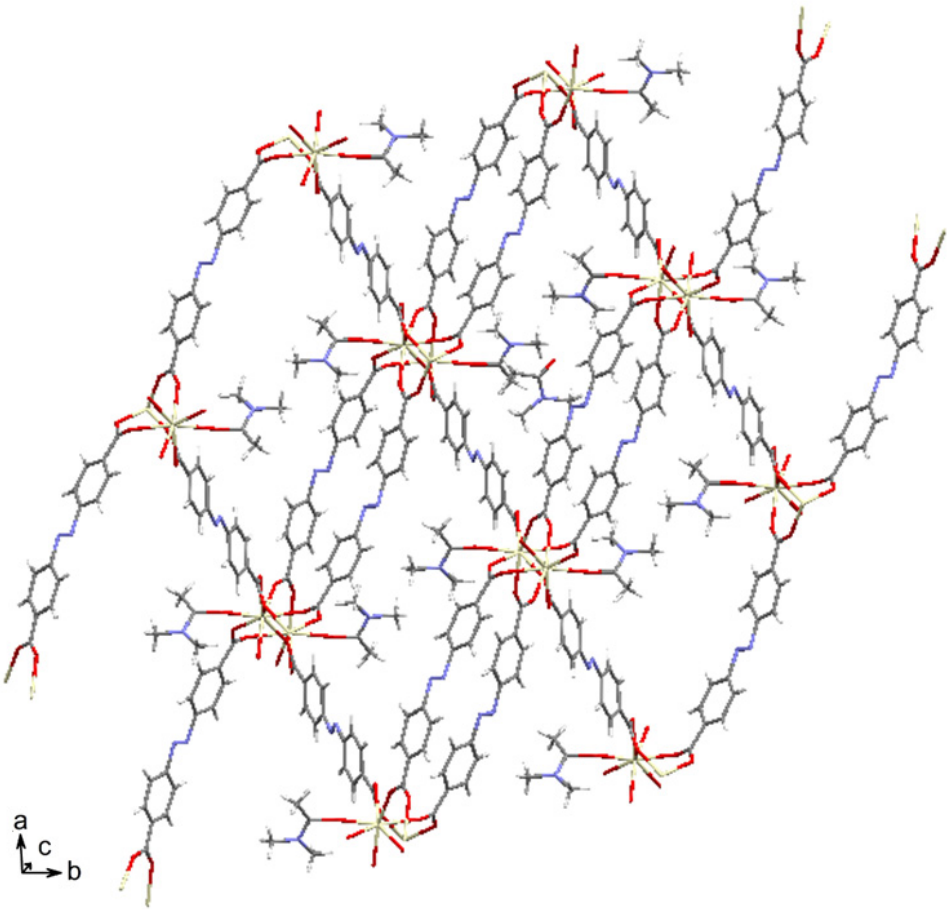

Figure 25 – Structural representation of $Ce_2(ADB)_3(DMA)_{3.4}$. c-axis is perpendicular to the figure. Cerium, carbon, nitrogen, oxygen and hydrogen atoms are depicted respectively in yellow, black, blue, red and white.

Two crystallographic independent DMA molecules are present in the structure: one directly coordinated to Ce atoms through a dative bond and one in the middle of the pore. While the occupancy factor of the latter DMA molecule has been refined to 1, the one directly coordinated to the metal site has been refined only to 0.7, explaining the 3.4 stoichiometric factor associated to DMA molecules observed in the structural formula.

Looking at the Pawley refinement done on the powder diffraction pattern in Figure 26 no new further crystalline phase different from the monoclinic one can be observed. Beside the purity of the synthesized compound such data is indicating also that the single crystal used for the structure solution is representative of the whole powder.

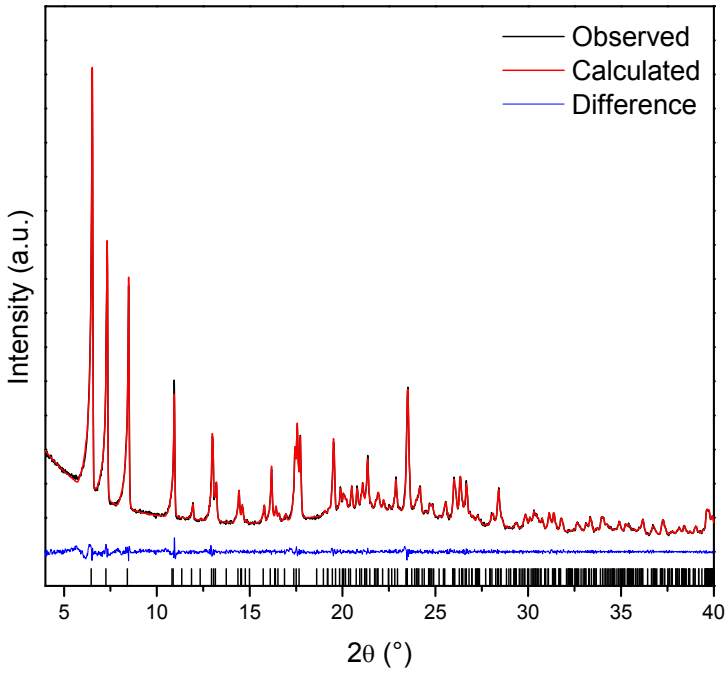

Figure 26 – Pawley fit on PXRD pattern of $Ce_2(ADB)_3(DMA)_{3.4}$. Observed, calculated and residuals are drawn respectively in black, red and blue lines, allowed reflections are reported by black ticks. (λ = 1.5406 Å).

Table 12 – Comparison between cell parameters obtained by SC-XRD and Pawley refinements on $Ce_2(ADB)_3(DMA)_3$. PXRD pattern.

$Ce_2(ADB)_3(DMA)_{3.4}$	**Pawley**	**SC-XRD**
a (Å)	16.371(2)	16.238(3)
b (Å)	8.875(2)	8.858(3)
c (Å)	21.142(3)	21.124(5)
β (°)	96.911(2)	96.47(2)
Volume ($Å^3$)	3049.51(8)	3019.0(13)

The slight discrepancy between the cell volume measured by SCXRD and Pawley refinement may be due to the small dimensions of the measured crystal (especially along one crystal axis) which is causing a low accuracy in the determination of one of the parameters. The data coming out from the Pawley refinement has to be considered as the most accurate, as in powder diffraction a virtually infinite number of different crystals contributes to the statistics of the measured values.

3.2.2 Thermal activation

The behavior of $Ce_2(ADB)_3(DMA)_{3.4}$ upon thermal treatment was studied by the means of TGA (in a flow of nitrogen or dry air) and VTXRD (in dynamic vacuum). Figure 27 reports the TGA curves obtained on $Ce_2(ADB)_3(DMA)_{3.4}$.

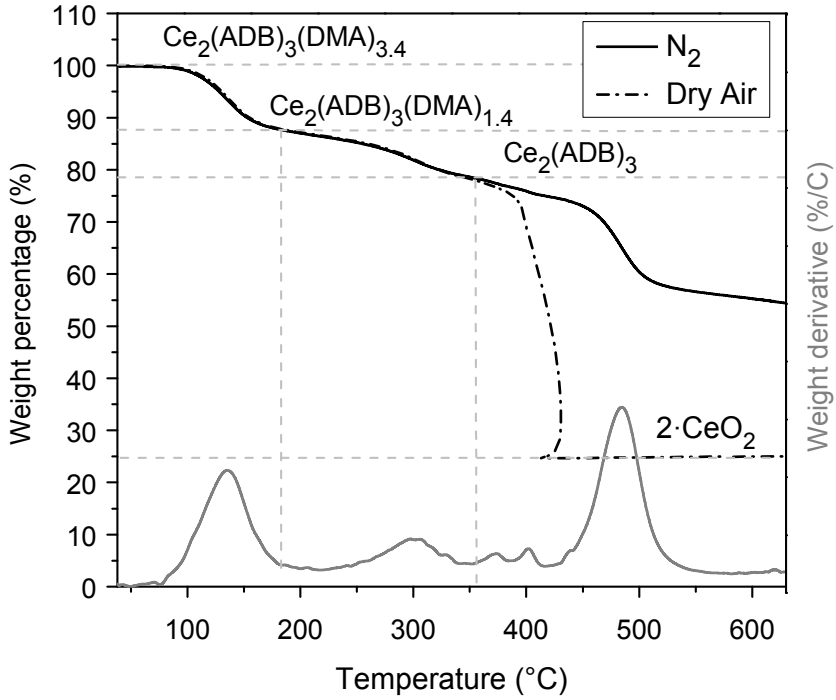

Figure 27 – TGA curve collected on $Ce_2(ADB)_3(DMA)_{3.4}$ in a N_2 flow (solid line) and dry air flow (dashed line). Derivative of TGA data for the N_2 flow is reported as a grey line. Dashed grey lines represents the relative formula weights of the written compounds.

TGA curves collected in different atmospheres (nitrogen and dry air) are superimposable up to 350°C. Above this temperature, they separate as the organic part of the MOF, in presence of dry air, burns to give carbon dioxide and water vapor yielding CeO_2 as observed for other Ce-based MOFs[36] and already observed for $Ce_2(NDC)_3(DMF)_2$. On the other hand, in nitrogen flow the MOF is decomposing into coke-like species and again CeO_2. These hypotheses are supported by the color of the material after the TGA measurement: black for the nitrogen one, and pale yellow for the one made in presence of oxygen.

Starting from this hypothesis, one can consider the ratio between the formula weights of the pristine compound and the cerium dioxide to be linked by the following combustion reaction:

$$Ce_2(ADB)_3(DMA)_{3.4} \xrightarrow{\Delta+O_2} 42\ CO_2 \uparrow +12\ H_2O \uparrow +3\ N_2 \uparrow +2\ CeO_2$$

Considering the relative mass of the sample after 450°C in air being only CeO_2 (plateau at 24.9%) it is possible to calculate the relative weight of the MOF that has reacted to give the oxide. By means of such calculation one obtain a value of about 100%, extremely close to the experimental one. This evidence strongly supports the correctness of the proposed unit formula coming from the SCXRD structure solution.

Working a similar way it is possible to assign the weight losses observed in the region between room temperature and the combustion temperature (395°C). The first weight loss, appearing in a temperature range between 110°C and 180°C can be modeled by means of the following equation:

$$Ce_2(ADB)_3(DMA)_{3.4} \xrightarrow{\Delta} Ce_2(ADB)_3(DMA)_{1.4} + 2\ DMA \uparrow$$

The accordance between the experimental value of the weight (87.8%) and the calculated one (87.4%) is good and permits to assign this weight loss to the desorption of the DMA molecules present inside the pores.

The other DMA molecules are desorbed at a higher temperature, between 250°C and 350°C, as modeled by the following chemical equation:

$$Ce_2(ADB)_3(DMA)_{1.4} \xrightarrow{\Delta} Ce_2(ADB)_3 + 1.4\ DMA \uparrow$$

Again a good agreement between the observed value (78.4%) and the theoretical value (78.1%) permits to assign this weight loss to the desorption of the DMA molecules directly coordinated to Ce cations. It is relevant to notice that these TGA data are confirming very strongly the stoichiometric number of DMA molecules refined by SCXRD method (which is a weaker datum, in this sense, mainly for being such a refinement linked to the idiosyncrasies of the crystallographer who is running the calculations) and also their speciation in two different families: a weakly and a strongly adsorbed one.

Such desolvation reactions were also studied by means of variable-temperature powder diffraction (VTXRD) in dynamic vacuum, giving results reported in Figure 28.

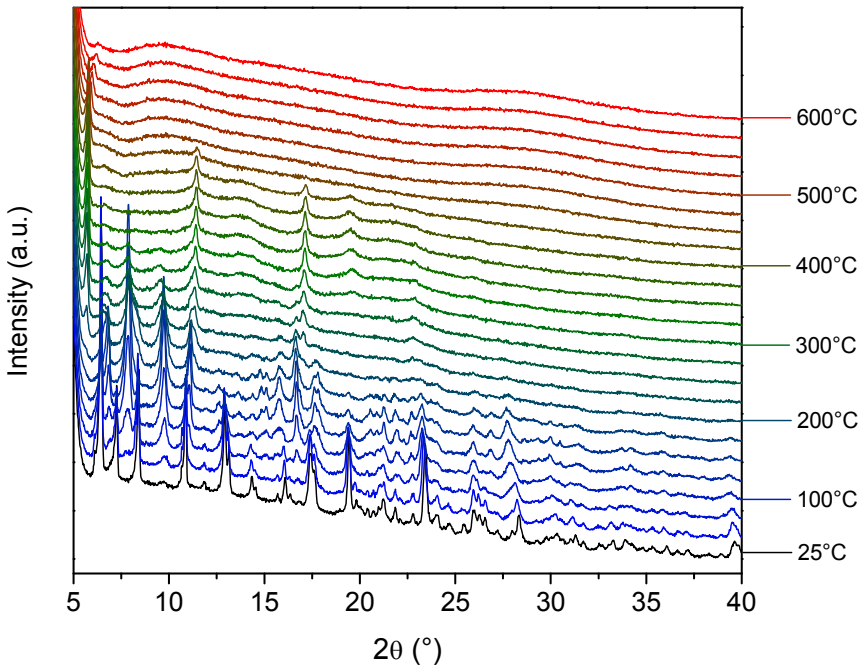

Figure 28 – VTXRD data collected on $Ce_2(ADB)_3(DMA)_3$.. (λ = 1.5406 Å)

The black curve reported in Figure 28, recorded at room temperature, is superimposable to the one reported in Figure 26 indicating that no phase transformation is happening at room temperature due to the dynamic evacuation. Upon heating up to 600°C three different phase transformations are visible in the patterns. The first one, starting at 50°C (see the peak at 9.8°) and being completed at 150°C can be linked to the first weight loss observed in TGA and assigned to the desorption of the first 2 DMA molecules loosely adsorbed in the pore system. A second phase transformation starting at 225°C and ending at 300°C can be similarly reconducted to the loss of the DMA molecules directly coordinated to the Ce metal sites. Above this temperature a collapse of the crystal structure is observed to give rise to amorphous (or nanocrystalline) solids. At temperatures above this amorphization a broad halo around 28° can be seen: this signal, being the most intense diffraction peak of crystalline CeO_2,[27] can be assigned to nanocrystalline cerium

dioxide coming from the pyrolysis of the MOF. In order to look at the relevant diffractograms collected in the variable-temperature PXRD experiments only five curves are shown in Figure 29 below:

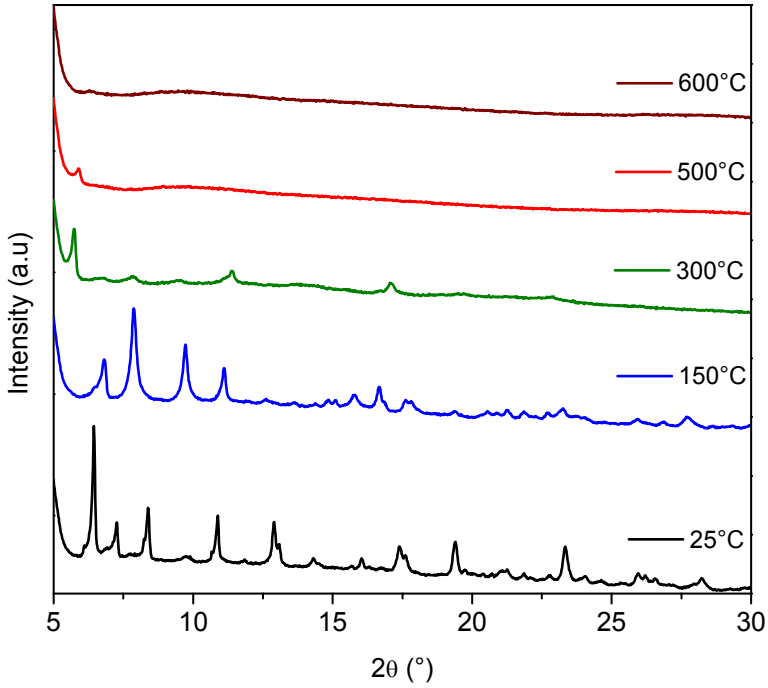

Figure 29 – Selection of five different diffractograms on $Ce_2(ADB)_3(DMA)_{3.4}$ from the VTXRD experiment at the temperatures of 25°C (black), 150°C (blue), 300°C (green), 500°C (red) and 600°C (brown) (λ = 1.5406 Å).

As noticeable from the curves in Figure 29 two new different crystalline phases are formed during the heating of $Ce_2(ADB)_3(DMA)_{3.4}$ in dynamic vacuum: as for their diffraction peaks in the low-angle region of the diffractogram they have crystalline cells with dimensions probably similar to those of $Ce_2(ADB)_3(DMA)_{3.4}$ which has been solved with single-crystal diffraction techniques. The one formed at 150°C having a number of peaks comparable to the pristine one is probably characterized by a similar space group (i.e. with a similar number of symmetry elements). The crystalline phase formed at temperatures above 300°C, having a substantially lower number of reflections, is probably belonging to a higher-symmetry space group. As the overall intensity of the diffraction signal is severely lowered in this final phase the general crystallinity of the sample is probably lost in the final phase

transformation. Despite many attempts the solution, of the crystal phases formed at high temperatures by single-crystal diffraction was not successful for the moment. This can be due to many reasons: i) after thermal activation the crystals become extremely sensitive to air moisture, decomposing in the time scale of minutes in air; ii) a general lower crystallinity that broadens and weakens the diffraction signals; iii) the disordering of the structure. A session of single-crystal diffraction measurements at a synchrotron source is scheduled in order to try to solve those crystal structures.

3.2.2 Adsorption properties

In order to measure the surface area and the porosity of $Ce_2(ADB)_3(DMA)_{3.4}$ a series of adsorption isotherms of N_2 at 77K (Figure 30) and of CO_2 (Figure 31) at 0°C were collected after a thermal activation in dynamic vacuum (for a duration of 3 h each) at different temperatures. For each adsorptive a different aliquot of powder was activated at increasing temperatures in a consecutive way.

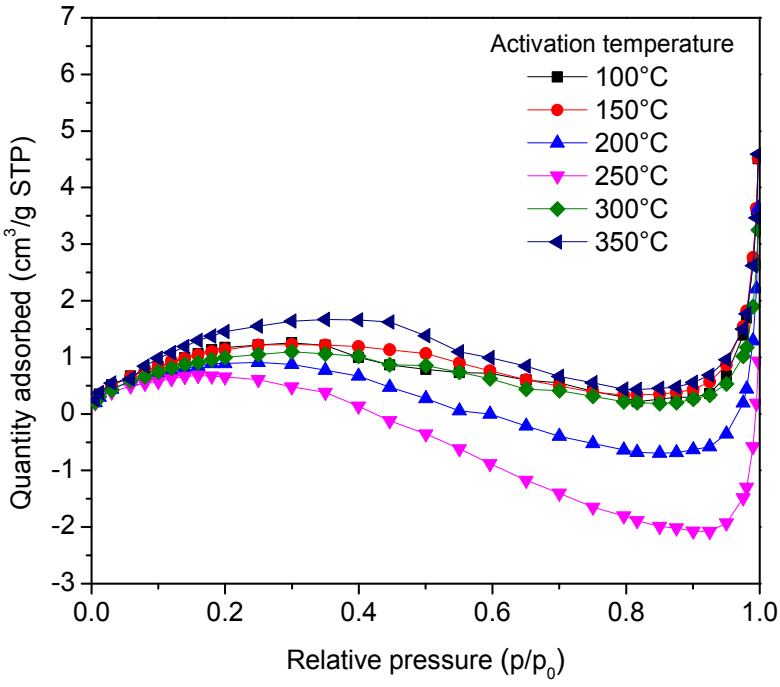

Figure 30 – -196°C N_2 adsorption isotherms collected on $Ce_2(ADB)_3(DMA)_{3.4}$. Desorption branches are omitted for the sake of clarity.

As the amount of adsorbed nitrogen is quite negligible for the all isotherms, $Ce_2(ADB)_3(DMA)_{3.4}$ cannot be considered porous for nitrogen at -196°C. The adsorbed amount is so little that the isotherms are dominated by the error and this causes them to be not strictly increasing (as expected for every adsorption isotherm) and even becoming negative. It has to be noticed that as a microporosity (and thus a Type I isotherm) is expected, the amount of sample admitted in the cell (about 20 mg) was optimized for a material with a typical figure of hundreds of m^2/g. This increases the error on the specific amount of adsorbed gas, which is normalized to the mass of the sample. With these considerations in mind, the analysis of those data with a BET or Langmuir model in order to extract a specific surface area measurement has to be considered meaningless and is not reported for this reason.

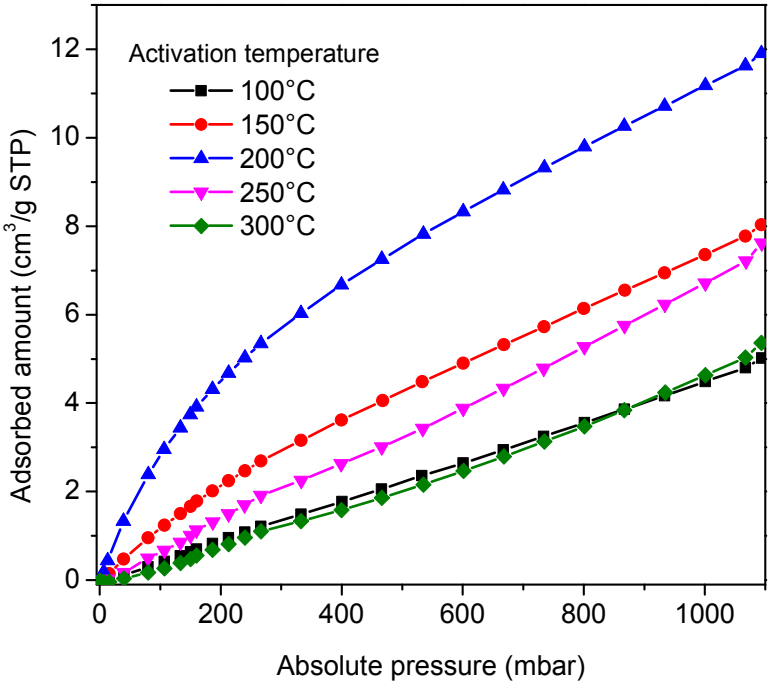

Figure 31 – 0°C CO_2 adsorption isotherms collected on $Ce_2(ADB)_3(DMA)_{3.4}$ after thermal activation at various temperatures. Desorption isotherms (still totally superimposable to adsorption ones) are omitted for the sake of clarity.

As an alternative method to characterize the porosity in this system CO_2 adsorption were measured in similar conditions to the nitrogen ones but at a temperature of 0°C. This time the isotherms are "well-behaving" as the material is capturing a not

negligible amount of gas: nevertheless this time the amount of sample used for the experiment was about ten times larger. The amount of carbon dioxide reaches a maximum at an activation temperature of 200°C then diminishes to go back at the one measured after the treatment at 100°C. The uptakes at a pressure of 1000 mbar are reported in the Table 13 below.

Table 13 – CO_2 uptakes of $Ce_2(ADB)_3(DMA)_{3.4}$. Isotherms measured at 0°C

Activation temperature	**CO_2 uptake (wt%) at 1000 mbar**
100°C	0.98
150°C	1.55
200°C	2.28
250°C	1.48
300°C	1.05

This material adsorbs a not negligible amount of CO_2 at 0°C. As these uptakes are not in the same order of magnitude of those measured on the best candidate for CO_2 storage and capture porous materials (i.e. UTSA-16[148] or Mg-MOF-74[109]) this material cannot be proposed for such applications. It must be considered that a kind of porosity, invisible for nitrogen, is present upon activation of $Ce_2(ADB)_3(DMA)_{3.4}$.

3.3 Ce/Zr-UiO-66

The synthesis of pure Zr, pure Ce and Ce-Zr mixed metal UiO-66 samples is described in section 2.1.3. The recipe for Ce containing samples is following what previously published by Lammert et al.[29,54,64]. For the synthesis of the pure Zr UiO-66, instead, the recipe published by Cavka et al.[22] was followed.

3.3.1 Crystal structure

The crystal structure of UiO-66, as thoroughly described in literature,[22,54,64,78,103,149] consists of a densely packed cubic face-centered lattice made from cuboctahedral $Zr_6O_4(OH)_4(CO_2)_{12}$ inorganic clusters connected by linear terephthalate linkers (see Figure 32). The carboxylates are bonding Zr^{4+} cations in a bidentate manner, above the edges of the hexanuclear octahedron. The three dimensional buildup of the structure forms a continuous face-centered cubic structure in which every cluster is linked to the 12 next neighbors.

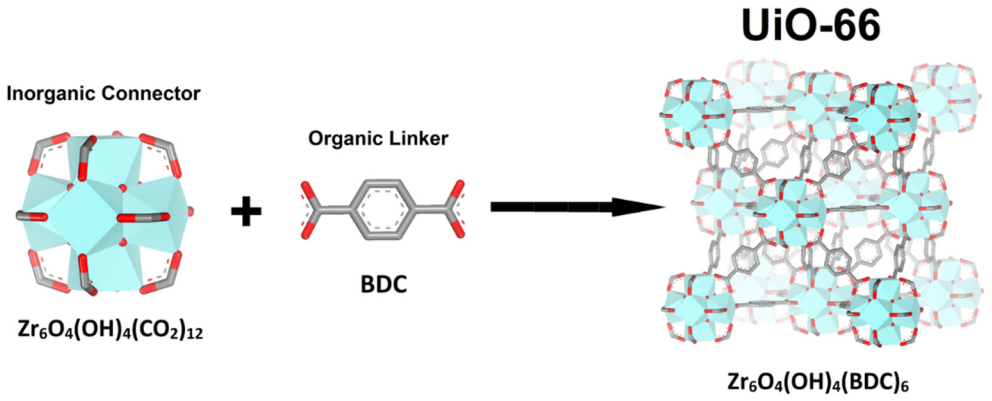

Figure 32 – Pictorial representation of the building of UiO-66: inorganic hexanuclear Zr_6 clusters and terephthalates assembling in a tightly packed cubic structure. Taken from ref. [78].

The pure Zr, pure Ce and the $Zr_{3.54}Ce_{2.46}$ samples were measured at the ID22 high-resolution powder diffraction beamline after being desolvated at 180°C in dynamic vacuum for 16 hours each. The results are shown in Figure 33, and results are summarized in Table 14.

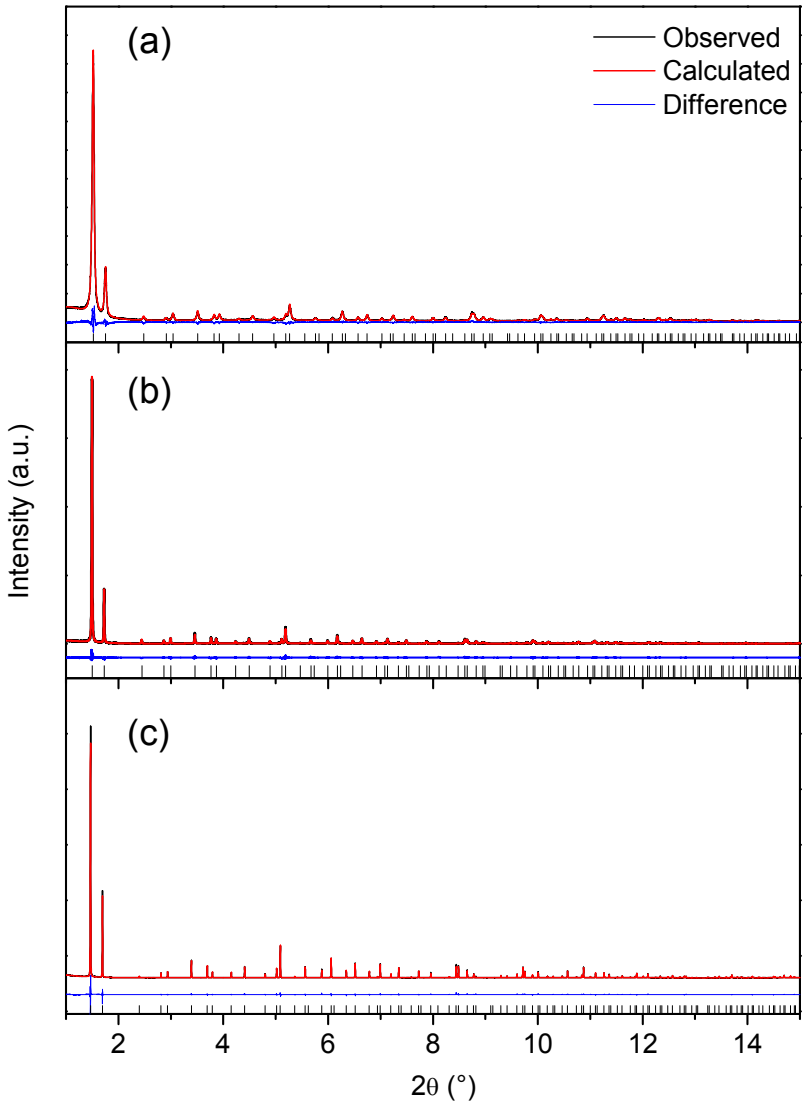

Figure 33 – PXRD pattern obtained on Zr UiO-66 (a), $Zr_{3.54}Ce_{2.46}$ UiO-66 (b) and Ce UiO-66 (c). The result for the Rietveld refinement is shown in red, and the residuals in blue. Vertical bars mark the allowed peak positions. ($\lambda = 0.31783$ Å).

Table 14 – Results and relevant information for the Rietveld refinement of the pure Ce, the pure Zr and one Ce/Zr-UiO-66 sample, the Ce45.

	Zr-UiO-66	**$Zr_{3.54}$-$Ce_{2.46}$ UiO-66 (Ce45)**	**Ce-UiO-66**
Formula	$12 \cdot [Zr_6O_6BDC_6]$	$12 \cdot [Zr_{3.54}Ce_{2.46}O_6BDC_6]$	$12 \cdot [Ce_6O_6BDC_6]$
Crystal system	$Cubic$	$Cubic$	$Cubic$
Space group	$Fm3m$	$Fm3m$	$Fm3m$
a (Å)	20.7535(2)	21.0652(1)	21.48825(2)
b (Å)	20.7535(2)	21.0652(1)	21.48825(2)
c (Å)	20.7535(2)	21.0652(1)	21.48825(2)
α = β = γ (°)	90	90	90
Cell volume (Å^3)	8938.75(26)	9347.52(14)	9922.09(2)
Temperature (K)	293(2)	293(2)	293(2)
R_{wp}	0.073	0.087	0.085
R_{Bragg}	0.027	0.03	0.024

All Rietveld refinements, performed up to 2θ = 32° (d_{min} = 0.577 Å), started from the published structure of Zr-UiO-66[22,103] and Ce-UiO-66[54] and proceeded without any issue. For the mixed metal sample the cations were refined independently of each other and their summed occupancy was fixed to one. As a general finding the cell parameter of the mixed-metal material seem to be linearly varying with the relative concentration of the metals. This behavior, already reported by Lammert et al. in 2017,[64] can be ascribed to the Vegard's law, which has been found to be working also for MOFs. As all Bragg peaks observed in the three samples belong to the UiO-66 phase no crystalline impurity could be detected. The peak width decreases with the amount of Ce: this indicates the progressive increase of crystallite size with the rise of Ce content.

As a general consideration from diffraction data, where only what is ordered can be observed[150], the fact that Ce and Zr are not forming any sort of superlattice or new crystal phase is a strong sign for the mutual disorder of Zr and Ce atoms in the lattice, even at the atomic level or at the cluster level This results in a diffraction data that cannot discriminate between these two metals inside the crystal cell.

The different width of the PXRD peaks from the three samples (Figure 33) is due to the different dimensions of the crystallites, as reported by Lammert et al.[64].

3.3.2 Thermal activation

For the thermal properties of pure Zr, pure Ce and mixed-metal UiO-66 material the present thesis refer totally to the works by Cavka et al.[22] for the Zr-UiO-66 and two papers from Lammert et al.[54,64] published in 2015 and 2017 for Ce-UiO-66 and the mixed-metal materials.

Remarkable thermal stability is one of the most important features of Zr-UiO-66: in fact this material shown to be still porous and crystalline up to 500°C in inert atmosphere. This has been shown by both TGA and VTXRD measurements.

Ce-UiO-66, on the other hand, showed a greatly reduced thermal stability when compared to the Zr counterpart losing totally its crystallinity at the temperature of 240°C, as shown by VTXRD measures.

The mixed-metal Ce/Zr-UiO-66 materials showed to have an intermediate behavior between the two pure compounds: as thoroughly shown by Lammert et al.[64] the thermal stability, determinated again by TGA and VTXRD measurements, showed to be greatly influenced by relative small amounts of Ce (Figure 34).

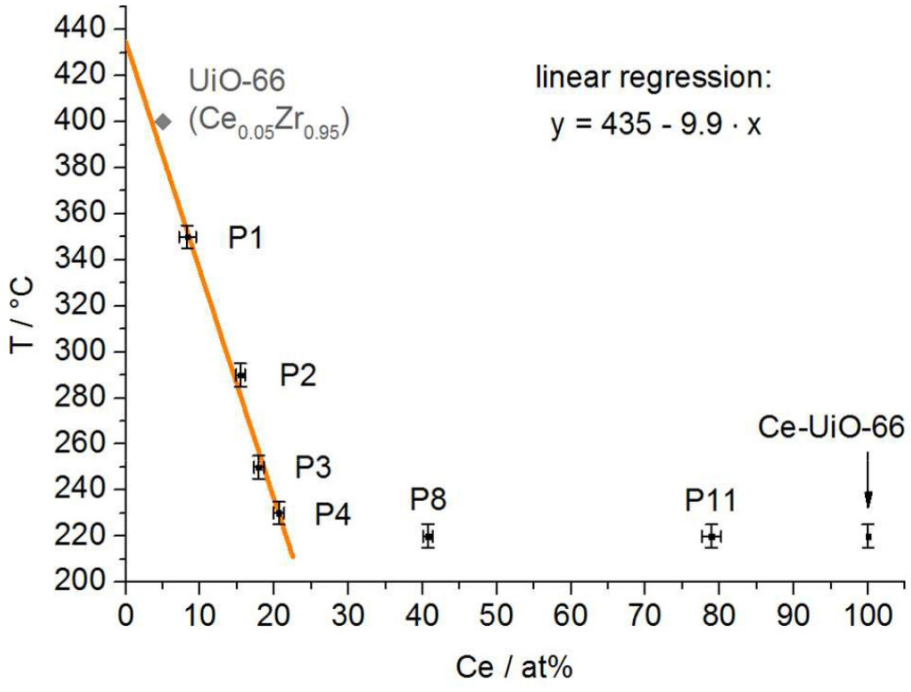

Figure 34 – Thermal stabilities of Ce/Zr-UiO-66 MOFs plotted against the amount of Ce. Taken from ref. [64].

As the samples studied in the paper by Lammert et al. are spanning the whole composition range from the pure Zr to the pure Ce materials, this data is perfectly compatible also with the samples studied in the present work.

3.3.3 X-ray absorption spectroscopy

As powder diffraction data gave no any new information about the spatial arrangement of Ce and Zr atoms the usage of XAS techniques (see section 1.3.2), being local techniques, shed light on this system.

XANES data collected on Ce L-edge, (Figure 35) demonstrate that Ce in all studied samples of MOFs is predominantly in the 4+ oxidation state. Zr is assumed to be also in the 4+ oxidation state, as already shown by Valenzano et al.[103].

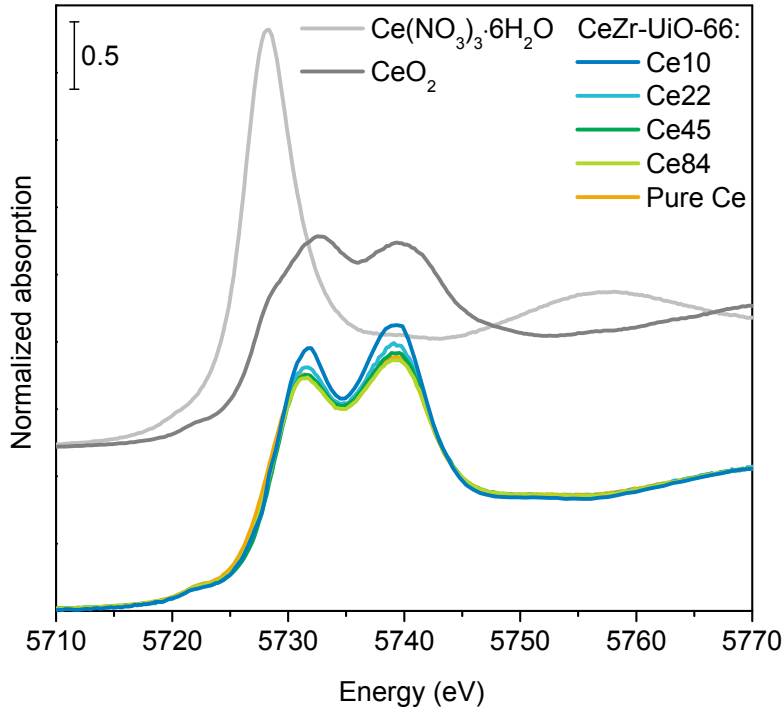

Figure 35 – Ce L_3-edge XANES spectra of bimetallic Ce/Zr-UiO-66 samples and pure Ce-UiO-66 compared to references for Ce(III) and Ce(IV) oxidation states.

XANES spectra of all Ce containing samples are very similar to each other, which confirms the similarity of the local geometry and electronic structure of both Ce and Zr cations also varying the Ce Zr ratio. This indicates that we are dealing with an isomorphous substitution of Ce in Zr sites (or vice-versa). These observations confirm the conclusions drawn from the PXRD Rietveld refinement.

The EXAFS region of the K-edges of both Ce and Zr is shown below in Figure 36.

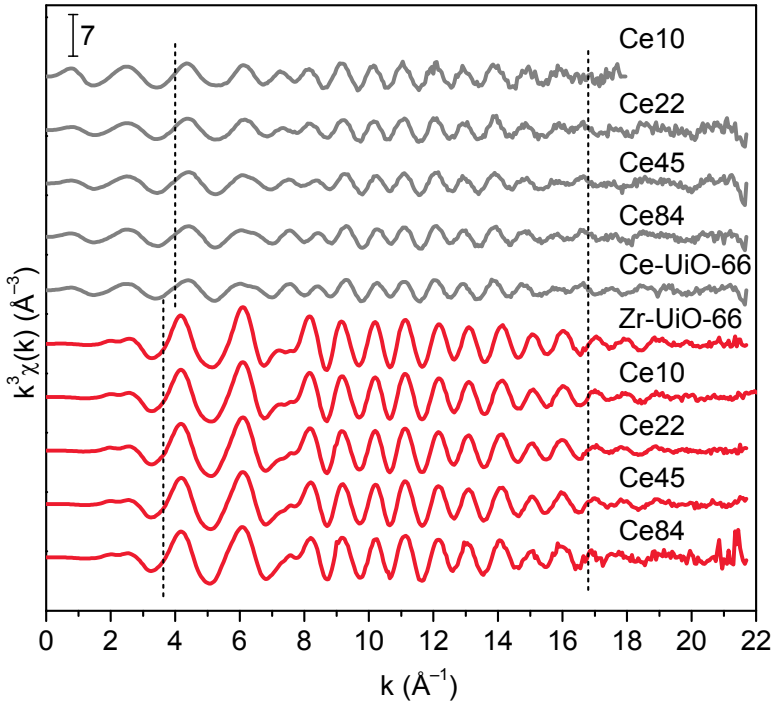

Figure 36 – EXAFS data at Ce (gray) and Zr K-edges (red) for all pure and bimetallic Ce/Zr-UiO-66 samples studied by XAS. Dashed lines indicate the regions used for the Fourier transform.

Fourier transformed Zr K-edge and Ce K-edge EXAFS data for five of the samples are shown in Figure 37 and Figure 38, respectively.

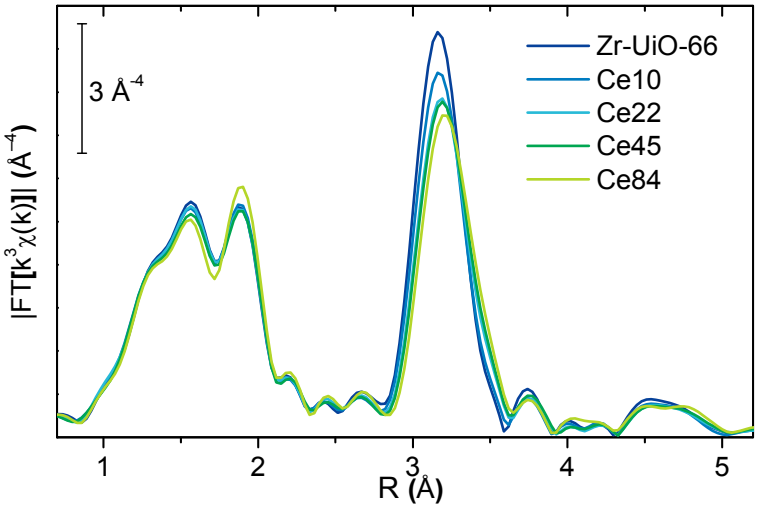

Figure 37 – Moduli of the phase-uncorrected Fourier transforms of k^3-weighted EXAFS data collected at the Zr K-edge for Ce/Zr-UiO-66 MOFs.

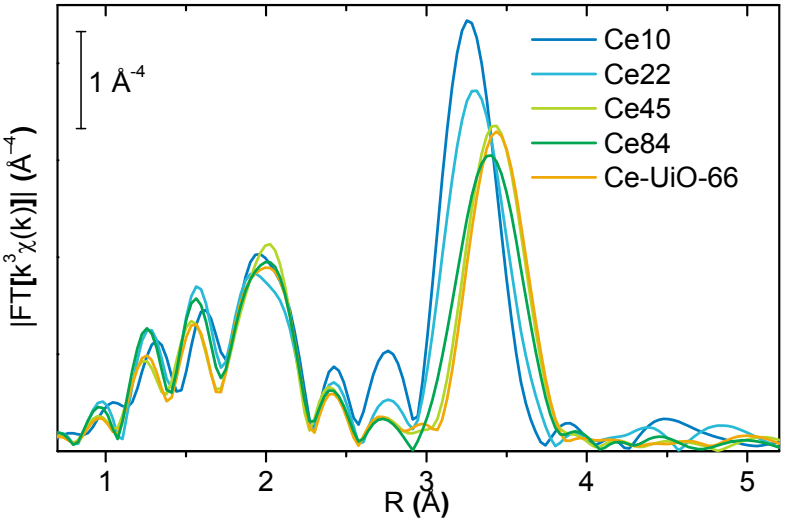

Figure 38 – Moduli of the phase-uncorrected Fourier transforms of k^3-weighted EXAFS data collected at the Ce K-edge for Ce/Zr-UiO-66 MOFs.

Qualitatively all the Fourier transformed spectra are in agreement with those already reported for UiO-66.[103] The shape of the peaks in the 1.2-2.5 Å, originating from the so-called first shell, and assignable to metal-oxygen scattering does not change in a significant way with the increase of Ce content: this evidences rather small variations in oxygen coordination of both Zr and Ce cations. The 2.8-3.8 Å peak, belonging to the second-shell of neighbors, is assigned to the metal-metal scattering from the members of the hexanuclear clusters present in the structure. The fact that the average value of the metal-metal distance depends on the ratio between the two metals confirms the formation of mixed-metal Ce_xZr_{6-x} cornerstones. It should be noticed that in this case, having a high-quality dataset (i.e. with a low signal to noise ratio), also the presence of a peak at 4.5-5 Å in the Zr edge data (Figure 37) can be observed. This signal is due to the scattering between the absorber atom and another one situated in the opposite vertex of the octahedron.

The changes that are taking place in the EXAFS spectra even upon addition of small amounts of Ce (Figure 38) can be explained hypothesizing the preferential formation of $CeZr_5$ clusters. This implies that only for Ce loadings lower than 17% one should have the contemporary presence of Zr_6 and $CeZr_5$ clusters. This is due to the simple consideration that there are six metallic cations per cluster and a material made only with $CeZr_5$ clusters would have a 17% Ce loading. In the case that any number of Zr atoms in a pristine Ce_6 cluster should be the same of a number of Ce atoms in a Zr_6 cluster the Zr and Ce EXAFS spectra should be looking pretty similar. As this is not the case (Ce additions to Zr-UiO-66 are not causing the same effect as Zr additions to Ce-UiO-66) some preferential cluster composition should be hypothesized. By similar considerations, the presence of hexanuclear Ce_6 clusters should be considered when dealing with samples with a Ce content higher than 17%, as the differences between Zr K-edge spectra of Ce22, Ce45 and Ce84 samples are minor. A detailed description about also the fitting of the EXAFS curves can be found in the paper in Appendix I.

The preferential formation of $CeZr_5$ cornerstones is also explaining the trend in the thermal stability already observed by Lammert et al.[64] (Figure 34): in fact, once the Ce concentration has reached around 20% the thermal stability of the bimetallic MOF is constant and it is the same value observed for Ce-UiO-66. This is consistent with the hypothesis for which above the Ce concentration of 20% there is the formation of hexanuclear Ce_6 clusters, whose thermal stability is indeed the one of Ce-UiO-66.

3.3.4 Vibrational spectroscopy

With the aim to characterize only mixed metal Ce/Zr-UiO-66 samples having $CeZr_5$ clusters and Zr_6 clusters, a series of low-containing samples (<17%, under the hypothesis advanced in the last chapter) was synthesized and characterized by dosing a probe molecule in an *in-situ* FTIR experiment. Aiming to probe the Lewis acidic sites present inside the pores CD_3CN was dosed after a prolonged thermal activation in dynamic vacuum at the temperature of 160°C. The activation conditions were optimized in order to get rid of almost all the solvent present in the pores of the material without collapsing it. The spectra of Ce5, Ce10 and Ce15 samples after thermal activation and after dosing the vapor pressure of CD_3CN are shown in Figure 39 below.

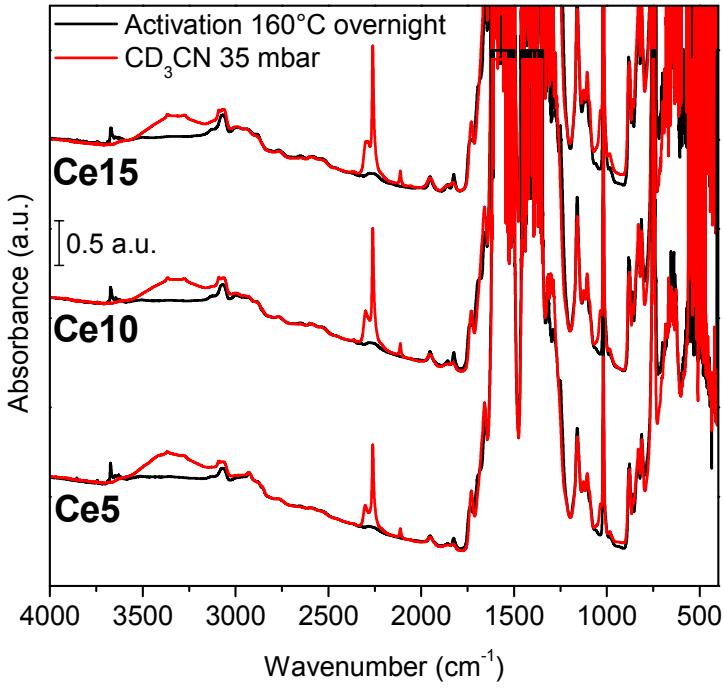

Figure 39 – FTIR transmission spectra of Ce5, Ce10 and Ce15 Ce/Zr mixed-metal UiO-66 samples after activation at 160°C (black). Spectra after dosing CD_3CN are reported in red.

All the spectra from the three samples are quite similar and the bands typical of MOFs are quite visible: the carboxylate symmetric and asymmetric stretching in the 1700-1250 cm^{-1} are evident. A complete assignation of all the vibrational bands, aided by computational simulations of the vibrational modes, can be found in the paper by Valenzano et al.[103]. Upon interaction with deuterated acetonitrile vapors, the sharp signal from OHs at 3670 cm^{-1} shifts into a broad band centered at 3300 cm^{-1} because of hydrogen bond formation. At the same time a sharp signal coming from the stretching of the C≡N bond is visible in the region around 2275 cm^{-1}. A magnified look at this spectral region for the Ce15 sample is reported in Figure 41 below, while the data collected on all three samples are reported in Figure 41.

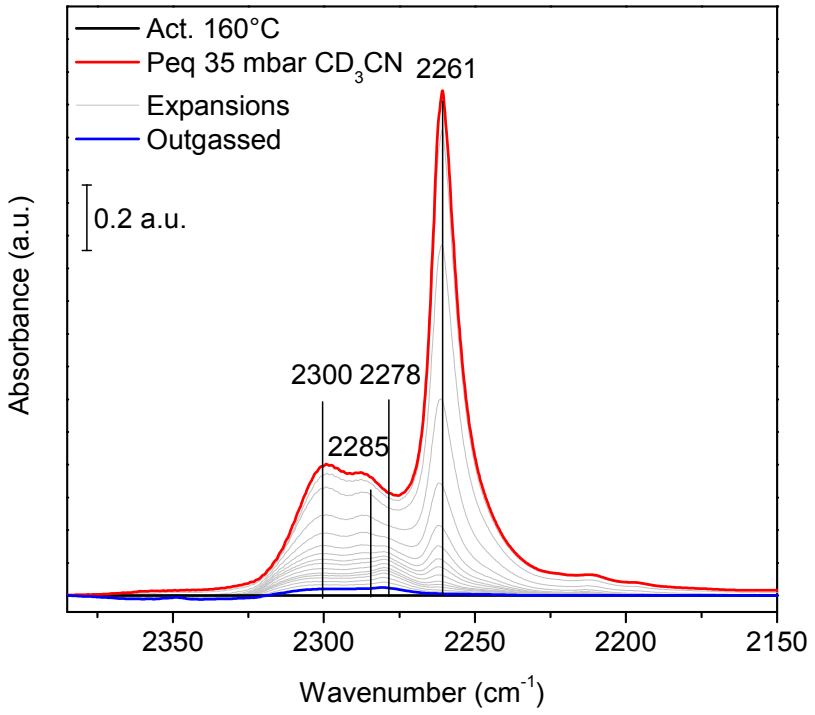

Figure 40 – Background subtracted FTIR spectra of the C≡N stretching region collected on Ce15 Ce/Zr-UiO-66 sample. Maximum coverage is reported in red, progressive outgassing in grey and prolonged outgassing in blue.

The C≡N stretching region is characterized by four bands in all three samples, assignabile in the following way:

- 2261 cm^{-1}: Liquid-like CD_3CN, characteristic of porous systems.[151]
- 2278 cm^{-1}: CD_3CN interacting with OHs from the cornerstones: the growth of this band is correlated with the one at 3300 cm^{-1} (Figure 39) that is restored upon outgassing
- 2285 cm^{-1}: CD_3CN interacting with Ce^{4+} Lewis acidic sites[152]
- 2300 cm^{-1}: CD_3CN interacting with Zr^{4+} Lewis acidic sites as reported by Nouar et al.[153]

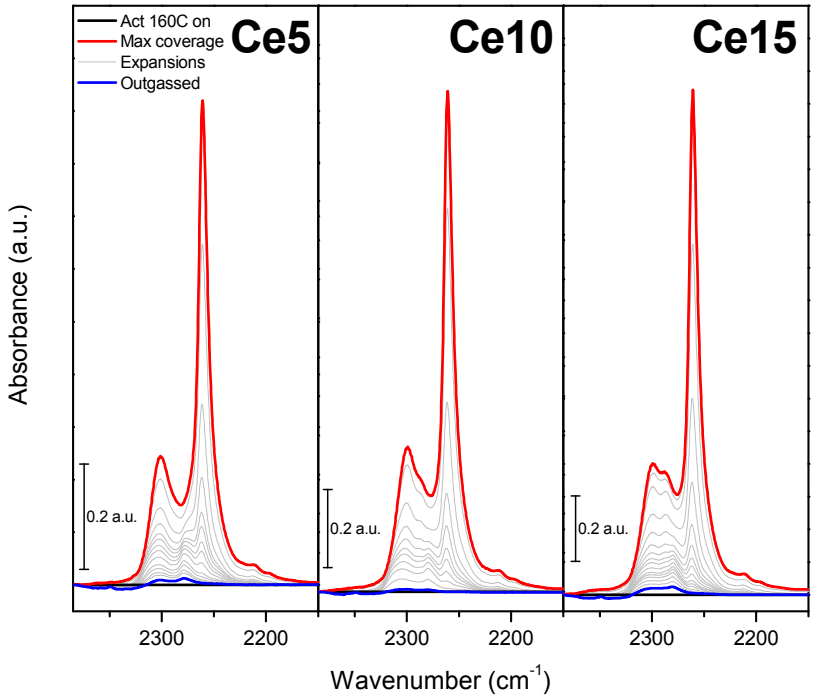

Figure 41 – Background subtracted FTIR spectra of the C≡N stretching region collected on Ce5, Ce10 and Ce15 Ce/Zr-UiO-66 samples. Maximum coverage is reported in red, progressive outgassing in grey and prolonged outgassing in blue.

The shape and the relative intensity of those bands is related to the Ce/Zr ratio (Figure 41): the higher the Ce content, stronger the band related to CD_3CN interacting with Ce sites.

3.4 Ce-UiO-66-ADC

The synthesis procedure of Ce-UiO-66-ADC described in section 2.1.4 was optimized by the means of high-throughput methods, also described earlier in the introduction in section 1.2.1. A SEM image of the product is printed in Figure 42. Only aggregates are visible as the crystal size is too small for being observed by SEM.

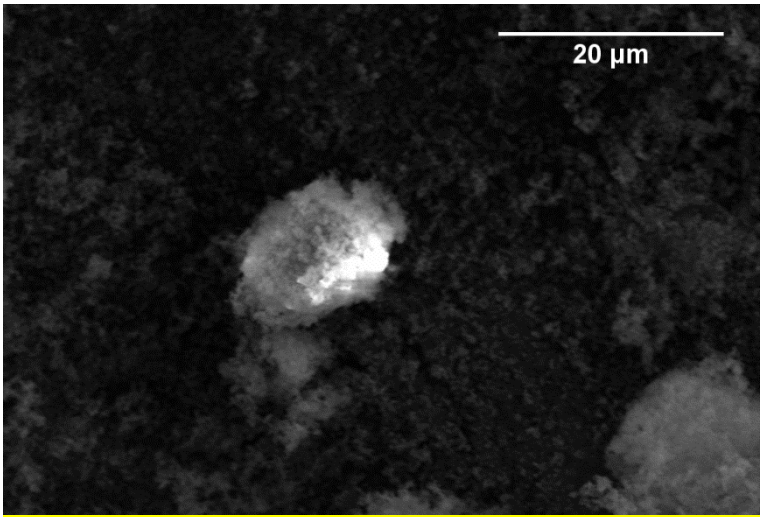

Figure 42 – SEM image of Ce-UiO-66-ADC.

3.4.1 Crystal structure

As in this case the synthesized product presents crystallites in the sub-micrometer dimension range the application of a single-crystal x-ray diffraction method to solve the structure was impossible as a crystal of suitable dimensions (>200 µm) is needed. To overcome this, a structural refinement on the powder x-ray diffraction pattern was done in order to obtain a suitable crystal structure for the material using the Rietveld method[150] (Figure 43). As a starting point for the refinement a structural model for Ce-UiO-66-ADC was built in Materials Studio (Figure 44) starting from the structure of UiO-66[22,103], substituting the terephthalate moieties with acetylenedicarboxylates and optimizing geometrically the structure using the Forcite program module.

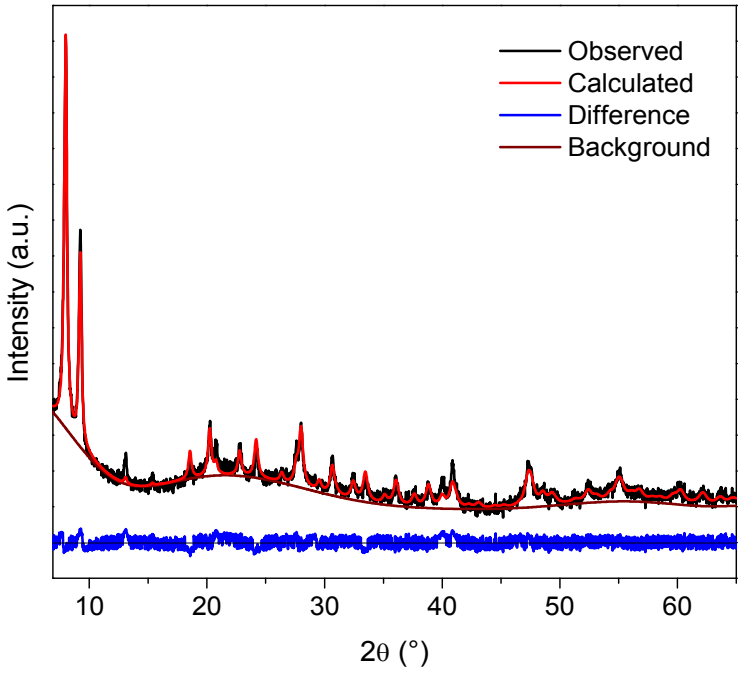

Figure 43 – PXRD pattern obtained on Ce-UiO-66-ADC (black curve). The result for the Rietveld refinement is shown in red, and the residuals in blue. (λ = 1.5406 Å)

Position of Ce atoms was refined freely while acetylenedicarboxylates were treated as rigid bodies in order to increase the stability of the fit and reduce the number of parameters refined. The refined parameters along with relevant crystallographic data are reported in Table 15 below.

It is relevant to notice that even the refinement was done on a dehydroxylated structure, as the presence of OH groups is very difficult to be observed by x-ray diffraction techniques. The presence of OH groups in the structure of UiO-66 is a well-known fact in literature[103] and for this reason their presence can be also hypothesized here. For this reason, the proposed structure would be $[Ce_6O_4(OH)_4(ADC)_6]$ while the refined one is slightly different.

Table 15 – Results and relevant information for the Rietveld refinement of Ce-UiO-66-ADC.

	Ce-UiO-66-ADC
Formula	$12 \cdot [Ce_6O_6ADC_6]$
Formula weight (g·mol^{-1})	6563.73
Crystal system	*Cubic*
Space group	$Fm3m$
a (Å)	19.1101(2)
b (Å)	19.1101(2)
c (Å)	19.1101(2)
α = β = γ (°)	90
Cell volume (Å^3)	6979.9(2)
Temperature (K)	293(2)
Abs. coefficient (cm^{-1})	300.58
Calc. density (g·cm^{-3})	1.559
Z	1
Measured reflections	24
No. of structural parameters	14
R_{wp}	0.097
R_{Bragg}	0.074

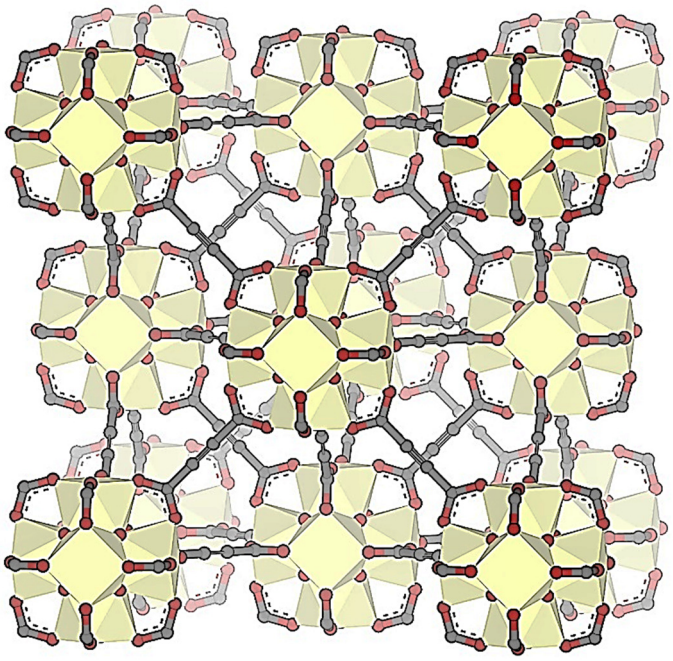

Figure 44 – Pictorial representation of the crystal structure of Ce-UiO-66-ADC. Cerium, oxygen and carbon atoms are printed respectively in yellow, red and black.

The crystal structure of Ce-UiO-66-ADC is characterized by the presence of hexanuclear Ce clusters (that can be considered as SBU) connected 12-fold with the neighboring ones to form a tightly packed face-centered cubic structure. This makes the material perfectly isostructural with the one of the pristine UiO-66[22,103] making this material an example of reticular chemistry, as described by Yaghi et al.[19]. Being acetylenedicarboxylates shorter than their terephthalate counterparts, the cell parameter is indeed smaller than UiO-66, nevertheless it has to be noticed that Ce-based MOFs have cell parameters slightly larger than their Zr materials made with the same linker, as shown by Lammert et al.[54,64].

3.4.2 Thermal activation

The behavior of Ce-UiO-66-ADC upon thermal treatment was studied by the means of TGA (Figure 45) and VTXRD (Figure 46) techniques giving results shown below.

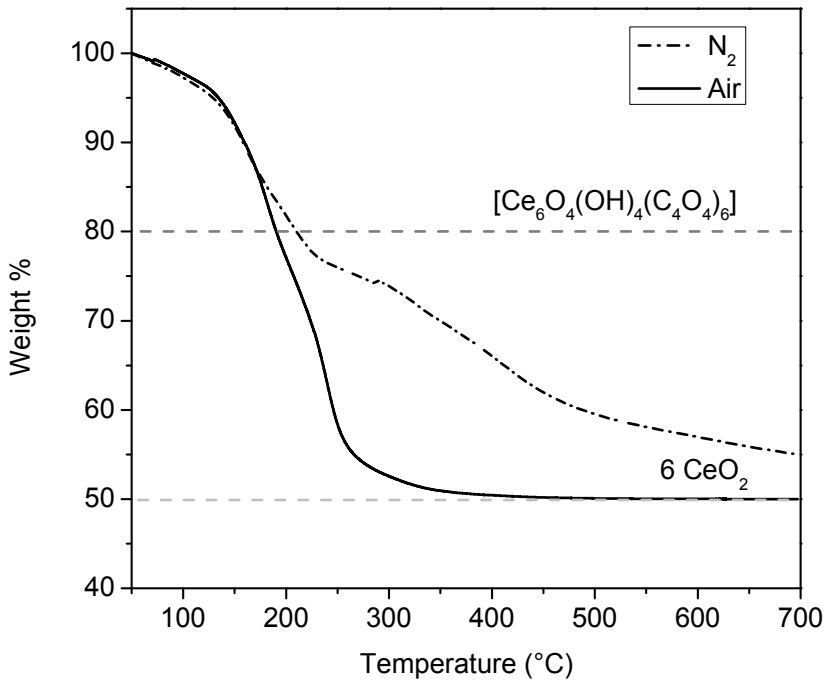

Figure 45 – TGA data collected on Ce-UiO-66-ADC in dry air (solid curve) and nitrogen (dashed curve) atmospheres.

The TGA curves show a very steep weight loss starting below 100°C in both atmospheres. They begin to diverge at about 200°C indicating that oxygen is playing a role in the weight loss of the materials and an oxidative process can be inferred from this data as the "classical" combustion of the organic moieties is expected to happen at higher temperatures (about 400°C). Considering the final mass of the sample after total combustion in air to be merely cerium dioxide one can use the formula unit of the crystal structure to calculate what would be the mass of sample that has to react to have this amount of oxide. This calculation is represented by the dashed horizontal grey lines in Figure 45. The residual 20% of the mass can be attributed to solvent (DMF or water) adsorbed within the pores of the material.

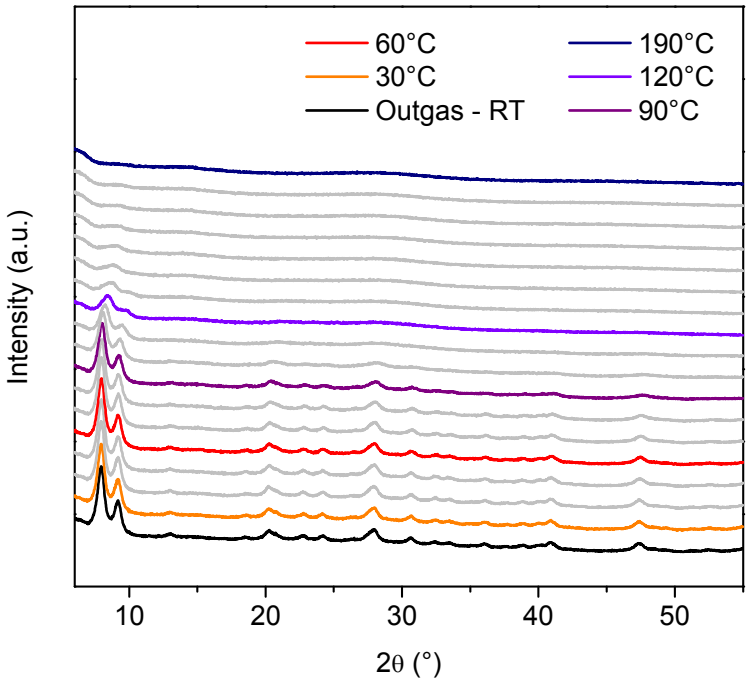

Figure 46 – VTXRD data collected on Ce-UiO-66-ADC in dynamic vacuum conditions. (λ = 1.5406 Å). Some relevant temperatures are highlighted for the sake of clearness.

As it is evident from the VTXRD data Ce-UiO-66-ADC retains its crystal structure upon heating in dynamic vacuum only up to 90°C. Above this temperature the main PXRD reflexes positioned above 10° in 2θ are vanishing totally together with all other signals. An extremely broad signal around 28° can be assigned to the formation of extremely small CeO_2 nanocrystals.

Comparing TGA with VTXRD (even considering that TGA data was collected in nitrogen flow, while the diffraction was carried out in dynamic vacuum for technical limitations) it is evident that the solvent cannot be outgassed during a thermal treatment keeping the MOF crystalline, as the amorphization temperature is much lower than the onset temperature of the first weight loss of the TGA curve, assigned to the desorption of solvent from the pore system of the material.

3.4.3 Adsorption properties

In order to highlight porosity and specific surface area of Ce-UiO-66-ADC, N_2 adsorption isotherms at -196°C were measured after thermal treatments in dynamic vacuum at increasing temperatures giving isotherms shown in Figure 47.

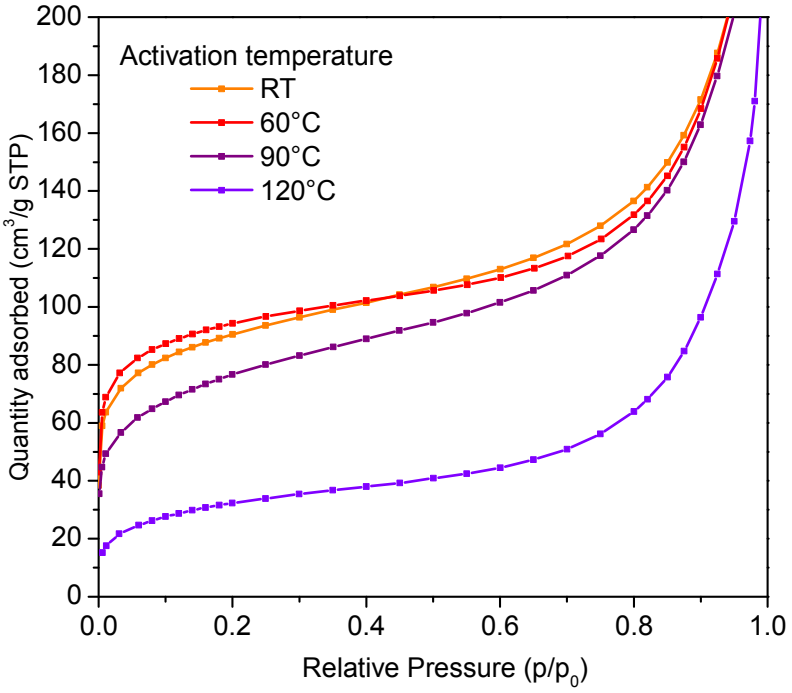

Figure 47 – -196°C N_2 adsorption isotherms collected on Ce-UiO-66-ADC. Activation temperature is highlighted by the color of the curve: RT (orange), 60°C (red), 90°C (purple) and 120°C (violet). Desorption branches (superimposable to adsorption branches) are omitted for the sake of clarity.

The activation temperatures for the thermal activation procedure were chosen looking at the results of the VTXRD experiment (Figure 46) in order to observe a correlation between uptake (and thus, porosity and surface area) with structural changes due to heating. All isotherms belong to the Type I classification according to IUPAC guidelines[100] as typical of microporous materials and expected for a UiO-66 isostructural material[22].

The analysis of the N_2 adsorption isotherms reported in Figure 47 with both Langmuir and BET models for the calculation of the specific surface area leads to values reported in Table 16 below. All activation procedures were 3 h long.

Table 16 – Specific surface area values measured on Ce-UiO-66-ADC.

Activation temperature	Langmuir area (m^2/g)	BET area (m^2/g)
RT	425(5)	316(3)
60°C	437(4)	327(4)
90°C	371(6)	273(2)
120°C	163(3)	118(1)

Despite the small weight loss observed in TGA in this temperature range (RT-120°C) the material is showing a remarkable specific surface area (up to about 430 m^2/g after activation at 60°C). Those values decrease at higher activation temperatures as suggested by VTXRD data which is pointing out a collapse of the crystal structure at temperatures above 90°C.

It is relevant to notice that a geometrical calculation made with the Materials Studio code of the specific surface area, made from the crystal structure found by Rietveld refinement, indicates a value of about 1200 m^2/g. The discrepancy between the simulated and the experimental values can be explained by the presence of adsorbed solvent (DMF or water) inside the pores of the material at those activation temperatures, as shown by TGA data (Figure 45). With those experimental result it is reasonable to consider that DMF cannot be desorbed by dynamic outgassing during heating because the material itself is collapsing before. Regular UiO-66, instead, being stable up to 500°C can be desolvated by this method without losing crystallinity[22,103,154].

3.4.4 Vibrational spectroscopy

Vibrational spectroscopies (FTIR and Raman) were employed to characterize Ce-UiO-66-ADC in order to obtain information about the chemical nature of the material. Those spectroscopies were also used to follow in an *ex-situ* manner the thermal activation procedure made before the nitrogen adsorption isotherms and the VTXRD experiments. Results are shown below in Figure 48 and Figure 49, respectively.

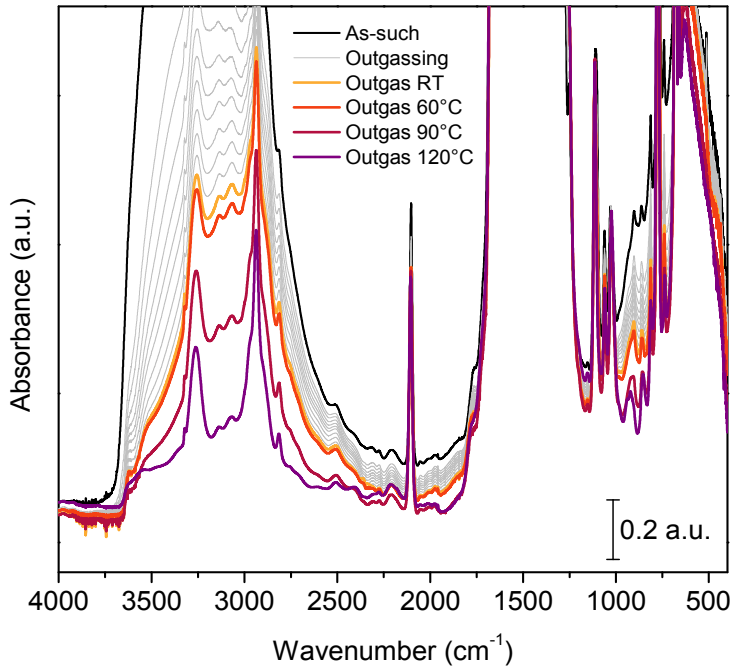

Figure 48 – Transmission FTIR spectra collected on Ce-UiO-66-ADC as such (black), after an overnight outgassing (orange) and thermal activations in dynamic vacuum (3 h long) at 60°C (red) 90°C (purple) and 120°C (violet).

The high-wavenumber region of the FTIR spectra is dominated by a very intense broad band in the 3400-2800 cm^{-1} range that can be assigned to OH groups of adsorbed solvent molecules (DMF and water, supposedly) interacting via H-bonds mutually within the pores of the MOF. This band is weakening but not vanishing after an overnight outgassing at room temperature (orange curve).

An assignment[143] of some relevant vibrational bands of the spectra reported in Figure 48 is the following:

- 3260 cm^{-1} ν(CH) of terminal alkyne
- 2935 cm^{-1} $\nu(CH)_{sym}$ of aliphatic CH groups from DMF
- 2810 cm^{-1} $\nu(CH)_{asym}$ of aliphatic CH groups from DMF
- 2107 cm^{-1} ν(C≡C) of asymmetrically substituted alkyne
- 1770 cm^{-1} ν(C=O) (shoulder) of carbonyl from DMF
- 1690-1280 cm^{-1} $\nu(COO^-)$ symmetric and asymmetric stretching of carboxylates

The region under 1000 cm^{-1}, the fingerprint region, is full of bands due to both linker moieties and Ce-O vibrational modes For a complete assignation of the bands in this region a computational modelling is mandatory as successfully applied in similar cases[83,103].

The effect of thermal treatment at increasingly higher temperatures (up to 120°C, violet curve in Figure 48) is causing the progressive decrease of the intensity of the broad band centered at 3100 cm^{-1} as the solvent adsorbed in the pores is being outgassed. As demonstrated by VTXRD and N_2 adsorption measurements at temperatures above 90°C the material collapses losing its crystallinity and porosity: this spectroscopic data demonstrate that it's not possible to outgas totally the MOF from the adsorbed solvents without collapsing it. It is however interesting to notice that the collapse is not testified by the comparison of the vanishing of a vibrational band, testifying a substantial chemical similarity between the crystalline pristine product and the collapsed one after treatment at temperatures above 90°C. The faint shoulder observable at 3620 cm^{-1} can be tentatively assigned to the presence of dangling OH groups from the Ce_6 clusters, as thoroughly known for UiO-66[103] but still engaged in H-bond interaction with solvent molecules adsorbed in the pores.

The color of the pellet during the thermal treatments changes from the pale yellow of the as-synthesized compound to a dark yellow at 90°C and a brown color at 120°C indicating the comparison of visible light absorbing species during the heat treatment.

The bands at 3260 and 2107 cm^{-1} characteristic of terminal alkynes are extremely informative and unexpected, as the linker used is, in fact a symmetrical substituted alkyne and the stretching of the triple bond is not active in IR spectroscopy[143]. Their intensity, however, it is not changing during outgassing and thermal treatments. Being the stretching of symmetric triple bonds a vibrational mode active in Raman spectroscopy the study continued with the measurement of such a spectra.

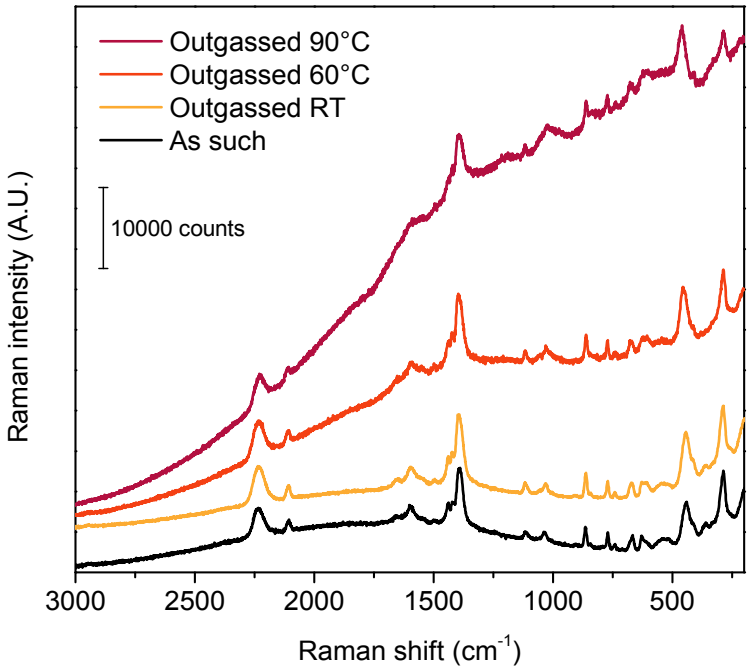

Figure 49 – Raman spectra collected on Ce-UiO-66-ADC as-such (black) after an overnight outgassing (orange) and after thermal activations in dynamic vacuum (3 h long) at 60°C (red) and 90°C (purple). (λ_i = 785 nm). The 120°C curve is omitted for too high fluorescence.

The same *ex-situ* experiment done by means of FTIR spectroscopy was replicated in the case of Raman technique (Figure 49). A general trend that can be correlated with increasingly high activation temperatures is the growing of the baseline due to concomitant fluorescence. The principal and most informative Raman bands were assigned[143] as the following:

- 2234 cm^{-1} — $\nu(C\equiv C)$ of symmetrically substituted alkynes
- 2107 cm^{-1} — $\nu(C\equiv C)$ of asymmetrically substituted alkynes
- 1584 cm^{-1} — $\nu(C=O)$ of carbonyl from DMF
- 1475-1350 cm^{-1} — $\nu(COO^-)_{sym}$ of carboxylates

The contemporary presence of symmetrically and unsymmetrically substituted alkynes can be inferred by the presence of both vibrational bands in the Raman spectra.

To undoubtedly assign those unexpected vibrational bands typical of triple bonds the vibrational spectra of Ce-UiO-66-ADC was compared with the spectra of acetylenedicarboxylate and propiolate anions, as in Figure 51, (the common name for the propynoate anion) in water solution as prepared from commercial starting materials. The standard solutions were prepared titrating with an excess of aqueous 5M KOH solution a suitable amount of commercial acetylenedicarboxylic acid (the linker used in the MOF synthesis) and propiolic acid.

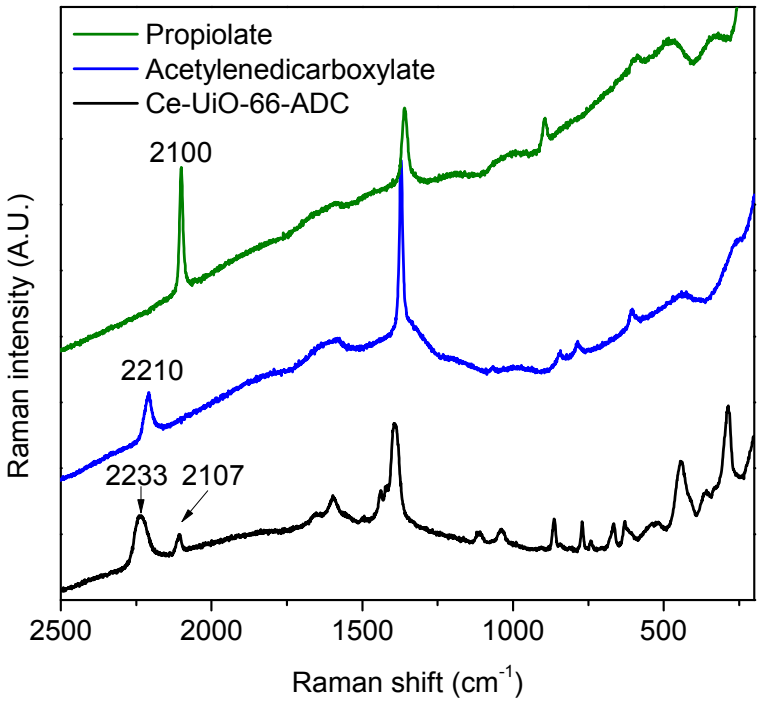

Figure 50 – Comparison of the Raman spectra of Ce-UiO-66-ADC (black) with basic water solutions of acetylenedicarboxylate (blue) and propiolate (green). (λ_i = 785 nm).

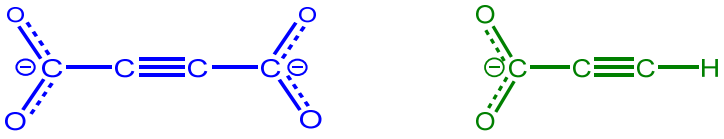

Figure 51 – Acetylenedicarboxylate (blue) and propiolate (green) anions.

3.4.5 Linker decarboxylation

As prompted out by the unexpected and serendipitous presence of vibrational bands typical of terminal alkynes they must be synthesized during the synthesis of the MOF, which is done solvothermally in water/DMF mixture at 100°C. No any relevant impurity of propiolic acid in the commercial acetylenedicarboxylic acid is highlighted by Raman spectroscopy. As previously reported by Tranchemontagne et al.[155] H_2ADC is thermally sensitive and it decomposes during synthesis if this is done at a sufficiently high temperature.

Li et al. reported in 2002[156] a detailed study about the kinetics of the decarboxylation reaction of acetylenedicarboxylic acid in water medium in function of the temperature (Figure 52).

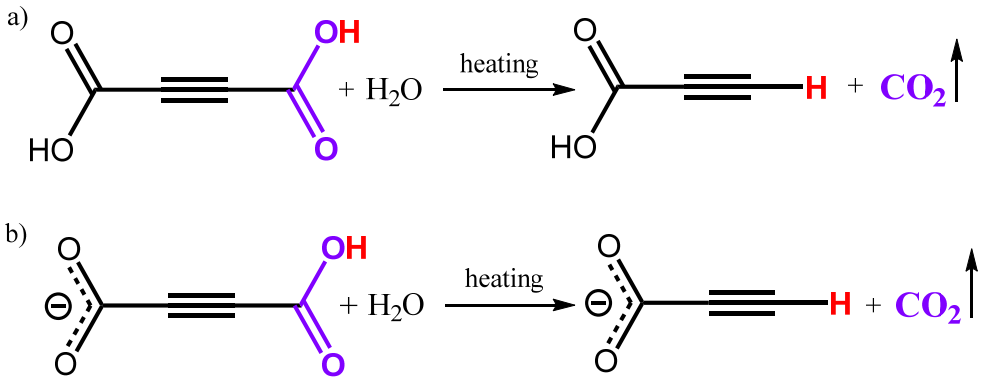

Figure 52 – Water-mediated decarboxylation reaction of H_2ADC (a) and $HADC^-$ (b).

What emerges from the paper is that the speed of this reaction is strongly dependent from the starting species i.e. the mono and the double deprotonated $HADC^-$ and ADC^{2-} as reported below in Figure 53.

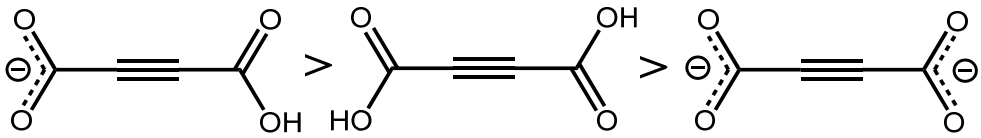

Figure 53 – Order of the decarboxylation speed for acetylenedicarboxylate related conjugated acids and bases.

This is also reasoning the finding for which the yield of the synthesis reaction for Ce-UiO-66-ADC is greatly improved if triethylamine is added to the synthesis mixture, as noticed during the optimization of the synthesis procedure of this compound[132].

The addition of a base pushes the equilibrium towards the double deprotonated species, which is more resistant to decarboxylation.

3.4.6 Defectivity hypothesis

The presence of defects in the crystal structure of UiO-66 is well-known in literature[157–159]. They can be related to both inorganic and organic components and, in the case of UiO-66, two main point defects types were characterized: missing cluster and missing linker defects. The first one corresponding to the absence of a hexanuclear metal cluster and the latter related to the lack of a linker molecule bridging two different SBUs. Both defects require some compensing anions in order to achieve the electrical neutrality: frequently they have been identified as monocarboxylate moieties (e.g. formate, acetate). The deliberate addition of monocarboxylic acids in the synthesis mixture of UiO-66 permitted to modulate the presence and concentration of defects in such material doing an effective "defect-engineering"[81,83,94,160]. Defectivity in UiO-66 is testified by the following experimental evidences, as reported by Shearer et al.[157]: reduced thermal stability, the occurrence of forbidden PXRD reflections, stoichiometric incongruencies from TGA data and deviations from the theoretical surface area. As reported in the paper[83] reported in Appendix II if the monocarboxylic moieties have a definite vibrational fingerprint, i.e. benzoate anions, the presence of defects can be correlated also with the appearance of unexpected vibrational bands.

In the case of Ce-UiO-66-ADC the *in-situ* production of the monocarboxylic derivative of the linker propiolic acid through a decarboxylation reaction was demonstrated by vibrational spectroscopy. For this reason the presence of defects decorated by propiolate moieties can be hypothesized looking at the current multi-technique dataset. Such proposed defective structure is visualized in Figure 54.

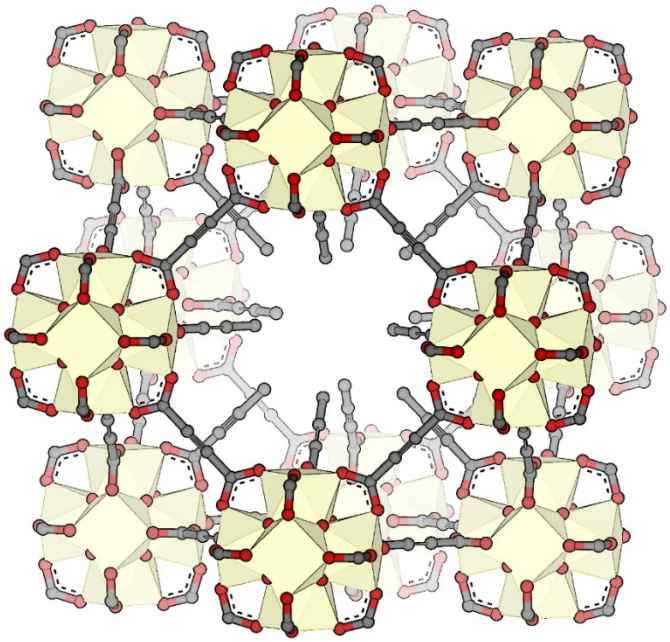

Figure 54 – Hypothesized missing-cluster defect decorated by propiolates for Ce-UiO-66-ADC.

As the current dataset does not permit to recognize unambiguously the presence of this defect into Ce-UiO-66-ADC such sentence is not anything more than a hypothesis. New experimental data as dissolution ^{1}H and ^{13}C NMR quantitative spectroscopy is needed in order to strengthen this hypothesis.

4.Conclusions

This thesis presented the successful synthesis of four novel Ce-based MOFs and their characterization with a selection of techniques specifically selected to disclose the properties of each material. The following paragraphs will concern singular conclusions that can be drawn from each material.

$Ce_2(NDC)_3(DMF)_2$

A novel MOF based on Ce^{3+} cations and a simple ditopic linker (2,6-naphthalenedicarboxylic acid) was synthesized with a solvothermal method. Its crystal structure solved by the means of a SCXRD technique, revealed its simple and rather unique structure formed by infinite Ce chains forming diamond-shaped channels. This material upon thermal treatment loses its crystallization DMF molecules and transforms into a different phase characterized by a high amount of crystalline disorder, as demonstrated by TGA and VTXRD data. The crystal structure of the desolvated MOF was solved from a synergic use of both SCXRD and EXAFS techniques that revealed a disordered structure with triangular channels. Despite the absence of a surface area by the means of N_2 volumetry at -196°C the material showed a decent porosity by CO_2 at -78°C evidencing a kind of porosity traditionally overlooked by classical characterization methods.

As this material is selectively adsorbing CO_2 over N_2, applications in separation of CO_2/N_2 mixtures can be proposed exploiting this characteristic of $Ce_2(NDC)_3$.

$Ce_2(ADB)_3(DMA)_{3.4}$

In a tight comparison with the above mentioned material, another novel Ce^{3+}-based material has been synthesized with solvothermal methods. The optimization of the synthesis procedure, with the help of the so-called High-Throughput methods, permitted to find the optimal conditions: the usage of DMA instead of DMF revealed to be necessary for the success of the synthesis. The material revealed a series of phase transitions upon heating accompanied by the loss of the crystallization solvent. These crystalline phases are characterized by a high degree of inherent disorder that prevented their solution by single-crystal x-ray diffraction. The study of the porosity of these compounds and their crystal structures may be completed by exploiting the same techniques that revealed to be useful in the study of $Ce_2(NDC)_3(DMF)_2$: synchrotron-based techniques (i.e. EXAFS spectroscopy) and CO_2 volumetry at -78°C.

Being the linker used in the building of the $Ce_2(ADB)_3(DMA)_{3.4}$ able to absorb visible light (i.e. colored) a possible application for this material may be inside optical devices as a light harvester.

Ce/Zr-UiO-66

Mixed metal Ce/Zr-UiO-66 was recently introduced in the literature as a way to improve the reactivity of UiO-66 using a redox-active metal like cerium. The resulting material revealed a diminished thermal stability than its pure Zr counterpart even at low Ce contents. In order to highlight the composition of the metal clusters, synchrotron high-resolution powder diffraction and the *in-situ* dosage of CD_3CN as a probe molecule in FTIR spectroscopy experiments were employed: the results highlighted the presence of Ce cations inside the material but without a specific information about the composition of the clusters. Thanks to a multi-wavelength EXAFS analysis on both Zr and Ce K-edges, the composition of the metallic cornerstones was finally identified to be truly bimetallic. The same technique highlighted also the preferential formation of $CeZr_5$ hexanuclear clusters instead of any other type of stoichiometry. By a result of this, a Ce/Zr-UiO-66 material would have a mixture of Zr_6 and $CeZr_5$ clusters at Ce loadings lower than 17% (1/6 of the total atomic metallic content) and a mixture of $CeZr_5$ and Ce_6 clusters at higher concentrations. This result explains also the relationship between the Ce content and the thermal stability already observed by Lammert et al.[64]

In respect to their Zr counterparts Ce-based UiO-type materials are suffering a general decreasing of the thermal and chemical stability. As Ce is known to be a redox-active metal (its oxide, CeO_2, is widely exploited as redox catalyst) Ce/Zr mixed UiO-66 MOFs may bridge the gap between the thermally delicate Ce-UiO-66 and the redox-inactive Zr-UiO-66 and they can be exploited as redox catalysts.

Ce-UiO-66-ADC

Since the discovery of UiO-66 a number of works by the scientific community was devoted to this material: iso-reticular material with ditopic linkers, defect engineering, post-synthetic modifications, just to cite few of these. None of these papers is devoted to the insertion of acetylenedicarboxylate as linker in UiO-66, probably because of its extreme thermoliability, thus its non-decomposition being difficult during the synthetic conditions of UiO-66. This thesis presented the first successful synthesis of an acetylenedicarboxylate-containing UiO-66 derivative with Ce^{4+} cations. The crystalline structure of this compound was determined via a Rietveld refinement which resulted in an isostructurality with UiO-66. This MOF revealed a poor thermal stability collapsing totally already at 90°C but even at after a

thermal activation at lower temperature it showed a decent porosity by the means of N_2 adsorption measurement at -196°C in the order of 400 m^2/g. Vibrational spectroscopies, IR and Raman, showed serendipitously the presence of a band assignable to the presence of propiolates, coming from the decarboxylation of the linker during the synthesis. As UiO-66 is known to incorporate monodentate moieties in the form of defects this allowed us to hypothesize the presence of such defective structures decorated by propiolate moieties inside the MOF.

Ce-UiO-66-ADC is one of the very few MOFs (looking at the literature) containing the carbon triple bond. In this respect, the specific reactivity of this moiety may be exploited in various applications: for example the addition of a gaseous species (e.g. HCl) to the triple bond can be used to build an adsorber for this gas.

In conclusion, the present work demonstrates how it is possible to design and synthesize novel Ce-based MOFs. Till now, cerium was not commonly adopted in MOF synthesis, but, being, among rare earth metals, one of the most abundant, I thought its adoption would have been interesting. Finally, the explored field revealed to be very rich and malleable, also considering the possible imaginable applications.

Acknowledgements

I would like to thank my supervisor, Dr. Francesca Bonino, for her constant and irreplaceable guidance over these three years (and not only…) of PhD. Prof. Claudia Barolo and Prof. Silvia Bordiga are acknowledged for their supervision under some specific topics. I owe all of you my personal growth into scientific research during these years of PhD.

Professor Norbert Stock, from the University of Kiel, and his research group are acknowledged for having kindly welcome me in its laboratory in Kiel and for his precious supervision that introduced me into the realm of the MOF synthesis.

Prof. Karl Petter Lillerud and Dr. Sigurd Øien-Ødegaard, from the University of Oslo, are acknowledged for the fruitful discussions and for having done part of the crystallographic work reported in the present thesis.

I am grateful to Dr. Kirill Lomachenko and Prof. Carlo Lamberti for their work with X-Ray Absorption spectroscopies and all the scientists who helped us at the ID22 and the BM31 beamlines at the ESRF facility.

Concerning $Ce_2(ADB)_3(DMA)_{3.4}$ my acknowledgements are due to Gioele Giordanengo (MSc thesis student) for having done part of the experiments. The whole work-group about this activity is also acknowledged: Prof. Marco Milanesio, Prof. Bartolomeo Civalleri, Dr. Luca Palin and Dr. Nadia Barbero.

With regard to Ce-UiO-66-ADC topic, I am grateful to Alessia Airi (MSc thesis student) for her help with a relevant fraction of the experimental work.

H2020 project ProDIA (Project No. 685727) is acknowledged for having partially granted my PhD.

List of abbreviations

ASAP	Accelerated Surface Area and Porosimetry system
CAN	Cerium Ammonium Nitrate
CCD	Charge Coupled Device
CCDC	Cambridge Crystallographic Data Centre
CCUS	Carbon Capture, Utilization and Storage
CMOS	Complementary Metal-Oxide Semiconductor
CSD	Cambridge Structural Database
DABCO	1,4-diazabicyclo[2.2.2]octane
DMA	N,N-dimethylacetamide
DMF	N,N-dimethylformamide
DMSO	Dimethyl sulfoxide
EXAFS	Extended X-ray Absorption Fine Structure
FTIR	Fourier Transform Infrared Spectroscopy
H_2ADB	4,4'-azodibenzoic acid or 4,4'-(E)-diazene-1,2-diyldibenzoic acid
H_2ADC	Acetylenedicarboxylic acid or Butynedioic acid
H_2BDC	Terephthalic acid or Benzene-1,4-dicarboxylic acid
H_2NDC	2,6-Naphthalenedicarboxylic acid
H_4DSNDC	4,8-Disulfonyl-2,6-Naphthalenedicarboxylic acid
HKUST	Hong Kong University of Science and Technology
HT	High Throughput
ICP-MS	Inductively Coupled Plasma – Mass Spectrometry
IUPAC	International Union of Pure and Applied Chemistry

MCM	Mobil Composition of Matter
MIL	Matériaux de l′Institut Lavoisier
MOF	Metal-Organic Framework
PXRD	Powder X-Ray Diffraction
RCSR	Reticular Chemistry Structure Resource
SBA	Santa Barbara Amorphous
SBU	Structure Building Unit
SCXRD	Single-Crystal X-Ray Diffraction
SDA	Structure Directing Agent
SEM	Scanning Electron Microscopy
TCI	Tokyo Chemical Industry
TGA	Thermogravimetry Analysis
UiO	Universitetet i Oslo (University of Oslo)
UTSA	University of Texas at San Antonio
UV-Vis	Ultraviolet-Visible
VTXRD	Variable-Temperature X-Ray Diffraction
XAFS	X-Ray Absorption Fine Structure
XANES	X-Ray Absorption Near Edge Structure
XAS	X-Ray Absorption Spectroscopy
XPS	X-Ray Photoelectron Spectroscopy

Bibliography

(1) Kaskel, S. *The Chemistry of Metal-Organic Frameworks: Synthesis, Characterization, and Applications*; Kaskel, S., Ed.; John Wiley & Sons: Weinheim, 2016.

(2) Zhou, H.-C.; Long, J. R.; Yaghi, O. M. Introduction to Metal–Organic Frameworks. *Chem. Rev.* **2012**, *112*, 673–674.

(3) Long, J. R.; Yaghi, O. M. The Pervasive Chemistry of Metal-Organic Frameworks. *Chem. Soc. Rev.* **2009**, *38*, 1213–1214.

(4) Zhou, H. C. J.; Kitagawa, S. Metal-Organic Frameworks (MOFs). *Chem. Soc. Rev.* **2014**, *43*, 5415–5418.

(5) Furukawa, H.; Cordova, K. E. E.; O'Keeffe, M.; Yaghi, O. M. O. M.; O'Keeffe, M.; Yaghi, O. M. O. M. The Chemistry and Applications of Metal-Organic Frameworks. *Science* **2013**, *341*, 1230444.

(6) Butova, V. V; Soldatov, M. A.; Guda, A. A.; Lomachenko, K. A.; Lamberti, C. Metal-Organic Frameworks: Structure, Properties, Methods of Synthesis and Characterization. *Russ. Chem. Rev.* **2016**, *85*, 280–307.

(7) Batten, S. R.; Champness, N. R.; Chen, X.-M.; Garcia-Martinez, J.; Kitagawa, S.; Öhrström, L.; O'Keeffe, M.; Paik Suh, M.; Reedijk, J. Terminology of Metal–organic Frameworks and Coordination Polymers (IUPAC Recommendations 2013). *Pure Appl. Chem.* **2013**, *85*, 1715–1724.

(8) Yaghi, O. M.; Li, H. Hydrothermal Synthesis of a Metal-Organic Framework Containing Large Rectangular Channels. *J. Am. Chem. Soc.* **1995**, *117*, 10401–10402.

(9) Kinoshita, Y.; Matsubara, I.; Saito, Y. The Crystal Structure of Bis(Succinonitrilo)Copper(I) Nitrate. *Bull. Chem. Soc. Jpn.* **1959**, *32*, 741–747.

(10) Hoskins, B. F.; Robson, R. Infinite Polymeric Frameworks Consisting of Three Dimensionally Linked Rod-like Segments. *J. Am. Chem. Soc.* **1989**, *111*, 5962–5964.

(11) Kato, R.; Kobayashi, H.; Kobayashi, A. Crystal and Electronic Structures of Conductive Anion-Radical Salts, (2, 5-R1, R2-DCNQI)2Cu (DCNQI = N, N'-Dicyanoquinonediimme; R1, R2= CH3, CH3O, Cl, Br). *J. Am. Chem. Soc.* **1989**, *111*, 5224–5232.

(12) MacGillivray, L. R.; Subramanian, S.; Zaworotko, M. J. Interwoven Two-

and Three-Dimensional Coordination Polymers through Self-Assembly of CuIcations with Linear Bidentate Ligands. *J. Chem. Soc. Chem. Commun.* **1994**, No. 11, 1325–1326.

(13) Kitagawa, S.; Munakata, M.; Tanimura, T. Synthesis of the Novel Infinite-Sheet and -Chain Copper(I) Complex Polymers {[Cu(C4H4N2)3/2(CH3CN)](PF6).0.5C3H6O}∞ and |[Cu2(C8H12N2)3](CIO4)2}∞ and Their X-Ray Crystal Structures. *Inorg. Chem.* **1992**, *31*, 1714–1717.

(14) Yaghi, O. M.; Li, H. T-Shaped Molecular Building Units in the Porous Structure of Ag(4,4‘-Bpy)·NO $_3$. *J. Am. Chem. Soc.* **1996**, *118*, 295–296.

(15) Li, H.; Eddaoudi, M.; Groy, T. L.; Yaghi, O. M. Establishing Microporosity in Open Metal−Organic Frameworks: Gas Sorption Isotherms for Zn(BDC) (BDC = 1,4-Benzenedicarboxylate). *J. Am. Chem. Soc.* **1998**, *120*, 8571–8572.

(16) Li, H.; Eddaoudi, M.; O’Keeffe, M.; Yaghi, O. M. Design and Synthesis of an Exceptionally Stable and Highly Porous Metal-Organic Framework. *Nature* **1999**, *402*, 276–279.

(17) Chui, S. S. Y.; Lo, S. M. F.; Charmant, J. P. H.; Orpen, A. G.; Williams, I. D. A Chemically Functionalizable Nanoporous Material [Cu3(TMA)2 (H2O)3](N). *Science* **1999**, *283*, 1148–1150.

(18) Moghadam, P. Z.; Li, A.; Wiggin, S. B.; Tao, A.; Maloney, A. G. P.; Wood, P. A.; Ward, S. C.; Fairen-Jimenez, D. Development of a Cambridge Structural Database Subset: A Collection of Metal-Organic Frameworks for Past, Present, and Future. *Chem. Mater.* **2017**, *29*, 2618–2625.

(19) Yaghi, O. M.; O’Keeffe, M.; Ockwig, N. W.; Chae, H. K.; Eddaoudi, M.; Kim, J. Reticular Synthesis and the Design of New Materials. *Nature* **2003**, *423*, 705–714.

(20) Vitillo, J. G.; Atzori, C.; Civalleri, B.; Barbero, N.; Barolo, C.; Bonino, F. Design and Characterization of MOFs (Metal-Organic Frameworks) for Innovative Applications. In *Hybrid Organic-Inorganic Interfaces*; Wiley-VCH Verlag GmbH & Co. KGaA: Weinheim, Germany, 2017; pp 459–495.

(21) O’Keeffe, M.; Peskov, M. A.; Ramsden, S. J.; Yaghi, O. M. The Reticular Chemistry Structure Resource (RCSR) Database of, and Symbols for, Crystal Nets. *Acc. Chem. Res.* **2008**, *41*, 1782–1789.

(22) Cavka, J. H.; Jakobsen, S.; Olsbye, U.; Guillou, N.; Lamberti, C.; Bordiga, S.; Lillerud, K. P. A New Zirconium Inorganic Building Brick Forming Metal Organic Frameworks with Exceptional Stability. *J. Am. Chem. Soc.*

2008, *130*, 13850–13851.

(23) Research topics - Department of chemistry UiO https://www.mn.uio.no/kjemi/english/research/groups/catalysis/research/.

(24) Haxel, G. B.; Hedrick, J. B.; Orris, G. J. *Rare Earth Elements—Critical Resources for High Technology SUPPORTING SOUND MANAGEMENT OF OUR MINERAL RESOURCES*; 2002.

(25) Long, K. R.; Van Gosen, B. S.; Foley, N. K.; Cordier, D. *The Principal Rare Earth Elements Deposits of the United States: A Summary of Domestic Deposits and a Global Perspective*; 2012.

(26) Institut für Seltene Erden und Metalle (ISE, Germany) http://www.institut-seltene-erden.org/.

(27) Montini, T.; Melchionna, M.; Monai, M.; Fornasiero, P. Fundamentals and Catalytic Applications of CeO_2-Based Materials. *Chem. Rev.* **2016**, *116*, 5987–6041.

(28) Kašpar, J.; Fornasiero, P.; Graziani, M. Use of CeO_2-Based Oxides in the Three-Way Catalysis. *Catal. Today* **1999**, *50*, 285–298.

(29) Lammert, M. PhD Thesis, Christian-Albrechts-University, Kiel, 2017.

(30) Liang, L. L.; Xu, L.; Xue, H. B.; Tao, Z. L.; Chen, F. J. Two Metal-Organic Frameworks with Different Configurations Constructed from a Flexible Tripodal Triaromatic Acid. *J. Mol. Struct.* **2016**, *1125*, 656–661.

(31) Warren, J. E.; Perkins, C. G.; Jelfs, K. E.; Boldrin, P.; Chater, P. A.; Miller, G. J.; Manning, T. D.; Briggs, M. E.; Stylianou, K. C.; Claridge, J. B.; et al. Shape Selectivity by Guest-Driven Restructuring of a Porous Material. *Angew. Chemie - Int. Ed.* **2014**, *53*, 4592–4596.

(32) Li, Z.; Liu, K. Poly[(μ(4)-Benzene-1,3,5-Tricarboxyl-Ato)Bis-(N,N-Dimethyl-Formamide)-Cerium(III)]. *Acta Crystallogr. Sect. E. Struct. Rep. Online* **2011**, *67*, m1020.

(33) D'Arras, L.; Sassoye, C.; Rozes, L.; Sanchez, C.; Marrot, J.; Marre, S.; Aymonier, C. Fast and Continuous Processing of a New Sub-Micronic Lanthanide-Based Metal–organic Framework. *New J. Chem.* **2014**, *38*, 1477.

(34) Quah, H. S.; Ng, L. T.; Donnadieu, B.; Tan, G. K.; Vittal, J. J. Molecular Scissoring: Facile 3D to 2D Conversion of Lanthanide Metal Organic Frameworks Via Solvent Exfoliation. *Inorg. Chem.* **2016**, *55*, 10851–10854.

(35) Almáši, M.; Zeleňák, V.; Opanasenko, M.; Císařová, I. Ce(III) and Lu(III) Metal-Organic Frameworks with Lewis Acid Metal Sites: Preparation,

Sorption Properties and Catalytic Activity in Knoevenagel Condensation. *Catal. Today* **2015**, *243*, 3098–3114.

(36) Ethiraj, J.; Bonino, F.; Vitillo, J. G.; Lomachenko, K. A.; Lamberti, C.; Reinsch, H.; Lillerud, K. P.; Bordiga, S. Solvent-Driven Gate Opening in MOF-76-Ce: Effect on CO_2 Adsorption. *ChemSusChem* **2016**, *9*, 713–719.

(37) Ayhan, O.; Malaestean, I. L.; Ellern, A.; Van Leusen, J.; Baca, S. G.; Kögerler, P. Assembly of Cerium(III) 2,2′-Bipyridine-5,5′-Dicarboxylate-Based Metal-Organic Frameworks by Solvent Tuning. *Cryst. Growth Des.* **2014**, *14*, 3541–3548.

(38) Bag, P. P.; Wang, X. S.; Cao, R. Microwave-Assisted Large Scale Synthesis of Lanthanide Metal-Organic Frameworks (Ln-MOFs), Having a Preferred Conformation and Photoluminescence Properties. *Dalton Trans.* **2015**, *44*, 11954–11962.

(39) Zhai, L.; Zhang, W. W.; Ren, X. M.; Zuo, J. L. Luminescent Lanthanide MOFs Based on Conjugated 1,1′-Ethynebenzene-3,3′,5,5′-Tetracarboxylate Ligand: Syntheses, Structures and Photoluminescent Properties. *Dalton Trans.* **2015**, *44*, 5746–5754.

(40) Wang, C.; Li, L.; Bell, J. G.; Lv, X.; Tang, S.; Zhao, X.; Thomas, K. M. Hysteretic Gas and Vapor Sorption in Flexible Interpenetrated Lanthanide-Based Metal-Organic Frameworks with Coordinated Molecular Gating via Reversible Single-Crystal-to-Single-Crystal Transformation for Enhanced Selectivity. *Chem. Mater.* **2015**, *27*, 1502–1516.

(41) Wu, Y. P.; Li, D. S.; Xia, W.; Guo, S. S.; Dong, W. W. Three Novel Lanthanide Metal-Organic Frameworks (Ln-MOFs) Constructed by Unsymmetrical Aromatic Dicarboxylatic Tectonics: Synthesis, Crystal Structures and Luminescent Properties. *Molecules* **2014**, *19*, 14352–14365.

(42) Das, S. K.; Chatterjee, S.; Bhunia, S.; Mondal, A.; Mitra, P.; Kumari, V.; Pradhan, A.; Bhaumik, A. A New Strongly Paramagnetic Cerium-Containing Microporous MOF for CO_2 Fixation under Ambient Conditions. *Dalton Trans.* **2017**, *46*, 13783–13792.

(43) Liu, Y. H.; Chien, P. H. A Series of Lanthanide-Organic Frameworks Possessing Arrays of 2D Intersecting Channels within a 3D Pillar-Supported Packed Double-Decker Network and Co^{2+}-Induced Luminescence Modulation. *CrystEngComm* **2014**, *16*, 8852–8862.

(44) Nandi, G.; Thakuria, R.; Titi, H. M.; Patra, R.; Goldberg, I. Synthesis, Structure, Topology and Magnetic Properties of New Coordination Polymers Based on 5(-Br/-COOH)-Substituted Nicotinic Acid. *CrystEngComm* **2014**, *16*, 5244–5256.

(45) Nandi, G.; Titi, H. M.; Thakuria, R.; Goldberg, I. Solvent Dependent Formation of Metallogels and Single-Crystal MOFs by La(III) and Ce(III) Connectors and 3,5-Pyridinedicarboxylate. *Cryst. Growth Des.* **2014**, *14*, 2714–2719.

(46) Silva, P.; Ananias, D.; Bruno, S. M.; Valente, A. A.; Carlos, L. D.; Rocha, J.; Almeida Paz, F. A. Photoluminescent Metal-Organic Frameworks - Rapid Preparation, Catalytic Activity, and Framework Relationships. *Eur. J. Inorg. Chem.* **2013**, *2013*, 5576–5591.

(47) Jia, L. N.; Hou, L.; Wei, L.; Jing, X. J.; Liu, B.; Wang, Y. Y.; Shi, Q. Z. Five Sra Topological Ln(III)-MOFs Based on Novel Metal-Carboxylate/Cl Chain: Structure, near-Infrared Luminescence and Magnetic Properties. *Cryst. Growth Des.* **2013**, *13*, 1570–1576.

(48) Tang, Q.; Liu, S.; Liu, Y.; Miao, J.; Li, S.; Zhang, L.; Shi, Z.; Zheng, Z. Cation Sensing by a Luminescent Metal-Organic Framework with Multiple Lewis Basic Sites. *Inorg. Chem.* **2013**, *52*, 2799–2801.

(49) Nayak, S.; Nayek, H. P.; Pietzonka, C.; Novitchi, G.; Dehnen, S. A Series of Three-Dimensional Lanthanide MOFs: Observation of Reversible Structural Changes Controlled by Solvent Desorption-Adsorption, and Magnetic Properties. *J. Mol. Struct.* **2011**, *1004*, 82–87.

(50) Han, Y.; Li, X.; Li, L.; Ma, C.; Shen, Z.; Song, Y.; You, X. Structures and Properties of Porous Coordination Polymers Based on Lanthanide Carboxylate Building Units. *Inorg. Chem.* **2010**, *49*, 10781–10787.

(51) Neofotistou, E.; Malliakas, C. D.; Trikalitis, P. N. Remarkable Structural Diversity and Single-Crystal-to-Single-Crystal Transformations in Sulfone Functionalized Lanthanide MOFs. *CrystEngComm* **2010**, *12*, 1034–1037.

(52) Devic, T.; Wagner, V.; Guillou, N.; Vimont, A.; Haouas, M.; Pascolini, M.; Serre, C.; Marrot, J.; Daturi, M.; Taulelle, F.; et al. Synthesis and Characterization of a Series of Porous Lanthanide Tricarboxylates. *Microporous Mesoporous Mater.* **2011**, *140*, 25–33.

(53) Pan, L.; Adams, K. M.; Hernandez, H. E.; Wang, X.; Zheng, C.; Hattori, Y.; Kaneko, K. Porous Lanthanide-Organic Frameworks: Synthesis, Characterization, and Unprecedented Gas Adsorption Properties. *J. Am. Chem. Soc.* **2003**, *125*, 3062–3067.

(54) Lammert, M.; Wharmby, M. T.; Smolders, S.; Bueken, B.; Lieb, A.; Lomachenko, K. A.; Vos, D. De; Stock, N. Cerium-Based Metal Organic Frameworks with UiO-66 Architecture: Synthesis, Properties and Redox Catalytic Activity. *Chem. Commun.* **2015**, *51*, 12578–12581.

(55) Lammert, M.; Reinsch, H.; Murray, C. A.; Wharmby, M. T.; Terraschke, H.; Stock, N. Synthesis and Structure of Zr(IV)- and Ce(IV)-Based CAU-24 with 1,2,4,5-Tetrakis(4-Carboxyphenyl)Benzene. *Dalton Trans.* **2016**, *45*, 18822–18826.

(56) Dreischarf, A. C.; Lammert, M.; Stock, N.; Reinsch, H. Green Synthesis of Zr-CAU-28: Structure and Properties of the First Zr-MOF Based on 2,5-Furandicarboxylic Acid. *Inorg. Chem.* **2017**, *56*, 2270–2277.

(57) Lammert, M.; Glißmann, C.; Reinsch, H.; Stock, N. Synthesis and Characterization of New Ce(IV)-MOFs Exhibiting Various Framework Topologies. *Cryst. Growth Des.* **2017**, *17*, 1125–1131.

(58) Waitschat, S.; Fröhlich, D.; Reinsch, H.; Terraschke, H.; Lomachenko, K. A.; Lamberti, C.; Kummer, H.; Helling, T.; Baumgartner, M.; Henninger, S.; et al. Synthesis of M-UiO-66 (M = Zr, Ce or Hf) Employing 2,5-Pyridinedicarboxylic Acid as a Linker: Defect Chemistry, Framework Hydrophilisation and Sorption Properties. *Dalton Trans.* **2018**, *47*, 1062–1070.

(59) SK, M.; Grzywa, M.; Volkmer, D.; Biswas, S. Zr(IV) and Ce(IV)-Based Metal-Organic Frameworks Incorporating 4-Carboxycinnamic Acid as Ligand: Synthesis and Properties. *Microporous Mesoporous Mater.* **2017**, *237*, 275–281.

(60) Jacobsen, J.; Reinsch, H.; Stock, N. Systematic Investigations of the Transition between Framework Topologies in Ce/Zr-MOFs. *Inorg. Chem.* **2018**, *57*, acs.inorgchem.8b02019.

(61) Smolders, S.; Struyf, A.; Reinsch, H.; Bueken, B.; Rhauderwiek, T.; Mintrop, L.; Kurz, P.; Stock, N.; De Vos, D. E. A Precursor Method for the Synthesis of New Ce(IV) MOFs with ReactIVe Tetracarboxylate Linkers. *Chem. Commun.* **2018**, *54*, 876–879.

(62) Smolders, S.; Lomachenko, K. A.; Bueken, B.; Struyf, A.; Bugaev, A. L.; Atzori, C.; Stock, N.; Lamberti, C.; Roeffaers, M. B. J.; De Vos, D. E. Unravelling the Redox-Catalytic Behavior of Ce^{4+} Metal–Organic Frameworks by X-Ray Absorption Spectroscopy. *ChemPhysChem* **2018**, *19*.

(63) Yang, X.; Xu, Q. Bimetallic Metal-Organic Frameworks for Gas Storage and Separation. *Cryst. Growth Des.* **2017**, *17*, 1450–1455.

(64) Lammert, M.; Glißmann, C.; Stock, N. Tuning the Stability of Bimetallic Ce(IV)/Zr(IV)-Based MOFs with UiO-66 and MOF-808 Structures. *Dalton Trans.* **2017**, *46*, 2425–2429.

(65) Brozek, C. K.; Dincă, M. Ti^{3+}-, $V^{2+/3+}$-, $Cr^{2+/3+}$-, Mn^{2+}-, and Fe^{2+}-Substituted

MOF-5 and Redox Reactivity in Cr- and Fe-MOF-5. *J. Am. Chem. Soc.* **2013**, *135*, 12886–12891.

(66) Stubbs, A. W.; Braglia, L.; Borfecchia, E.; Meyer, R. J.; Román-Leshkov, Y.; Lamberti, C.; Dincă, M. Selective Catalytic Olefin Epoxidation with Mn(II)-Exchanged MOF-5. *ACS Catal.* **2018**, *8*, 596–601.

(67) Marshall, R. J.; Forgan, R. S. Postsynthetic Modification of Zirconium Metal-Organic Frameworks. *Eur. J. Inorg. Chem.* **2016**, *2016*, 4310–4331.

(68) Kim, M.; Cahill, J. F.; Fei, H.; Prather, K. A.; Cohen, S. M. Postsynthetic Ligand and Cation Exchange in Robust Metal–Organic Frameworks. *J. Am. Chem. Soc.* **2012**, *134*, 18082–18088.

(69) Gul-E-Noor, F.; Jee, B.; Mendt, M.; Himsl, D.; Pöppl, A.; Hartmann, M.; Haase, J.; Krautscheid, H.; Bertmer, M. Formation of Mixed Metal $Cu_{3-x}Zn_x(Btc)_2$frameworks with Different Zinc Contents: Incorporation of Zn^{2+}into the Metal-Organic Framework Structure as Studied by Solid-State NMR. *J. Phys. Chem. C* **2012**, *116*, 20866–20873.

(70) Gotthardt, M. A.; Schoch, R.; Wolf, S.; Bauer, M.; Kleist, W. Synthesis and Characterization of Bimetallic Metal-Organic Framework Cu-Ru-BTC with HKUST-1 Structure. *Dalton Trans.* **2015**, *44*, 2052–2056.

(71) Sun, D.; Sun, F.; Deng, X.; Li, Z. Mixed-Metal Strategy on Metal-Organic Frameworks (MOFs) for Functionalities Expansion: Co Substitution Induces Aerobic Oxidation of Cyclohexene over Inactive Ni-MOF-74. *Inorg. Chem.* **2015**, *54*, 8639–8643.

(72) Liu, Q.; Cong, H.; Deng, H. Deciphering the Spatial Arrangement of Metals and Correlation to Reactivity in Multivariate Metal-Organic Frameworks. *J. Am. Chem. Soc.* **2016**, *138*, 13822–13825.

(73) Zhai, Q. G.; Bu, X.; Mao, C.; Zhao, X.; Feng, P. Systematic and Dramatic Tuning on Gas Sorption Performance in Heterometallic Metal-Organic Frameworks. *J. Am. Chem. Soc.* **2016**, *138*, 2524–2527.

(74) He, J.; Zhang, Y.; He, J.; Zeng, X.; Hou, X.; Long, Z. Enhancement of Photoredox Catalytic Properties of Porphyrinic Metal-Organic Frameworks Based on Titanium Incorporation via Post-Synthetic Modification. *Chem. Commun.* **2018**, *54*, 8610–8613.

(75) Vuong, G. T.; Pham, M. H.; Do, T. O. Synthesis and Engineering Porosity of a Mixed Metal Fe2Ni MIL-88B Metal-Organic Framework. *Dalton Trans.* **2013**, *42*, 550–557.

(76) Stock, N.; Biswas, S. Synthesis of Metal-Organic Frameworks (MOFs):

Routes to Various MOF Topologies, Morphologies, and Composites. *Chem. Rev.* **2012**, *112*, 933–969.

(77) Allendorf, M. D.; Stavila, V. Crystal Engineering, Structure–function Relationships, and the Future of Metal–organic Frameworks. *CrystEngComm* **2015**, *17*, 229–246.

(78) Øien-Ødegaard, S.; Shearer, G. C.; Lillerud, K. P.; Bordiga, S. Metal-Organic Framework Sponges; In press, 2018.

(79) Hermes, S.; Witte, T.; Hikov, T.; Zacher, D.; Bahnm??ller, S.; Langstein, G.; Huber, K.; Fischer, R. A. Trapping Metal-Organic Framework Nanocrystals: An in-Situ Time-Resolved Light Scattering Study on the Crystal Growth of MOF-5 in Solution. *J. Am. Chem. Soc.* **2007**, *129*, 5324–5325.

(80) Schaate, A.; Roy, P.; Godt, A.; Lippke, J.; Waltz, F.; Wiebcke, M.; Behrens, P. Modulated Synthesis of Zr-Based Metal-Organic Frameworks: From Nano to Single Crystals. *Chem. Eur. J.* **2011**, *17*, 6643–6651.

(81) Shearer, G. C.; Chavan, S.; Bordiga, S.; Svelle, S.; Olsbye, U.; Lillerud, K. P. Defect Engineering: Tuning the Porosity and Composition of the Metal-Organic Framework UiO-66 via Modulated Synthesis. *Chem. Mater.* **2016**, *28*, 3749–3761.

(82) Shearer, G. C. On the Defect Chemistry of the Metal-Organic Framework UiO-66, University of Oslo, 2015.

(83) Atzori, C.; Shearer, G. C.; Maschio, L.; Civalleri, B.; Bonino, F.; Lamberti, C.; Svelle, S.; Lillerud, K. P.; Bordiga, S. Effect of Benzoic Acid as a Modulator in the Structure of UiO-66: An Experimental and Computational Study. *J. Phys. Chem. C* **2017**, *121*.

(84) Butova, V. V.; Budnyk, A. P.; Guda, A. A.; Lomachenko, K. A.; Bugaev, A. L.; Soldatov, A. V.; Chavan, S. M.; Øien-Ødegaard, S.; Olsbye, U.; Lillerud, K. P.; et al. Modulator Effect in UiO-66-NDC (1,4-Naphthalenedicarboxylic Acid) Synthesis and Comparison with UiO-67-NDC Isoreticular Metal–Organic Frameworks. *Cryst. Growth Des.* **2017**, acs.cgd.7b00892.

(85) Klein, N.; Herzog, C.; Sabo, M.; Senkovska, I.; Getzschmann, J.; Paasch, S.; Lohe, M. R.; Brunner, E.; Kaskel, S. Monitoring Adsorption-Induced Switching by ^{129}Xe NMR Spectroscopy in a New Metal-Organic Framework $Ni_2(2,6\text{-}Ndc)_2(Dabco)$. *Phys. Chem. Chem. Phys.* **2010**, *12*, 11778–11784.

(86) Bon, V.; Kavoosi, N.; Senkovska, I.; Kaskel, S. Tolerance of Flexible MOFs toward Repeated Adsorption Stress. *ACS Appl. Mater. Interfaces* **2015**, *7*, 22292–22300.

(87) Stock, N. High-Throughput Investigations Employing Solvothermal Syntheses. *Microporous Mesoporous Mater.* **2010**, *129*, 287–295.

(88) Albat, M.; Stock, N. Multiparameter High-Throughput and in Situ X-Ray Diffraction Study of Six New Bismuth Sulfonatocarboxylates: Discovery, Phase Transformation, and Reaction Trends. *Inorg. Chem.* **2018**, *57*, 10352–10363.

(89) Horcajada, P.; Chalati, T.; Serre, C.; Gillet, B.; Sebrie, C.; Baati, T.; Eubank, J. F.; Heurtaux, D.; Clayette, P.; Kreuz, C.; et al. Porous Metal–organic-Framework Nanoscale Carriers as a Potential Platform for Drug Delivery and Imaging. *Nat. Mater.* **2010**, *9*, 172–178.

(90) Kandiah, M.; Nilsen, M. H.; Usseglio, S.; Jakobsen, S.; Olsbye, U.; Tilset, M.; Larabi, C.; Quadrelli, E. A.; Bonino, F.; Lillerud, K. P. Synthesis and Stability of Tagged UiO-66 Zr-MOFs. *Chem. Mater.* **2010**, *22*, 6632–6640.

(91) Chavan, S. M.; Shearer, G. C.; Svelle, S.; Olsbye, U.; Bonino, F.; Ethiraj, J.; Lillerud, K. P.; Bordiga, S. Synthesis and Characterization of Amine-Functionalized Mixed- Ligand Metal − Organic Frameworks of UiO-66 Topology. *Inorg. Chem.* **2014**, *53*, 9509–9515.

(92) Tanabe, K. K.; Cohen, S. M. Postsynthetic Modification of Metal-Organic Frameworks - A Progress Report. *Chem. Soc. Rev.* **2011**, *40*, 498–519.

(93) Deria, P.; Mondloch, J. E.; Karagiaridi, O.; Bury, W.; Hupp, J. T.; Farha, O. K. Beyond Post-Synthesis Modification: Evolution of Metal-Organic Frameworks via Building Block Replacement. Royal Society of Chemistry 2014, pp 5896–5912.

(94) Shearer, G. C.; Vitillo, J. G.; Bordiga, S.; Svelle, S.; Olsbye, U.; Lillerud, K. P. Functionalizing the Defects: Postsynthetic Ligand Exchange in the Metal Organic Framework UiO-66. *Chem. Mater.* **2016**, *28*, 7190–7193.

(95) Øien, S.; Agostini, G.; Svelle, S.; Borfecchia, E.; Lomachenko, K. A.; Mino, L.; Gallo, E.; Bordiga, S.; Olsbye, U.; Lillerud, K. P.; et al. Probing Reactive Platinum Sites in Uio-67 Zirconium Metal-Organic Frameworks. *Chem. Mater.* **2015**, *27*, 1042–1056.

(96) Braglia, L.; Borfecchia, E.; Maddalena, L.; Øien, S.; Lomachenko, K. A.; Bugaev, A. L.; Bordiga, S.; Soldatov, A. V.; Lillerud, K. P.; Lamberti, C. Exploring Structure and Reactivity of Cu Sites in Functionalized UiO-67 MOFs. Elsevier 2015.

(97) Howarth, A. J.; Peters, A. W.; Vermeulen, N. A.; Wang, T. C.; Hupp, J. T.; Farha, O. K. Best Practices for the Synthesis, Activation, and Characterization of Metal−organic Frameworks. *Chem. Mater.* **2017**, *29*,

26–39.

(98) Giacovazzo, C.; Monaco, H. L.; Artioli, G.; Viterbo, D.; Milanesio, M.; Gilli, G.; Gilli, P.; Zanotti, G.; Ferraris, G.; Catti, M. *Fundamentals of Crystallography*; International Union of Crystallography Texts on Crystallography; OUP Oxford, 2011.

(99) Dyadkin, V.; Pattison, P.; Dmitriev, V.; Chernyshov, D. A New Multipurpose Diffractometer PILATUS@SNBL. *J. Synchrotron Radiat.* **2016**, *23*, 825–829.

(100) Thommes, M.; Kaneko, K.; Neimark, A. V.; Olivier, J. P.; Rodriguez-Reinoso, F.; Rouquerol, J.; Sing, K. S. W. Physisorption of Gases, with Special Reference to the Evaluation of Surface Area and Pore Size Distribution (IUPAC Technical Report). **2015**, *87*, 1051–1069.

(101) Bokhoven, J. A. van; Lamberti, C. *X-Ray Absorption and X-Ray Emission Spectroscopy : Theory and Applications*; Wiley, 2016.

(102) Soldatov, M. A.; Martini, A.; Bugaev, A. L.; Pankin, I.; Medvedev, P. V.; Guda, A. A.; Aboraia, A. M.; Podkovyrina, Y. S.; Budnyk, A. P.; Soldatov, A. A.; et al. The Insights from X-Ray Absorption Spectroscopy into the Local Atomic Structure and Chemical Bonding of Metal–organic Frameworks. *Polyhedron* **2018**, *155*, 232–253.

(103) Valenzano, L.; Civalleri, B.; Chavan, S.; Bordiga, S.; Nilsen, M. H.; Jakobsen, S.; Lillerud, K. P.; Lamberti, C. Disclosing the Complex Structure of UiO-66 Metal Organic Framework: A Synergic Combination of Experiment and Theory. *Chem. Mater.* **2011**, *23*, 1700–1718.

(104) Chavan, S.; Vitillo, J. G.; Gianolio, D.; Zavorotynska, O.; Civalleri, B.; Jakobsen, S.; Nilsen, M. H.; Valenzano, L.; Lamberti, C.; Lillerud, K. P.; et al. H 2 Storage in Isostructural UiO-67 and UiO-66 MOFs. *Phys. Chem. Chem. Phys.* **2012**, *14*, 1614–1626.

(105) Jakobsen, S.; Gianolio, D.; Wragg, D. S.; Nilsen, M. H.; Emerich, H.; Bordiga, S.; Lamberti, C.; Olsbye, U.; Tilset, M.; Lillerud, K. P. Structural Determination of a Highly Stable Metal-Organic Framework with Possible Application to Interim Radioactive Waste Scavenging: Hf-UiO-66. *Phys. Rev. B - Condens. Matter Mater. Phys.* **2012**, *86*, 125429.

(106) Prestipino, C.; Regli, L.; Vitillo, J. G.; Bonino, F.; Damin, A.; Lamberti, C.; Zecchina, A.; Solari, P. L.; Kongshaug, K. O.; Bordiga, S. Local Structure of Framework Cu(II) in HKUST-1 Metallorganic Framework: Spectroscopic Characterization upon Activation and Interaction with Adsorbates. *Chem. Mater.* **2006**, *18*, 1337–1346.

(107) Masciocchi, N.; Galli, S.; Colombo, V.; Maspero, A.; Palmisano, G.; Seyyedi, B.; Lamberti, C.; Bordiga, S. Cubic Octanuclear Ni(II) Clusters in Highly Porous Polypyrazolyl-Based Materials. *J. Am. Chem. Soc.* **2010**, *132*, 7902–7904.

(108) Millward, A. R.; Yaghi, O. M. Metal-Organic Frameworks with Exceptionally High Capacity for Storage of Carbon Dioxide at Room Temperature. *J. Am. Chem. Soc.* **2005**, *127*, 17998–17999.

(109) Sumida, K.; Rogow, D. L.; Mason, J. A.; McDonald, T. M.; Bloch, E. D.; Herm, Z. R.; Bae, T.-H.; Long, J. R. Carbon Dioxide Capture in Metal–Organic Frameworks. *Chem. Rev.* **2012**, *112*, 724–781.

(110) Peng, Y.; Krungleviciute, V.; Eryazici, I.; Hupp, J. T.; Farha, O. K.; Yildirim, T. Methane Storage in Metal-Organic Frameworks: Current Records, Surprise Findings, and Challenges. *J. Am. Chem. Soc.* **2013**, *135*, 11887–11894.

(111) Bae, Y. S.; Snurr, R. Q. Development and Evaluation of Porous Materials for Carbon Dioxide Separation and Capture. *Angew. Chemie - Int. Ed.* **2011**, *50*, 11586–11596.

(112) Patel, H. A.; Byun, J.; Yavuz, C. T. Carbon Dioxide Capture Adsorbents: Chemistry and Methods. *ChemSusChem* **2017**, *10*, 1303–1317.

(113) Llabres i Xamena, F.; Gascon, J. *Metal Organic Frameworks as Heterogeneous Catalysts*; Llabres i Xamena, F., Gascon, J., Eds.; Catalysis Series; Royal Society of Chemistry: Cambridge, 2013.

(114) Gascon, J.; Corma, A.; Kapteijn, F.; Llabrés I Xamena, F. X. Metal Organic Framework Catalysis: Quo Vadis? *ACS Catal.* **2014**, *4*, 361–378.

(115) Rogge, S. M. J.; Bavykina, A.; Hajek, J.; Garcia, H.; Olivos-Suarez, A. I.; Sepúlveda-Escribano, A.; Vimont, A.; Clet, G.; Bazin, P.; Kapteijn, F.; et al. Metal–organic and Covalent Organic Frameworks as Single-Site Catalysts. *Chem. Soc. Rev.* **2017**, *46*, 3134–3184.

(116) Farrusseng, D.; Aguado, S.; Pinel, C. Metal-Organic Frameworks: Opportunities for Catalysis. *Angew. Chemie - Int. Ed.* **2009**, *48*, 7502–7513.

(117) Ullman, A. M.; Brown, J. W.; Foster, M. E.; Léonard, F.; Leong, K.; Stavila, V.; Allendorf, M. D. Transforming MOFs for Energy Applications Using the Guest@MOF Concept. *Inorg. Chem.* **2016**, *55*, 7233–7249.

(118) Han, Y.; Liu, M.; Li, K.; Zuo, Y.; Wei, Y.; Xu, S.; Zhang, G.; Song, C.; Zhang, Z. C.; Guo, X. Facile Synthesis of Morphology- and Size-Controlled Zirconium Metal-Organic Framework UiO-66: The Role of Hydrofluoric

Acid in Crystallization. *CrystEngComm* **2015**, *17*, 1–9.

(119) So, M. C.; Wiederrecht, G. P.; Mondloch, J. E.; Hupp, J. T.; Farha, O. K. Metal-Organic Framework Materials for Light-Harvesting and Energy Transfer. *Chem. Commun.* **2015**, *51*, 3501–3510.

(120) Zhang, T.; Lin, W. Metal-Organic Frameworks for Artificial Photosynthesis and Photocatalysis. *Chem. Soc. Rev.* **2014**, *43*, 5982–5993.

(121) Lee, C. Y.; Farha, O. K.; Hong, B. J.; Sarjeant, A. A.; Nguyen, S. T.; Hupp, J. T. Light-Harvesting Metal-Organic Frameworks (MOFs): Efficient Strut-to-Strut Energy Transfer in Bodipy and Porphyrin-Based MOFs. *J. Am. Chem. Soc.* **2011**, *133*, 15858–15861.

(122) Wang, L.; Han, Y.; Feng, X.; Zhou, J.; Qi, P.; Wang, B. Metal-Organic Frameworks for Energy Storage: Batteries and Supercapacitors. *Coord. Chem. Rev.* **2016**, *307*, 361–381.

(123) Sun, L.; Campbell, M. G.; Dincə, M. Electrically Conductive Porous Metal-Organic Frameworks. *Angew. Chemie - Int. Ed.* **2016**, *55*, 3566–3579.

(124) Son, H.-J.; Jin, S.; Patwardhan, S.; Wezenberg, S. J.; Jeong, N. C.; So, M.; Wilmer, C. E.; Sarjeant, A. A.; Schatz, G. C.; Snurr, R. Q.; et al. Light-Harvesting and Ultrafast Energy Migration in Porphyrin-Based Metal−Organic Frameworks. *J. Am. Chem. Soc.* **2013**, *135*, 862−869.

(125) Lee, D. Y.; Kim, E. K.; Shin, C. Y.; Shinde, D. V.; Lee, W.; Shrestha, N. K.; Lee, J. K.; Han, S. H. Layer-by-Layer Deposition and Photovoltaic Property of Ru-Based Metal-Organic Frameworks. *RSC Adv.* **2014**, *4*, 12037–12042.

(126) Leong, K.; Foster, M.; Wong, B.; Spoerker, E.; Van Gough, D.; Deaton, J.; Allendorf, M. Energy and Charge Transfer by Donor–acceptor Pairs Confined in a Metal–organic Framework: A Spectroscopic and Computational Investigation. *J. Mater. Chem. A* **2014**, *2*, 3389–3398.

(127) Li, Y.; Chen, C.; Sun, X.; Dou, J.; Wei, M. Metal–Organic Frameworks at Interfaces in Dye-Sensitized Solar Cells. *ChemSusChem* **2014**, *7*, 2469–2472.

(128) Lee, D. Y.; Lim, I.; Shin, C. Y.; Patil, S. A.; Lee, W.; Shrestha, N. K.; Lee, J. K.; Han, S. H. Facile Interfacial Charge Transfer across Hole Doped Cobalt-Based MOFs/TiO_2 Nano-Hybrids Making MOFs Light Harvesting Active Layers in Solar Cells. *J. Mater. Chem. A* **2015**, *3*, 22669–22676.

(129) Bella, F.; Bongiovanni, R.; Kumar, R. S.; Kulandainathan, M. A.; Stephan, A. M. Light Cured Networks Containing Metal Organic Frameworks as Efficient and Durable Polymer Electrolytes for Dye-Sensitized Solar Cells.

J. Mater. Chem. A **2013**, *1*, 9033–9036.

(130) Giordanengo, G. Sintesi e Caratterizzazione Di Un Nuovo Polimero Di Coordinazione Metallo-Organico a Base Di Cerio Con Legante Azoico, Università di Torino, 2017.

(131) Boghici, A. R. Sintesi Del MOF Ce-UiO-66-ADC, Università di Torino, 2017.

(132) Airi, A. A Tough MOF with a Fragile Linker: Ce-UiO-66-ADC, Università di Torino, 2018.

(133) Sheldrick, G. M. Crystal Structure Refinement with SHELXL. *Acta Crystallogr. Sect. C Struct. Chem.* **2015**, *71*, 3–8.

(134) Stoe & Cie. X-Shape, X-Area and X-Red. Stoe & Cie: Darmstadt, Germany 2002.

(135) Burla, M. C.; Caliandro, R.; Carrozzini, B.; Cascarano, G. L.; Cuocci, C.; Giacovazzo, C.; Mallamo, M.; Mazzone, A.; Polidori, G. Crystal Structure Determination and Refinement via SIR2014. *J. Appl. Crystallogr.* **2015**, *48*, 306–309.

(136) Macrae, C. F.; Bruno, I. J.; Chisholm, J. A.; Edgington, P. R.; McCabe, P.; Pidcock, E.; Rodriguez-Monge, L.; Taylor, R.; Van De Streek, J.; Wood, P. A. Mercury CSD 2.0 - New Features for the Visualization and Investigation of Crystal Structures. *Journal of Applied Crystallography*. International Union of Crystallography April 1, 2008, pp 466–470.

(137) Coelho, A. A. TOPAS and TOPAS-Academic: An Optimization Program Integrating Computer Algebra and Crystallographic Objects Written in C++: An. *J. Appl. Crystallogr.* **2018**, *51*, 210–218.

(138) Abdala, P. M.; Safonova, O. V.; Wiker, G.; van Beek, W.; Emerich, H.; van Bokhoven, J. A.; Sá, J.; Szlachetko, J.; Nachtegaal, M. Scientific Opportunities for Heterogeneous Catalysis Research at the SuperXAS and SNBL Beam Lines. *Chim. Int. J. Chem.* **2012**, *66*, 699–705.

(139) Klementiev, K.; Chernikov, R. XAFSmass: A Program for Calculating the Optimal Mass of XAFS Samples. *J. Phys. Conf. Ser.* **2016**, *712*, 012008.

(140) Ravel, B.; Newville, M. ATHENA, ARTEMIS, HEPHAESTUS: Data Analysis for X-Ray Absorption Spectroscopy Using IFEFFIT. *J. Synchrotron Radiat.* **2005**, *12*, 537–541.

(141) Rehr, J. J.; Albers, R. C. Theoretical Approaches to X-Ray Absorption Fine Structure. *Rev. Mod. Phys.* **2000**, *72*, 621–654.

(142) Signorile, M.; Bonino, F.; Damin, A.; Bordiga, S. A Novel Raman Setup Based on Magnetic-Driven Rotation of Sample. *Top. Catal.* **2018**, *61*, 1491–1498.

(143) Colthup, N. B.; Daly, L. H.; Wiberley, S. E. *Introduction to Infrared and Raman Spectroscopy*; Academic Press, 1990.

(144) Schneemann, A.; Bon, V.; Schwedler, I.; Senkovska, I.; Kaskel, S.; Fischer, R. A. Flexible Metal-Organic Frameworks. *Chem. Soc. Rev.* **2014**, *43*, 6062–6096.

(145) Serre, C.; Bourrelly, S.; Vimont, A.; Ramsahye, N. A.; Maurin, G.; Llewellyn, P. L.; Daturi, M.; Filinchuk, Y.; Leynaud, O.; Barnes, P.; et al. An Explanation for the Very Large Breathing Effect of a Metal–Organic Framework during CO2 Adsorption. *Adv. Mater.* **2007**, *19*, 2246–2251.

(146) Gregg, S. J.; Sing, K. S. W. *Adsorption, Surface Area and Porosity*; Academic Press, 1982.

(147) Rouquerol, J. *Adsorption by Powders and Porous Solids : Principles, Methodology and Applications*.

(148) Masala, A.; Vitillo, J. G.; Mondino, G.; Grande, C. A.; Blom, R.; Manzoli, M.; Marshall, M.; Bordiga, S. CO_2 Capture in Dry and Wet Conditions in UTSA-16 Metal–Organic Framework. *ACS Appl. Mater. Interfaces* **2017**, *9*, 455–463.

(149) Øien, S.; Wragg, D.; Reinsch, H.; Svelle, S.; Bordiga, S.; Lamberti, C.; Lillerud, K. P. Detailed Structure Analysis of Atomic Positions and Defects in Zirconium Metal-Organic Frameworks. *Cryst. Growth Des.* **2014**, *14*, 5370–5372.

(150) Pecharsky Vitalij, Z. P. *Fundamentals of Powder Diffraction and Structural Characterization of Materials*, second.; Springer US, 2009.

(151) Bonino, F.; Damin, A.; Bordiga, S.; Lamberti, C.; Zecchina, A. Interaction of CD_3CN and Pyridine with the Ti(IV) Centers of TS-1 Catalysts: A Spectroscopic and Computational Study. *Langmuir* **2003**, *19*, 2155–2161.

(152) Proust, B. Synthesis and Characterization of Cerium(IV)-Based MOF, ENSICAEN, Università di Torino, 2015.

(153) Nouar, F.; Breeze, M. I.; Campo, B. C.; Vimont, A.; Clet, G.; Daturi, M.; Devic, T.; Walton, R. I.; Serre, C. Tuning the Properties of the UiO-66 Metal Organic Framework by Ce Substitution. *Chem. Commun.* **2015**, *51*, 14458–14461.

(154) Shearer, G. C.; Forselv, S.; Chavan, S.; Bordiga, S.; Mathisen, K.; Bjorgen,

M.; Svelle, S.; Lillerud, K. P. In Situ Infrared Spectroscopic and Gravimetric Characterisation of the Solvent Removal and Dehydroxylation of the Metal Organic Frameworks UiO-66 and UiO-67. *Top. Catal.* **2013**, *56*, 770–782.

(155) Tranchemontagne, D. J.; Hunt, J. R.; Yaghi, O. M. Room Temperature Synthesis of Metal-Organic Frameworks: MOF-5, MOF-74, MOF-177, MOF-199, and IRMOF-0. *Tetrahedron* **2008**, *64*, 8553–8557.

(156) Li, J.; Brill, T. B. Spectroscopy of Hydrothermal Reactions 20: Experimental and DFT Computational Comparison of Decarboxylation of Dicarboxylic Acids Connected by Single, Double, and Triple Bonds. *J. Phys. Chem. A* **2002**, *106*, 9491–9498.

(157) Shearer, G. C.; Chavan, S.; Ethiraj, J.; Vitillo, J. G.; Svelle, S.; Olsbye, U.; Lamberti, C.; Bordiga, S.; Lillerud, K. P. Tuned to Perfection: Ironing Out the Defects in Metal–Organic Framework UiO-66. *Chem. Mater.* **2014**, *26*, 4068–4071.

(158) Taddei, M. When Defects Turn into Virtues: The Curious Case of Zirconium-Based Metal-Organic Frameworks. *Coord. Chem. Rev.* **2017**, *343*, 1–24.

(159) Dissegna, S.; Epp, K.; Heinz, W. R.; Kieslich, G.; Fischer, R. A. Defective Metal-Organic Frameworks. *Adv. Mater.* **2018**, *30*, 1704501.

(160) Fang, Z.; Bueken, B.; De Vos, D. E.; Fischer, R. A. Defect-Engineered Metal-Organic Frameworks. *Angew. Chemie Int. Ed.* **2015**, *54*, 7234–7254.

Appendix I

This appendix containg two papers:

Atzori C., Lomachenko K.A., Øien-Ødegaard S., Stock N., Lamberti C., Barolo C., Bonino F. "Disclosing the properties of a new Ce(III)-based MOF: $Ce_2(NDC)_3(DMF)_2$", *Submitted to Crystal Growth & Design in September 2018.*

Lomachenko K.A., Jacobsen J., Bugaev A.L., **Atzori C.**, Bonino F., Bordiga S., Stock N., Lamberti C. "Exact stoichiometry of Ce_xZr_{6-x} cornerstones in mixed-metal UiO-66 MOFs revealed by EXAFS spectroscopy", *Accepted for publishing in JACS in November 2018.*

These papers concern activities discussed in the present thesis.

Appendix II

This appendix contains five papers:

Smolders S., Lomachenko K.A., Bueken B., Struyf A., Bugaev A.L., **Atzori C.**, Stock N., Lamberti C., Roeffaers M.B.J., De Vos D.E. "Unravelling the Redox-catalytic Behavior of Ce^{4+} Metal-Organic Frameworks by X-ray Absorption Spectroscopy", *ChemPhysChem,* **2018**, 19, 373-378.

Atzori, C., Shearer, G.C., Maschio, L., Civalleri, B., Bonino, F., Lamberti, C., Svelle, S., Lillerud, K.P., Bordiga, S. "Effect of Benzoic Acid as a Modulator in the Structure of UiO-66: An Experimental and Computational Study", *J. Phys. Chem. C,* **2017**, 121 (17), 9312-9324

Butova V.V., Budnyk, A.P., Guda, A.A., Lomachenko, K.A., Bugaev, A.L., Soldatov, A.V., Chavan, S.M., Oien-Odegaard, S., Olsbye, O., Lillerud K.P., **Atzori, C**., Bordiga S., Lamberti C. "Modulator Effect in UiO-66-NDC (1,4-Naphthalenedicarboxylic Acid) Synthesis and Comparison with UiO-67-NDC Isoreticular Metal-Organic Frameworks", *Cryst. Growth Des.*, **2017**, *2017 (10)*, 5422-5431

Masala A., Grifasi F., **Atzori C.**, Vitillo J.G., Mino L., Bonino F., Chierotti M.R., Bordiga S. "CO_2 Adsorption Sites in UTSA-16: Multitechnique Approach", J. Phys. Chem. C, **2016**, 120 (22), 12068-12074

Kavoosi, N., Bon, V., Senkovska, I., Krause, S., **Atzori, C.**, Bonino, F., Pallmann, J., Paasch, S., Brunner E., Kaskel, S. "Tailoring adsorption induced phase transitions in the pillared-layer type metal-organic framework DUT-8(Ni)", *Dalton Trans.,* **2017***,* 46 (17), 4685-4695.

These papers concern topics not discussed in the present thesis but also part of my PhD activities.